Characterisation and Modelling of Spinal Facet Joints

Mohd Juzaila Abd Latif

Submitted in accordance with the requirements for the degree of

Doctor of Philosophy

The University of Leeds

School of Mechanical Engineering

May, 2011

The candidate confirms that the work submitted is his own, except where work which has formed part of jointly-authored publications has been included. The contribution of the candidate and the other authors to this work has been explicitly indicated below. The candidate confirms that appropriate credit has been given within the thesis where reference has been made to the work of others.

1. Chapter 4 of this thesis is based on a jointly-authored abstract submitted to 4th International Conference of Computational Bioengineering (2009), Bertinoro, Italy: "Morphological study of ovine spinal facet joint", which is authored by Abd Latif M.J., Jin Z.M. and Wilcox R.K. The candidate undertook the major tasks of the work presented in the paper. Being the supervisor of the candidate, Dr. Ruth Wilcox and Prof. Zhongmin Jin guided the candidate throughout the process of the work.

2. Chapter 5 of this thesis is based on a jointly-authored manuscript abstract to 17th Congress of the European Society of Biomechanics 2010, Edinburgh, UK and 6th World Congress on Biomechanics 2010, Singapore: "Biomechanical characterisation of ovine spinal facet joint cartilage", which is authored by Abd Latif M.J., Jin Z.M. and Wilcox R.K. The candidate undertook the major tasks of the work presented in the paper. Being the supervisor of the candidate, Dr. Ruth Wilcox and Prof. Zhongmin Jin guided the candidate throughout the process of the work.

The right of Mohd Juzaila Abd Latif to be identified as Author of this work has been asserted by him in accordance with the Copyright, Designs and Patents Act 1988.

Acknowledgements

Abstract

The spinal facet joints are known to be an important component in the kinematics of the spine and play a role in the load transmission through the spinal vertebrae. Due to the high level of mobility and the large forces influencing the facet joint, it can develop significant degenerative changes which lead to the back pain problems in the human spine. However, the technical difficulties, limitations, ethical concerns and cost involved in experimental studies of human facet joints have driven the use of computational modelling studies. The aim of this study was to characterise the anatomical and biomechanical behaviour of the spinal facet joints and evaluate the use of an ovine facet joint model as a representation of the human facet joint.

In the present study, ovine spines were used in order to investigate an animal model to represent the human spine in the facet joint studies. Morphological studies were carried out to determine the facet articular radius and facet orientation angle using an improved method based on micro-computed tomography scan images. Subsequently, the biomechanical properties of the cartilage in the ovine facet joint were characterised using a combination of experimental and computational methods. The similarities of the results obtained between the ovine and human results indicate that the ovine spine would be a good model to represent the human spine in facet joint studies.

A novel specimen-specific modelling approach was implemented to model the cartilage specimen since the model could replicate the actual curvature of the cartilage surface and the trabecular architecture of the subchondral bone. The specimen-specific model demonstrated that the cartilage curvature, the elastic modulus of the subchondral bone and trabecular architecture of the subchondral bone, influenced the characterisation of the biphasic properties of the cartilage. The methodologies developed were then applied in a pilot study in human facet joint specimens and recommendations made for future work in this area.

Contents

Figures

Tables

Nomenclature

E – Elastic Modulus

v – Poisson's Ratio

κ – Permeability

H – Aggregate Modulus

e – Void Ratio

μ – Friction Coefficient

V – Volume

C – Compression Modulus

$E_{composite(axi)}$ – Composite elastic modulus derived from axisymmetric biphasic model

$E_{composite(3D\ solid)}$ – Composite elastic modulus derived from 3D solid specimen-specific model

$E_{composite(3D\ trabecular)}$ – Composite elastic modulus calculated from 3D specimen-specific model

Abbreviations

LBP – Low Back Pain

CT – Computed Tomography

μCT – Micro Computed Tomography

MRI – Magnetic Resonance Imaging

3D – Three Dimensional

FOC – Facet Orientation Circle

FCC – Facet Curvature Circle

ECM – Extracellular Matrix

GAG – Glycosaminoglycan

H&E – Hematoxylin and Eosin

FE – Finite Element

FEA – Finite Element Analysis

ROM – Range of Motion

PBS – Phosphate Buffered Saline

LVDT – Linear Variable Differential Transformer

CAX4RP – Four-node bilinear displacement and pore pressure, reduced integration

CAX8RP – Eight-node bilinear displacement and pore pressure, reduced integration

CAX4 – Four-node bilinear

C3D8RP – Eight-node trilinear displacement and pore pressure, reduced integration

C3D8 – Eight-node linear brick

C3D4 – Four-node linear tetrahedral

SD – Standard Deviation

Chapter 1: Literature Review

1.1 Introduction

Low back pain (LBP) has a lifetime prevalence of about 60% to 80% and is a leading cause of disability (Frymoyer *et al.*, 1983, Linton *et al.*, 1998, Friedrich *et al.*, 2007, Strine and Hootman, 2007, Schmidt *et al.*, 2007a). In the United Kingdom, the total cost of LBP treatments in 1993 exceeded £8 billion and in the United States, the total cost reached to $200 billion in 2005 (Rosen, 1994, Katz, 2006). There is also a high cost in terms of lost working hours associated with such pain.

There are various structures in the low back region that can cause severe LBP. One of the sources of LBP is the facet joints, also known as zygapophysial joints, which have been implicated in chronic LBP (Helbig and Lee, 1988, Dreyer and Dreyfuss, 1996, Manchikanti et al., 1999). The fact that pain can originate from the facet joints is widely accepted in the radiologic and orthopaedic literature (Mooney and Robertson, 1976, Carrera et al., 1980, Lewinnek and Warfield, 1986, Cavanaugh et al., 1996, Manchikanti et al., 1999, Kalichman and Hunter, 2007).

This chapter reviews the background of LBP and the characterisation of the human spinal facet joints. The experimental methods and the development of finite element models of the facet joints are also outlined while highlighting the need for further research. Throughout this thesis, the anatomic directions of human body are expressed according to the clinical terms shown in Figure 1.1.
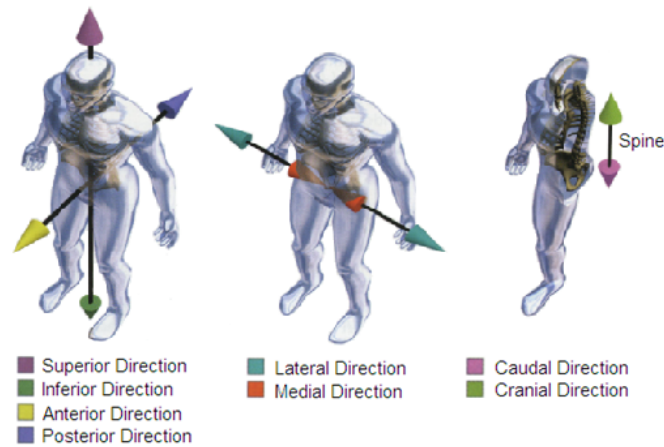
Figure 1.1. Anatomic reference directions. Adapted from Kurtz and Edidin (2006).

1.2 Structure and Anatomy of the Spine

1.2.1 Introduction

The human spine is a complex structure that provides both mobility and stability, and also protects the spinal cord. The normal spine has three natural curves, the cervical (neck) curve, the thoracic (middle back) curve, and the lumbar (lower back) curve as shown in Figure 1.2. There is also a fourth curve in the fused sacral region of the spine. The cervical and lumbar sections curve forward (lordosis), while the thoracic section curves backward (kyphosis). This curvature allows even distribution of weight and the withstanding of the applied loads.

The spine is divided into cervical, thoracic, lumbar and sacral regions. The cervical spine is the top seven vertebrae (C1-C7) in the neck area which starts just below the skull. These are smaller bones that allow the head to turn freely, while the rest of the back remains stationary. The thoracic spine is made up of the twelve vertebrae (T1-T12) in the middle back, and each thoracic vertebra is attached to a rib. The lower back, which is called the lumbar spine, is made up of the next five vertebrae (L1-L5). Finally, below the lumbar region are five fused vertebrae (S1-S5) of the sacrum and the bone of the coccyx referred as the tail bone.
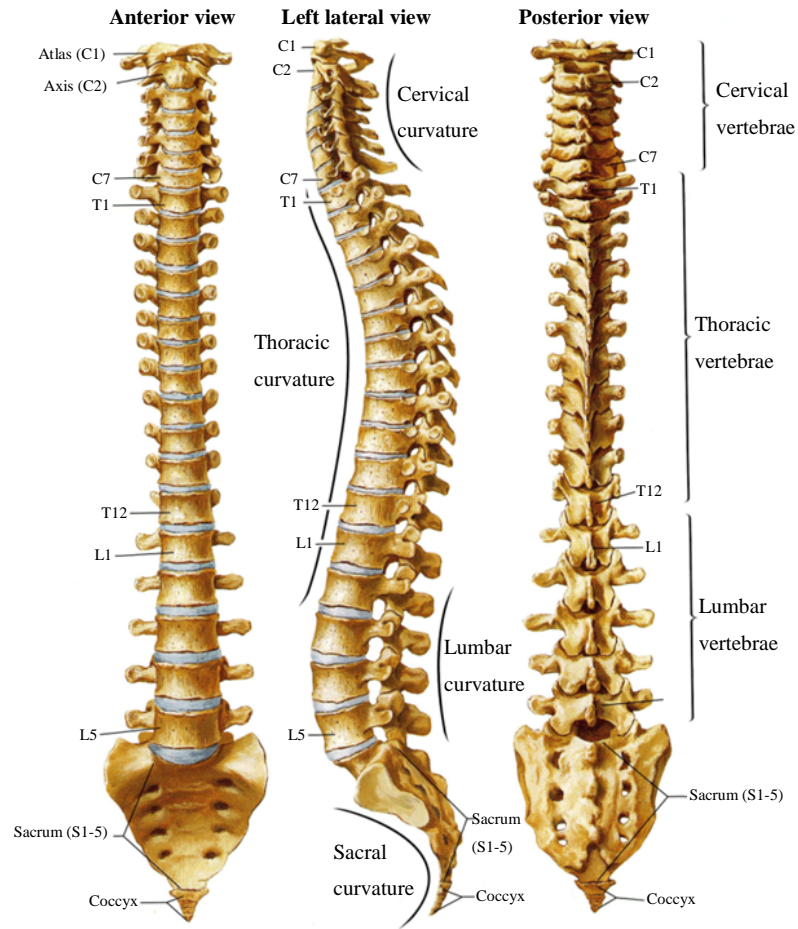
Figure 1.2. The human spine. Adapted from Netter (2006).

The real flexibility of the spine results from complex kinematic motions of the structure. However in human spine studies, it is well accepted that the motion can be simplified into extension, flexion, lateral bending and axial rotation as shown in Figure 1.3. As well as the rotation motions, the spine will also be subjected to axial displacement with the application of traction and compression motions.
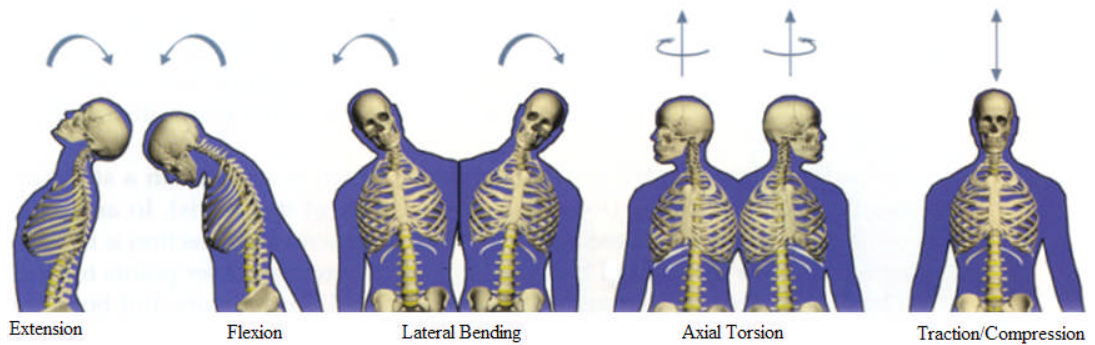
Figure 1.3. The kinematic motions of the spine. Adapted from Kurtz and Edidin (2006).

Even though the lower portion of the spine holds most of the body's weight, each segment relies upon the strength of the others to function properly. This interdependence among all sections of the spine, and the requirement to serve the demands of both mobility and stability, make the spine vulnerable to injury and deterioration due to aging.

1.2.2 Vertebra

The vertebrae are irregular shaped bones consisting of various components. The anterior part of the vertebra is a large block of bone called the vertebral body, and the posterior part of the vertebra is connected to it via the pedicles. Projecting posteriorly from the pedicles, the bone structures extend and develop into specialised masses of bone called the superior articular process, the inferior articular process, the transverse process, and the spinous process, as shown in Figure 1.4.
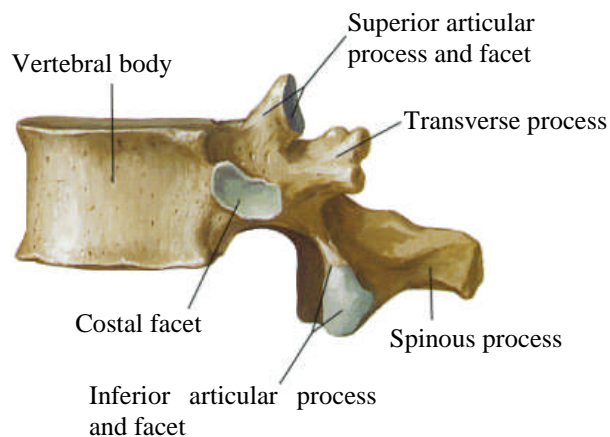
Figure 1.4. Lateral view of thoracic vertebra T12. Adapted from Netter (2006).

The vertebral body comprises of a strong outer layer of cortical bone and a hollow cavity which is reinforced by vertical and horizontal struts called trabecular (cancellous) bone. Cortical bone is a very dense material that provides high stiffness and strength in a relatively thin compact structure, while the trabecular bone is a porous and sponge-like network of bone material. However in some cases, the cortical bone of the vertebrae is more like dense trabecular bone (Mosekilde, 1993,

Silva *et al.*, 1994). Table 1.1 shows previous experimental studies that have been conducted to determine the mechanical properties of the trabecular bone in the vertebral body.

Table 1.1. The compressive modulus and ultimate stress of trabecular bone in vertebral body.

Reference	Age	Vertebra	Compressive Modulus (MPa)	Ultimate Stress (MPa)
Mosekilde, 1987	15-87	L1	67 ± 45	2.4 ± 1.6
Hansson, 1987	71-84	L1-L4	22.8 ± 15.5	1.55 ± 1.11
Kopperdahl, 1998	32-65	T1-L4	291 ± 113	2.23 ± 0.95

1.2.3 Vertebral Joints and Ligaments

There are a number of connections between the vertebrae including the intervertebral disc, ligamentous structures and facet joints. In addition, the vertebrae at the thoracic region articulate with the ribs that are attached at the costal facets. The intervertebral discs lie between the adjacent superior and inferior surfaces of the vertebral bodies from C2 to S1 with the shape of the discs varying according to the dimensions of the vertebral bodies. The inferior and superior articular processes of each vertebra are joined by a facet joint and covered by a facet capsulary ligament known as the facet capsule.

The spinal ligaments are important structures for maintaining the stability of the spine because they provide the mechanical constraint to prevent overextension. There are two primary ligament systems in the spine, the intrasegmental and intersegmental systems. The intrasegmental system connects adjacent vertebrae individually, and includes the ligamentum flavum, interspinous ligament, intertransverse ligament, and facet capsulary ligament as shown in Figure 1.5. While the intersegmental system, consisting of the anterior longitudinal ligament, posterior longitudinal ligament, and supraspinous ligament, holds the vertebrae along the thoracolumbar spine.
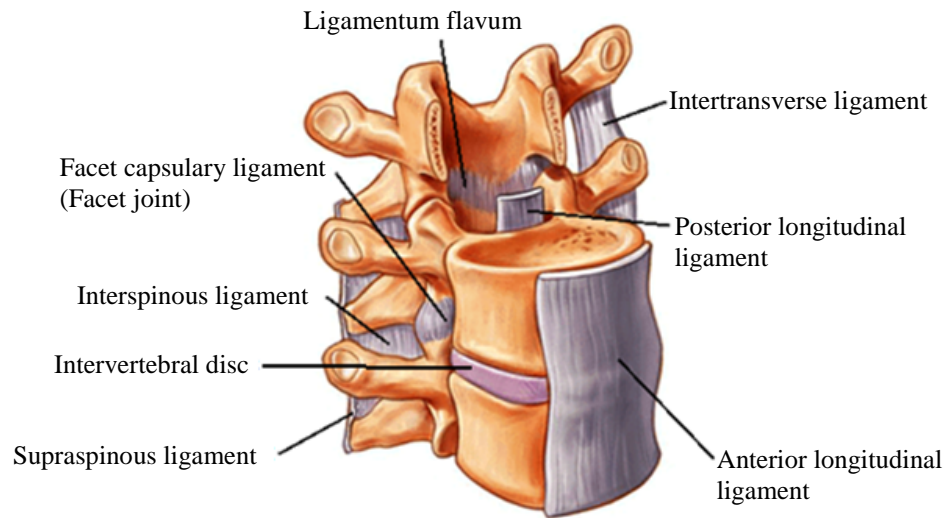
Figure 1.5. Vertebral joints at lumbar region. Adapted from www.spineuniverse.com.

1.2.3.1 Intervertebral Disc

The intervertebral disc consists of an annulus fibrosus, surrounding the nucleus pulposus, and covered by the endplates at the top and bottom surfaces as shown in Figure 1.6. The discs allow complex movement between vertebrae without mechanical disadvantages of the opposing vertebra surfaces. It resists spinal compression while permitting limited bending, twisting, and sliding between vertebral bodies. These motions are resisted by the elasticity and tensile forces developed in the collagen fibres of the annulus fibrosus (Adams *et al.*, 2002). Another function of the disc is to distribute the loads applied to the spine evenly on the vertebral bodies. Each disc forms a cartilaginous joint to stabilise the spine and maintain its alignment by anchoring adjacent vertebral bodies to each other.
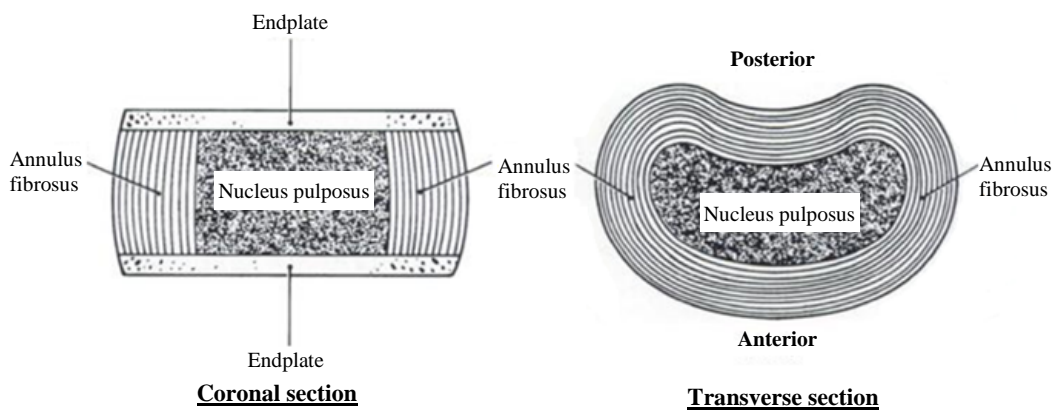
Figure 1.6. The basic structure of intervertebral disc. Adapted from Adams *et al.* (2002).

i. Nucleus Pulposus

The nucleus pulposus is a gelatinous semi-solid structure consisting of a random network of collagens and proteoglycans, which bind water. Water constitutes about 70% to 80% of total nucleus pulposus weight and type II collagen dominates about 80% of the total collagen content (Guerin and Elliot, 2006). It has been reported that the swelling pressure of healthy nucleus pulposus tissue is 0.1 to 0.2 MPa in a lying position, 0.3 to 1 MPa in sitting and standing positions, and may reach as high as 3 MPa when in a lifting position (Wilke *et al.*, 1999).

ii. Annulus Fibrosus

The annulus fibrosus is a ring of highly organised angle-ply laminate structures that forms the outer boundary of the intervertebral disc and surrounds the nucleus pulposus. It consists of 15 to 25 distinct layers where the fibres are organised in an alternating layout at an angle of between 20 and 45 degrees with respect to the transverse axis (Cassidy *et al.*, 1989, Marchand and Ahmed, 1990). The annulus is composed of collagen type I and type II fibres embedded in a proteoglycan matrix (Adams *et al.*, 2002, Guerin and Elliot, 2006).

Under compression loading of the intervertebral disc, the inner annulus is exposed to axial compression stresses and the bulging of the nucleus pulposus results in radial compressive and circumferential tensile stresses in the outer annulus (Adams *et al.*, 2002). However in bending or torsion loading conditions, the fibres may be loaded directly in tension at some point around the circumference of the annulus fibrosus.

iii. Endplates

The vertebral endplate consists of hyaline cartilage that forms a structural boundary between the intervertebral disc and the cancellous core of the vertebral body. It comprises of a gel of hydrated proteoglycan molecules reinforced by a network of collagen fibrils (Moore, 2006) and the thickness ranges from 0.26 to 1.08 mm, with a mean value of 0.58 ± 0.35 mm; the thickness has been observed to be greater in the lumbar vertebrae in comparison to the thoracic vertebrae (Edwards *et al.*, 2001).

The principal functions of the endplate are to prevent extrusion of the disc into the porous vertebral body, and to evenly distribute load to the vertebral body. The endplate is also important for load transfer and the overall structural integrity of the vertebra. This has been experimentally studied where a significant reduction in the local structural properties of the vertebral body was found following partial endplate removal (Oxland *et al.*, 2003).

1.2.3.2 Ligaments

The ligaments are comprised primarily of type I collagen fibres embedded in a hydrated extracellular matrix (Guerin and Elliot, 2006). Generally the ligaments will be stretched and withstand the tension during the movements of the spine. The stiffness of the ligaments have been measured experimentally and it has been found that the facet capsulary ligament has the highest stiffness, as shown in Table 1.2 (Pintar *et al.*, 1992). However, the ligament stiffness may vary strongly from specimen to specimen, depending on age, gender, body height, body weight, physical fitness, genetic influences, and the preparation of the investigated specimen.

Table 1.2. The stiffness of human lumbar ligaments* (Pintar *et al.*, 1992).

Ligament	T12-L1	L1-L2	L2-l3	L3-L4	L4-L5	L5-S1	Mean±SD (N/mm)
ALL	32.9±20.9	32.4±13.0	20.8±14.0	39.5±20.3	40.5±14.3	13.2±10.2	33.0±15.7
PLL	10.0±5.5	17.1±9.6	36.6±15.2	10.6±8.5	25.8±15.8	21.8±16.0	20.4±11.9
CL	31.7±7.9	42.5±0.8	33.9±19.2	32.3±3.3	30.6±1.5	29.9±22.0	33.9±10.7
LF	24.2±3.6	23.0±7.8	25.1±10.9	34.5±6.2	27.2±12.2	20.2±8.4	27.2±9.2
ISL	12.1±2.6	10.0±5.0	9.6±4.8	18.1±15.9	8.7±6.5	16.3±15.0	11.5±6.6
SSL	15.1±6.9	23.0±17.3	24.8±14.5	34.8±11.7	18.0±6.9	17.8±3.8	23.7±10.9

*ALL: Anterior longitudinal ligament; PLL: Posterior longitudinal ligament; CL: Facet capsulary ligament; LF: Ligamentum flavum; ISL: Interspinous ligament; SSL: Supraspinous ligament.

1.3 Low Back Pain

1.3.1 Introduction

LBP is defined 'as pain occurring between the costal margins and the gluteal folds' (Friedrich *et al.*, 2007). Linton *et al.* (1998) estimated the prevalence of spinal pain in the general population as 66%, with 56% of patients reporting pain in the lumbar region, 44% in the cervical region, and 15% in the thoracic region. Another study on spinal pain patients reported that the pain occurrence of 79% in lumbar region, 47% in cervical region, and 22% in thoracic region, where multilevel regions of pain were found for some of the patients (Manchikanti and Pampati, 2002). Although the prevalence percentage varied between these studies, similar trends were found along the spine regions, with the lumbar region having the highest prevalence percentage of LBP.

Lumbar facet joints were first recognised as a potential source of back pain in 1911 by Goldthwait and the term "facet syndrome" was coined by Ghormley in 1933 (Goldthwait, 1911, Ghormley, 1933). Research by Manchikanti *et al.* (1999) demonstrated that the facet joint is a source of pain in 45% of the patients suffering with chronic low back pain. In another study, 500 consecutive patients with chronic, non-specific spine pain were evaluated (Manchikanti *et al.*, 2004). Out of the patients, cervical facet joint pain was seen in 140 patients (28%), thoracic facet joint pain in 30 patients (6%), and lumbar facet joint pain in 124 patients (25%). This indicates that more than half of the chronic low back pain patients were caused by the facet joints and the spread between cervical (28%) and lumbar (25%) is much more even when all cases of back pain are taken into account.

1.3.2 Causes

LBP may originate from many spinal structures, including the ligaments, facet joints, vertebral periosteum, paravertebral musculature and fascia, blood vessels, annulus fibrosus, and the spinal nerve roots. In many instances, the exact cause of LBP cannot be determined despite thorough evaluation of the patient by capable clinician due to this wide range of causes. Furthermore, clinical studies have found that the correlation between clinical symptoms and imaging results is weak (Sarzi-

Puttini *et al.* 2004, Deyo and Weinstein, 2001). Thus, nonspecific terms, such as strain, sprain, or degenerative processes, are commonly used.

However, the most common causes of LBP are musculoligamentous injuries and age-related degenerative processes in the intervertebral discs and facet joints (Deyo and Weinstein, 2001). It was also reported that spinal stenosis and disc herniation were among the common source of LBP (Sarzi-Puttini *et al.* 2004, Arnoldi *et al.*, 1976). Spinal stenosis is narrowing of the central spinal canal that produces pressure on the nerve roots typically from degenerative changes in spinal structures.

1.3.3 Diagnosis

Various diagnostic tests are employed in the evaluation of low back pain. Clinically, the first stage of the LBP diagnosis is observation of the medical history and physical examination of the patient. If potential serious conditions are suspected, imaging diagnostics are performed using imaging techniques such as plain radiography, computed tomography (CT) scanning and magnetic resonance imaging (MRI). However, the diagnostic tests may vary for children, pregnant women and older patients (Chou *et al.*, 2007).

Plain radiography is normally performed on patients with clinical findings suggesting systemic disease or trauma, while for CT or MRI are used for patients whom there is a strong clinical suggestion of underlying infection, cancer, or persistent neurologic deficit (Deyo and Weinstein, 2001, Chou *et al.*, 2007). Imaging diagnostic tests are also used for diagnosing the degenerative facet disease studies as shown in Figure 1.7 (Carrera *et al.*, 1980, Fujiwara *et al.*, 1999, Weishaupt *et al.*, 1999). However, imaging studies only provide anatomic information and are unable to determine the particular painful structure (Dreyer 1996).
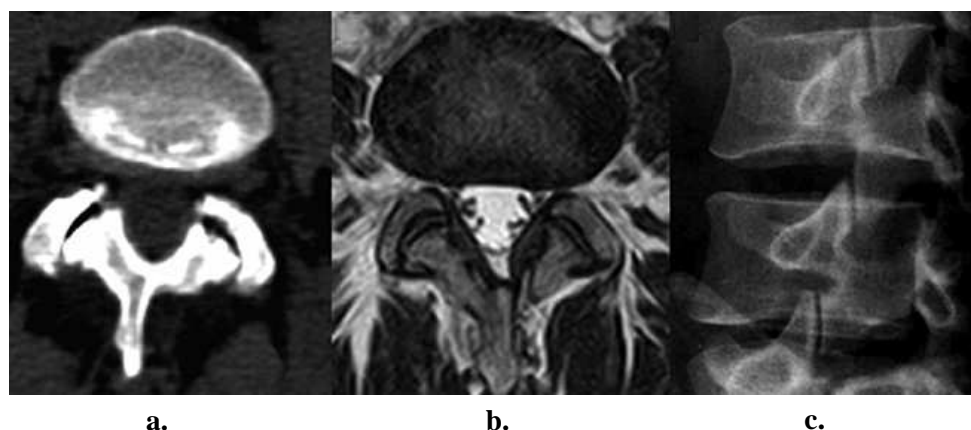
Figure 1.7. Examples of images of the facet joints a. CT scan b. MRI c. Oblique radiograph. Adapted from Kalichman and Hunter (2007).

1.3.4 Treatment

The treatments for low back pain are selected after the diagnosis of the problem, whether it is chronic or acute. In general, supervised exercise therapy and spinal manipulation are used in the first stage of treatments (Chou *et al.*, 2007). However, the effects of these physical treatments have been contradictory, with one study reporting them to help to restore function, improve mobility, relieve pain and prevent physical disabilities of patients suffering from back pain (Maul *et al.*, 2005), whilst others found the effects were limited (Andersson *et al.*, 1999, Geisser *et al.*, 2005).

The pain is also treated by medications such as non-steroidal anti-inflammatory drugs, muscle-relaxants, antidepressants and analgesics in the later stage of the treatment (Deyo and Weinstein, 2001, Mens, 2005, Chou *et al.*, 2007). Surgical intervention is only performed when one of the following is observed: herniated intervertebral discs with persistent sciatica, spinal stenosis with progressive or severe neurologic deficit, and spondylolisthesis with progressive or severe neurologic deficit (Deyo and Weinstein, 2001, Sarzi-Puttini *et al.*, 2004).

For the back pain which is suspected from the facet joints, history and physical examination is observed after the patients have received treatment with intraarticular facet injections of local anaesthetic agents, such as lidocaine and bupivacaine (Manchikanti *et al.*, 1999, Young *et al.*, 2003, Manchikanti *et al.*, 2004, Laslett *et al.*, 2006). Studies have shown that injection of steroids into the facet joints can help relieve the low back pain for intermediate and long term periods (Lilius *et al.*, 1989,

Marks *et al.*, 1992). Alternatively, radiofrequency denervation treatment has also been used to relieve the pain (van Kleef *et al.*, 1999, Leclaire *et al.*, 2001). Surgery such as arthrodesis (fusion) is only occasionally performed to treat facet arthropathy because of discouraging results and the potential to cause traumatic dislocation (Cohen and Raja, 2007). However, facet implants such as interspinous process spacers and anatomic facet replacement systems may improve the results of the surgical intervention but as yet, long term studies have not been carried out, so the outcomes are not yet fully known.

1.4 Facet Joint

1.4.1 Introduction

The facet joints are categorised as synovial (diarthrodial) joints and are located at the posterior side of the spine column, connecting the superior and inferior processes of neighbouring vertebrae. The articular surfaces are coated with cartilage and covered with capsules as shown in Figure 1.8. The joint is nourished and lubricated by synovial fluid which is produced from the connective tissue of the capsule in order to allow the joints to articulate smoothly.
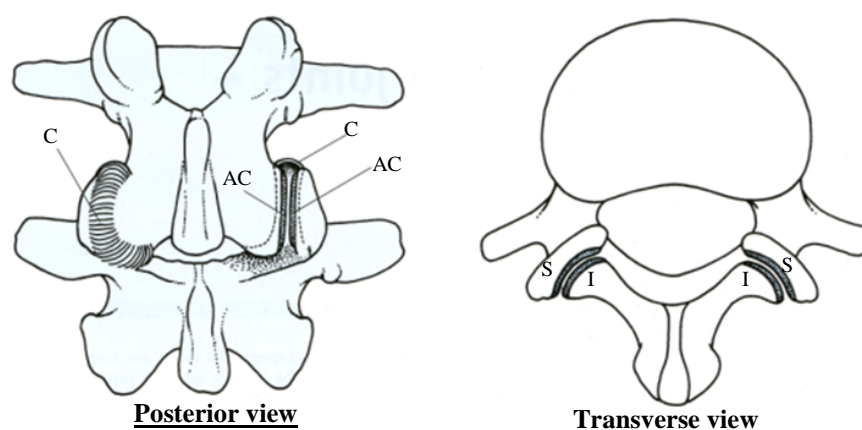
Figure 1.8. The lumbar L3-L4 facet joint. Adapted from Bogduk (2005).

*C: Joint capsule; AC: Articular cartilage; S: Superior articular process; I: Inferior articular process.

The spinal facet joints have been recognised as an important component in the kinematics of the spine (Miyazaki *et al.*, 2010). The main function of the facet joint

is to limit excessive intervertebral shear and torsion motions of the intervertebral segment (Stokes, 1988, Mow and Huiskes, 2005). They also play an important role in load transmission through the vertebrae, where the normal facets carry 3% to 25% of the load applied at the vertebra and potentially as high as 47% if the facet joint is arthritic (Adams and Hutton, 1980, Yang and King, 1984). Because of their high level of mobility and the large forces influencing the facet joints, especially in the lumbar area, the joints can develop significant degenerative changes which lead to pain and disability.

1.4.2 Anatomy

Throughout the spinal column, the size and shape of the articular facets differ in order to accommodate the function of a particular spinal region. The shape is associated with the amount of stress on the vertebral column and the kinematics related to motion segments in the spine (Masharawi *et al.*, 2005). Generally the articular facets morphology vary from a flat shape to a curved shape with the appearance of a "C" or "J" curve (Bogduk, 2005).

1.4.2.1 Linear Dimensions

The first major effort to create a database of the facet sizes was conducted by Panjabi *et al.* (1993) where the linear dimensions of articular facets for human spine were measured from cervical C2 vertebra to lumbar L5 vertebra as illustrated in Figure 1.9. The width, height, and area of the articular facets were found to range from 9.5 mm to 16.8 mm, 10.2 mm to 18.4 mm, and 72.3 mm^2 to 211.9 mm^2 respectively. In addition, similar measurements were also carried out from another study to evaluate the facet dimensions from thoracic T1 vertebra to lumbar L5 vertebra (Masharawi *et al.*, 2005). The facet dimensions from both studies are comparable.
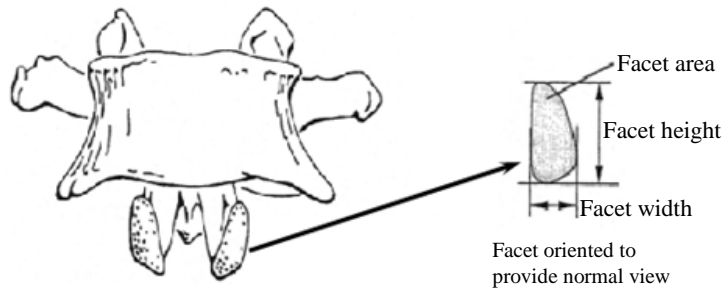
Figure 1.9. Linear and areal dimensions of facets measured*. Adapted from Panjabi *et al.* (1993).

1.4.2.2 Facet Orientation

In previous studies, the facet orientation was characterised using either the facet joint diameter or facet angle using various measurement methods such as CT scan images (Hagg and Wallner, 1990, van Schaik *et al.*, 1997), a modified protractor (Tulsi and Hermanis, 1993) and a three-dimensional (3D) coordinate measurement system (Panjabi *et al.*, 1993, Masharawi *et al.*, 2004). Van Schaik *et al.* (1997) determined the facet joint orientation based on a diameter measured from the transverse plane of CT scan images. A circle, known as facet orientation circle (FOC), was formed through three edge points of the left and right facet joints as shown in Figure 1.10.
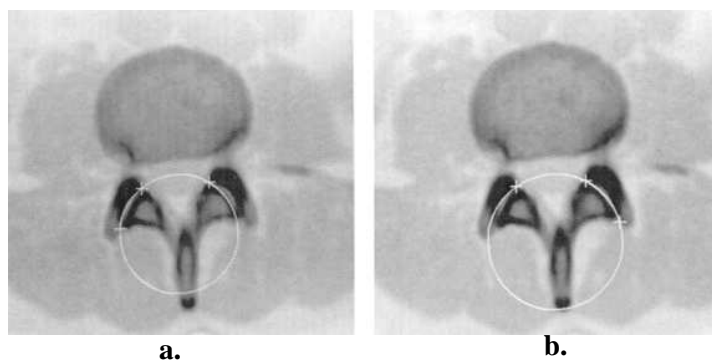
Figure 1.10. Reference points used to determine the FOC a. Right facet b. Left facet. Adapted from van Schaik *et al.* (1997).

However, most of the facet orientation studies used angles as the reference parameter. The facet orientation angle has been assessed from two-dimensional transverse plane either on the dissected vertebrae or the CT scan images. In both cases, the angle was measured from the facet line constructed on two extremities

points of the superior articular facet, to the reference line created through the spinous process and midpoint of the vertebral body as shown in Figure 1.11 (Ahmed *et al.*, 1990, Hagg and Wallner, 1990, Tulsi and Hermanis, 1993). In addition, the facet orientation angles were also measured in three dimensions based on the longitudinal facet angle (Panjabi *et al.*, 1993, Masharawi *et al.*, 2004).
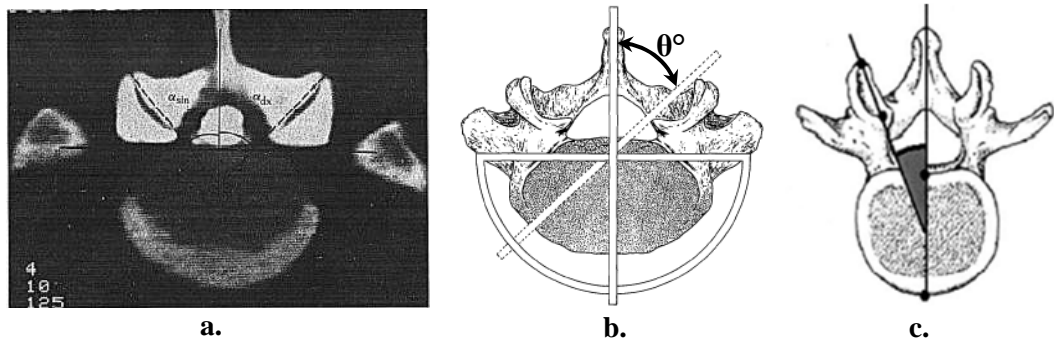
Figure 1.11. Measurements of facet orientation angle a. Hagg and Wallner (1990), b. Tulsi and Hermanis (1993), c. Masharawi *et al.* (2004).

Figure 1.12 shows comparisons of the facet angle measured from the previous studies. Based on the results, no definite trend with respect to the vertebral level can be seen due to the inconsistency of the results. Although substantial measurement variations were obtained by Masharawi *et al.* (2004), results from the other studies seem to be around this range. The large number of samples (*n=240*) used by Masharawi *et al.* (2004) perhaps better represent the variation across the population and so could be the most useful for making comparison to future studies.
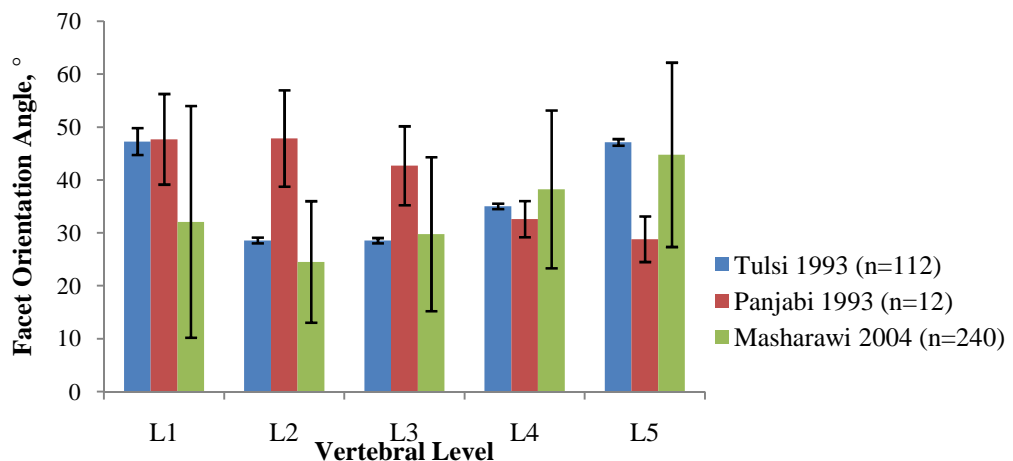
Figure 1.12. Comparison of facet orientation angle measured from previous studies.

1.4.2.3 Facet Articular Radius

The facet joint curvature was probably first quantified by Hagg and Wallner (1990) by using CT scan images. The scans were performed on patients with no degenerative changes of the facet joints as observed on the CT scan. The curvature was measured at the superior articular facet by approximating a set of circles with different radius of 0.5 cm, 1.0 cm, 2.0 cm, and 5.0 cm. The measurement method was then improved in another study where a circle known as the facet curvature circle (FCC) was constructed from the CT scan images, based on three reference points along the edge of the superior articular facet as shown in Figure 1.13 (van Schaik and van Pinxteren, 1999).
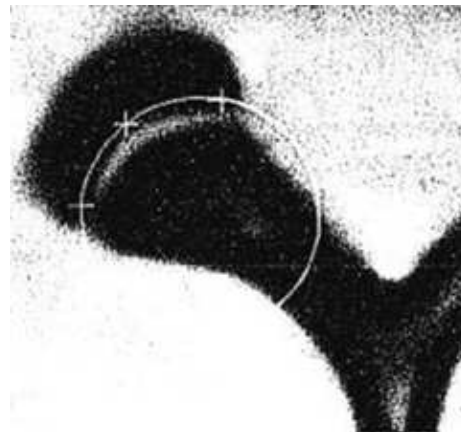
Figure 1.13. CT scan image with FCC drawn through reference points. Adapted from van Schaik and van Pinxteren (1999).

The facet curvature has also been quantified directly using cadaveric specimens where a fine ductile wire was used to mould the midfacet surface (McLain *et al.*, 2002). A contact radiograph was performed on the wire and transferred to an image analysis system where a best-fit circular outline was applied to each facet curvature.

A comparison of the measured radius between the different studies is outlined in Table 1.3. A similar range of values of facet radius was found from both measurement methods.

Table 1.3. Comparisons of the human superior facet radius measured by van Schaik and Pinxteren (1999), and McLain *et al.* (2004).

Reference	Method	Vertebra	Facet Radius (mm)
McLain, 2002	Direct measurement using ductile wire	L4 (*n=7*)	20.0
van Schaik, 1999	CT scan	L4 (*n=67*)	13.6±6.0 (right) 13.8±7.6 (left)
		L5 (*n=71*)	16.8±9.0 (right) 18.4±8.4 (left)

1.4.3 Characterisation of Load Bearing in the Facet Joint

Since the spinal facet joints play a role in load transmission through the spine, the characterisation of the load bearing of the facet joints is important in order to understand the normal function and provide mechanical understanding of the joint. Methods of measuring the load in facet joints can be divided into direct and indirect methods. Direct methods, such as pressure-sensitive film and pressure transducer techniques, employ sensors adjacent to the surfaces which are under load. Indirect methods such as strain gauge techniques, deduce the joint loads by measuring the related parameters of the joints subjected to loading. Although a few other measuring techniques have been utilised (Adams and Hutton, 1980, Yang and King, 1984, El-Bohy *et al.*, 1989, Hedman, 1992), the strain gauge, pressure-sensitive film, and pressure transducer measuring techniques are the most widely used to measure the loads transmitted through the facet joints.

1.4.3.1 Strain Gauge

A strain gauge is a device that measures the deformations of the material to which it is attached. Early work in biomechanics that utilised the strain gauge was to quantify *in vivo* bone strains (Lanyon, 1972).

Strain gauges were first used in human spine studies to examine mechanical response of the lumbar intervertebral joint under physiological loading (Lin *et al.*, 1978). The gauges were mounted on the surface of the vertebral body and also near to the articular process of the vertebra. During extension loading, the strain gauges

at the articular process were activated indicating that there was a second load path through the superior and inferior articular processes. This was supported by Schendel *et al.* (1993) using the same technique. Here, the strain gauges were attached at the inferior articular process rather than the superior articular process, as shown in Figure 1.14, because the human superior articular process contains more bone mass which prevents the effectiveness of the strain gauge measurement. The facets were found to carry large loads during extension, torsion, and lateral bending, but none in flexion. Strain gauges have also been used in the canine lumbar spine to determine the facet loads where combinations of three or more gauges were attached at the bony surface of articular process (Kahmann *et al.*, 1990, Buttermann *et al.*, 1992, Luo *et al.*, 1996).
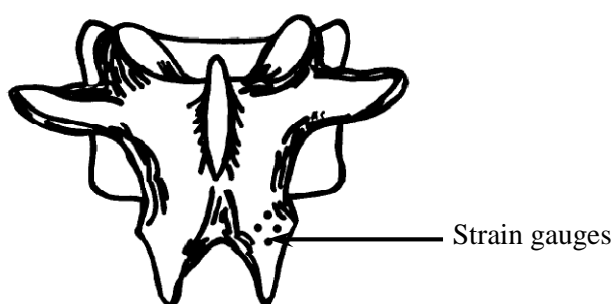
Figure 1.14. Posterior view of Ll vertebral body illustrating strain gauge placement on the inferior articular process. Adapted from Schendel *et al.* (1993).

However, to ensure that the strain gauges remain functional and attached to the bone during the testing and calibration in high humidity environments is a difficult task (Schendel *et al.*, 1993). Furthermore, strain gauge methods deduced facet joint loads by measuring the related parameters of the joints subjected to loading. It has also been reported that the strain gauges are highly sensitive to the placement and number of strain gauges used (Buttermann *et al.*, 1992, Luo *et al.*, 1996).

1.4.3.2 Pressure-Sensitive Film

The common type of sensor used to measure the contact area and planar pressure in synovial joints is Fuji Prescale pressure-sensitive film. Fuji Prescale measurement consists of pressure-sensitive film, a densitometer, and pressure

reader. The films are supplied according to the pressure range starting from 0.05 MPa to 300 MPa. When pressure is applied to the film, a red colour impression is formed in varying density according to the amount of pressure and pressure distribution. The densitometer is used to read the colour density on the film and convert it into digital data. Finally the pressure value is determined using an image processing method.

Fuji Prescale film has been widely used in contact biomechanics studies of synovial joints. The applications of the film range from the qualitative assessment of contact stress pattern (Lorenz *et al.*, 1983, Dunlop *et al.*, 1984, Huberti and Hayes, 1988, Warner *et al.*, 1998) to quantitative analysis of the contact pressure in synovial joints using digital image techniques (Brown *et al.*, 1988, Wagner *et al.*, 1992, Clark *et al.*, 2002).

Lorenz *et al.* (1983) and Dunlop *et al.* (1984) utilised the Fuji Prescale film to quantify directly the peak pressures, contact areas, and facet loads of the human facet joints subjected to compression load. The film was sealed in moisture proof packets (Lorenz *et al.*, 1983) or Sellotape (Dunlop *et al.*, 1984), in order to prevent the film damage from the moisture, and then inserted between the articulating surfaces of the two facet joints prior applying the loads. The results of the peak pressure from both measurements for neutral and extension vertebral segments positions are shown in Figure 1.15 and Figure 1.16. Although it is not appropriate to compare the results because of the difference in the test set-up, the outcomes demonstrate the sensitivity of the load bearing characterisation for the facet joint because the specimen preparation, loading set-up and type of Fuji film were different between the two studies.
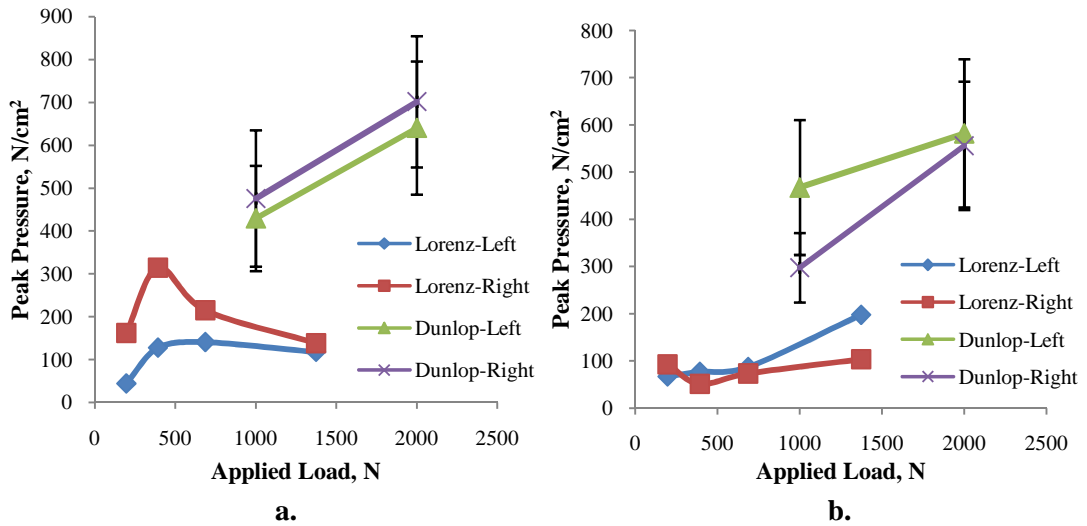
Figure 1.15. Peak pressures in neutral position a. L2-L3 segments b. L4-L5 segments (Lorenz *et al.*, 1983, Dunlop *et al.*, 1984).
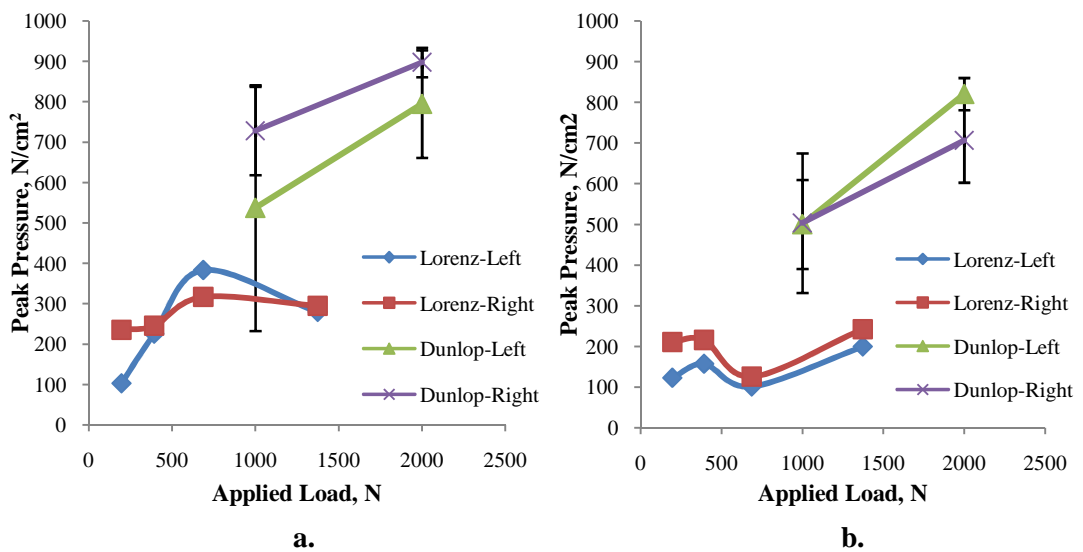
Figure 1.16. Peak pressures in extension position (6º to 8º) a. L2-L3 segments b. L4-L5 segments (Lorenz *et al.*, 1983, Dunlop *et al.*, 1984).

The measurement error of Fuji film for biomechanical use was reported to be between 10% to 28% (Wu *et al.*, 1998). However, the accuracy of the measurement can be increased by incorporating more than one range of film into experimental studies (Atkinson *et al.*, 1998). The main concern of using the Fuji Prescale film is that the measurement of the pressure and contact area can only be carried out at one cycle of the experiment and only measures the maximum pressure.

1.4.3.3 Pressure Transducer

The pressure transducers used in the facet joint studies have normally been fabricated according to the particular interest of the studies. The technique is a combination of other measurement techniques such as Fuji Prescale film and force sensing resistor (Hedman, 1992) and a diaphragm instrumented with a foil-type strain gauge (El-Bohy *et al.*, 1989). However, Tekscan (South Boston, USA) introduced a commercial pressure transducer measurement system which could measure the contact area, force, and pressure in the synovial joints.

The Tekscan computerised measurement system consists of a sensor, computer interface, and software. The sensor is made from a thin and flexible resistive sensor that uses patterns of electrical conductors which produce a grid of sensing elements. It connects to a standard personal computer with specialised interface hardware. This system includes software for calibration, recording and analysing data, and converting the measured resistances into estimates of resultant force, mean and maximum pressure, contact area, and centre of pressure.

Experimental studies have been carried out to examine the measurement accuracy of the Tekscan system by comparing to the Fuji Prescale films (Harris *et al.*, 1999, Wilson *et al.*, 2003). The contact areas measured using the Tekscan system were found to be more accurate, while comparable results in terms of the contact force and contact pressure were observed in the experiments. In addition, consistent and repeatable measurements were achieved using the Tekscan system.

The Tekscan system has been applied to measure the facet load directly where the sensor was inserted in the facet joint as shown in Figure 1.17 (Wilson *et al.*, 2006). Consistent and repeatable results were achieved for different loads and loading types. However, the accuracy depends on the calibration method and the applied load level with the range of sensor's measurement (Wilson *et al.*, 2006, Ramruttun *et al.*, 2008).
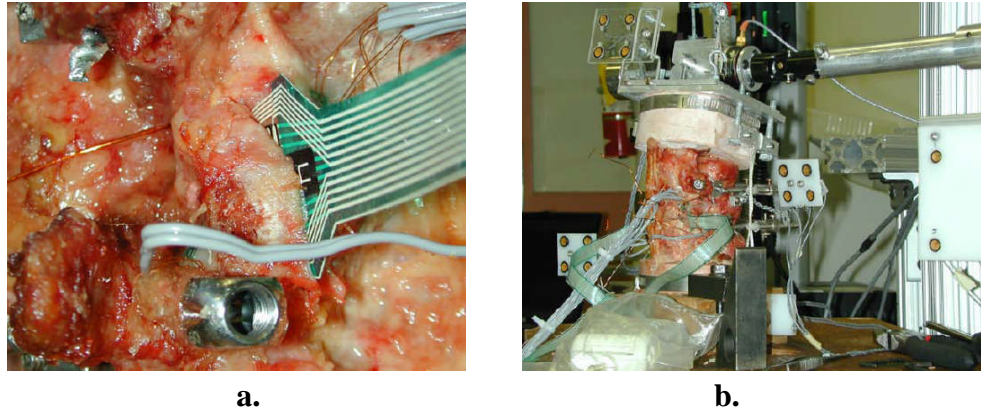
Figure 1.17. Measurement of facet joint load using Tekscan system a. Tekscan sensor inserted into facet joint b. Testing set-up. Taken from Wilson *et al.* (2006).

1.4.4 Discussion

An extensive database of the facet height, width, area, and orientation angle of the facet joints have been established (Panjabi *et al.*, 1993, Masharawi *et al.*, 2004, Masharawi *et al.*, 2005). However, the measurements were made based on the linear dimensions which were unable to include the curvature of the articular facets. The curvatures of the articular facets have been reported to be an important aspect in computational method particularly in contact stress analysis (Holzapfel and Stadler, 2006). Despite the importance of the curvatures in spinal mechanics, it appears that little attention has been paid to the facet curvature characterisation and many of the morphological studies of the facet joints were focused more on the facet orientation. However, the variation of the measured facet orientation angles shown in Figure 1.12 indicates that the characterisation of the angle has yet to be fully refined, as various methods were used to quantify the angle. Furthermore, there is still a lack of facet curvature data due to the low number of studies and lack of sophistication in the methods used.

Various methods have been used in the experimental studies in order to characterise the load bearing of the facet joints. The obvious advantage of using the strain gauge is that the facet joints are not disturbed and remain intact while the measurements are made. However, this indirect measurement method is limited to capture only the deformation of the material at the point at which it was attached and is unable to assess the area of load distribution within the joint. Furthermore, the method requires intensive setup and needs disarticulation of the joint for calibration.

Most importantly, every indirect method must be validated with a direct measurement to be useful (Buttermann *et al.*, 1992).

Pressure sensitive film is probably the easiest method to set up and has been used to measure the pressure in the facet joints. The concerns of using this method are that the measurements are made only at the peak contact pressure over one cycle of the experiment and are unable to allow real-time analysis of data. Furthermore, the consistency of the measurement has also be a problem for the film, as illustrated in Figure 1.15 and Figure 1.16 where notable differences of the contact pressures were shown between the left and right facet joints. Apart from the crinkle problem of the film, the experimental result was also reported to be very sensitive to the choice of the film (Harris *et al.*, 1999).

The use of Tekscan measurement system overcomes many of the problems of pressure sensitive film. Specifically, it allows continuous measurements of changing loads, and electronic recording of results. The system also provides real-time, more reliable and repeatable measurement, and has been proved to be more accurate compared to Fuji Prescale film (Harris *et al.*, 1999, Wilson *et al.*, 2003, Wilson *et al.*, 2006). However, there appear to be limited studies which have employed the Tekscan system in the facet joints to evaluate the reliability of the system.

1.5 Articular Cartilage

1.5.1 Introduction

Articular cartilage is a common type of hyaline cartilage. It is a smooth and glistening bluish-white tissue which covers the opposing articular margins of the synovial joints including the spinal facet joints. The main functions of articular cartilage in synovial joints are to transmit loads between the opposing joint surfaces, to distribute the stresses over the subchondral bones, and to provide a low-friction articulation (Mow and Huiskes, 2005). These functions are achieved from the unique material properties possessed by the cartilage. Experiments on articular cartilage are commonly performed to characterise the biomechanical and biochemical properties. The properties are used to enhance tissue engineering developments for cartilage repair and as an input for computational modelling.

1.5.2 Composition and Structure

Articular cartilage consists of two distinct phases which are the fluid and solid phases. The fluid phase is composed of 60-85% water while the solid phase is composed of 15-22% collagens, and 4-7% aggrecan by wet weight (Mow and Huiskes, 2005). The tissue contains four different zones with respect to depth, which from the surface to the subchondral bone are the superficial, middle, deep and calcified zones as shown in Figure 1.18. This composition makes the articular cartilage structure inhomogeneous, and possesses anisotropic and nonlinear properties both in compression and tension.
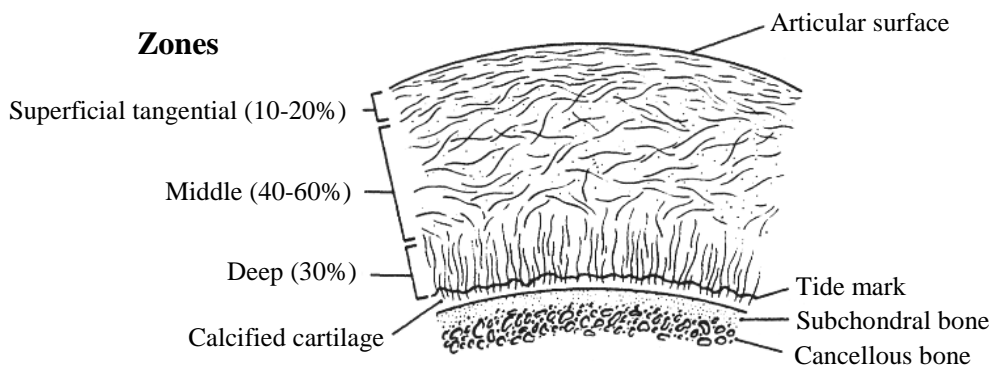
Figure 1.18. Schematic diagram of articular cartilage zones. Adapted from Mow *et al.* (1992).

Collagen is dominated by type II collagen, which makes up 90-95% of the total collagen, and smaller amounts of type I, V, VI, IX, and XI (Eyre, 1991, Hu and Athanasiou, 2003, Mow and Huiskes, 2005). Aggrecan constitutes 80-90% proteoglycans in articular cartilage. Proteoglycans consist of core chain of hyaluronic acid attached with a protein core which contains glycosaminoglycan (GAG) side-chains, mostly keratan sulphate and chondroitin sulphate (Mow and Huiskes, 2005). Aggrecans are elastic macromolecules that give the ability to resist compression and contribute to the durability of the tissue.

The collagens and proteoglycans crosslink together in a network and form the extracellular matrix (ECM) framework as illustrated in Figure 1.19. The negatively charged proteoglycans are tightly bound with the positive charge groups along the collagen fibrils and hyaluronates of the aggregate. In order to maintain the electroneutrality in the cartilage, the total ion concentration inside the cartilage must

be higher than the ion concentration in the surrounding synovial fluid. This imbalance of ions creates an osmotic pressure difference that causes fluid to flow into the cartilage structure to maintain osmotic equilibrium which leads to a swelling pressure. The ability of articular cartilage to perform its physiological functions depends on the structure, the composition, and the integrity of its ECM as the matrix generates the tensile and compressive stiffness of the cartilage (van der Rest and Mayne, 1988, Franz et al., 2001, Mow and Huiskes, 2005).
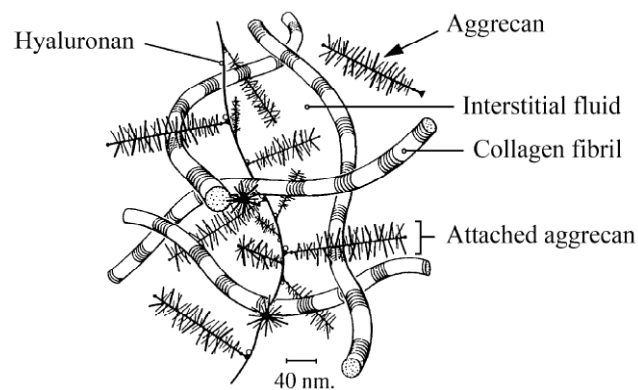
Figure 1.19. A schematic diagram indicating the collagen-proteoglycan matrix in cartilage. Adapted from Mow and Huiskes (2005).

1.5.3 Properties Characterisation

1.5.3.1 Constitutive Modelling

Various constitutive models have been used to describe cartilage from single-phase to biphasic and multiphasic models. The earliest models assumed the cartilage to be single-phase isotropic and linearly elastic (Elmore *et al.*, 1963, Kempson *et al.*, 1971, Hori and Mockros, 1976). This model could describe the mechanical behaviour of the cartilage under static, instantaneous and equilibrium conditions but was unable to describe the time-dependent creep and stress-relaxation behaviours of the cartilage. Then, viscoelastic models were introduced to account for the creep and stress-relaxation behaviour of the cartilage (Hayes and Mockros, 1971, Parsons and Black, 1977, Hayes and Bodine, 1978). However, these models were unable to describe the effect of fluid present in the cartilage.

As the result, a biphasic model was developed to describe the nature of the cartilage in solid and fluid phases (Mow *et al.*, 1980). Both the phases were individually immiscible and incompressible. The solid phase was porous and permeable to fluid flow, which is subsequently responsible for the compressive behaviour of the cartilage. Due to the very low permeability of the cartilage, large drag forces are generated from the fluid flow which maintained the high fluid pressure over a long period of time (Mow and Huiskes, 2005).

With infinitesimal strain and constant permeability, this theory is known as the linear biphasic theory. However, cartilage deformation is non-linear with finite strains and its permeability is dependent on compression. Because of the generality of the formulation, the biphasic model has been expanded to incorporate strain-dependent permeability (Lai and Mow, 1980, Lai *et al.*, 1981, Mow *et al.*, 1984, Holmes, 1985, Holmes *et al.*, 1985, Holmes, 1986), flow-dependent viscoelasticity (Hayes and Bodine, 1978), the intrinsic viscoelasticity of the solid matrix in the biphasic poroviscoelastic theory (Mak *et al.*, 1987) and non-linear finite deformation (Kwan *et al.*, 1984, Holmes, 1986, Holmes and Mow, 1990, Kwan *et al.*, 1990).

In addition, multiphasic models consider the charged nature of the tissue to describe the physiochemical and electrochemical behaviour. The electromechancial theory combines the laws for linear electrokinetic transduction in ionized media with the biphasic theory (Frank and Grodzinsky, 1987). Subsequently, the triphasic theory was developed to incorporate the ion phase in addition to the solid and fluid phase of the biphasic theory (Lai *et al.*, 1991). However, the multiphasic models are rarely used to analyse experimental data because of their complexity.

1.5.3.2 Specimen Preparation

The preparation of articular cartilage specimens depends on the type of test which will be performed in order to characterise the cartilage properties. For compression tests using an indenter, the cartilage specimens have been extracted from the articular surface of the synovial joint that included the underlying bone (Korhonen *et al.*, 2002). However for confined and unconfined compression tests, the full thickness of the cartilage layer was separated from the subchondral bone and then cut according to the size of the confined chamber (Korhonen *et al.*, 2002). Compression tests using an indenter were also performed using *in situ* specimens

where the indentations were performed at different sides of the articular cartilage surface of the synovial joint (Swann and Seedhom, 1989, Athanasiou *et al.*, 1991).

Storage is also an important part of the specimen preparation, especially when the test cannot be performed immediately after the specimen extraction. Generally, cartilage specimens have been kept frozen either at -20 °C (Kempson *et al.*, 1968, Korhonen *et al.*, 2002, Jin and Lewis, 2004) or -80 °C (Athanasiou *et al.*, 1991, Roemhildt *et al.*, 2006). There are conflicting opinions about the effect of freezing on the cartilage biomechanical properties. Hori and Mockros (1976) conducted compression test using an indenter on human articular cartilage at two different storage temperatures, -20 °C and 4 °C, and found differences in shear and bulk modulus. This is supported by another study where freezing at -20 ºC altered the biomechanical properties due to the damage to the extracellular matrix and cells (Willet *et al.*, 2005). However in another study, cartilage that was frozen at -80 °C did not have different material properties as compared to fresh cartilage (Athanasiou *et al.*, 1991). Although testing fresh cartilage will avoid all the storage artefacts, it is inevitable that storage is necessary for some experimental studies of cartilage.

1.5.3.3 Thickness

The thickness of the cartilage varies in different synovial joints in the human body, which could be due to the degree of dynamic loading of the joints. It has also been reported that articular cartilage is distributed inhomogeneously and yields a variable thickness within the major synovial joints of the human (Adam *et al.*, 1998).

Generally, two types of method have been employed to determine the thickness of articular cartilage, which are direct methods such as compression testing, and indirect methods such as imaging techniques. Imaging techniques have been used extensively because the scans were mostly performed without dissecting the cartilage in the scanning process and, more importantly, it can be used clinically. Magnetic resonance imaging (MRI) uses a strong magnetic field and high-frequency radio waves to produce images of organs and structures inside the body (Eckstein *et al.*, 1995, Vanwanseele *et al.*, 2004, Millington *et al.*, 2007), while computed tomography (CT) scanning uses ionising radiation (X-rays) to generate detailed images of structures inside the body (Yoganandan *et al.*, 2003). The accuracy of

both CT and MRI images depends on the magnification and resolution of the equipment. However, MRI is more sensitive than CT scan for the assessment of cartilage since it can detect the fluid content (Eckstein *et al.*, 1998), whereas the CT scan is better at imaging harder tissues such as bone.

Other indirect methods used to measure the cartilage thickness are stereophotogrammetry (Ateshian *et al.*, 1991) and ultrasound (Rushfeldt *et al.*, 1981, Modest *et al.*, 1989). The ultrasound method utilises a pulse-echo ultrasound controlled by a computer, which reflects the boundaries where material density changes. The cartilage thickness is determined by performing a time based correlation of the reflections. The stereophotogrammetry uses prepared specimens where the object is recorded and measured in a two-dimensional photographic image. The thickness is determined from the mathematical computations using both perspective and projective geometry.

The cartilage thickness can also be determined directly using compression testing, where a needle indenter tip is used to penetrate the cartilage until a significant increase in the measured load is obtained indicating that the needle is in contact the subchondral bone (Swann and Seedhom, 1989, Schenck *et al.*, 1994, Athanasiou *et al.*, 1998). The thickness of the cartilage is determined by the difference between the position of the needle when it contacts the cartilage surface and the subchondral bone. Other direct methods have utilised measurement instruments such as the micrometer (Ziv *et al.*, 1993). However, these methods require either the joint capsule or even the articular cartilage layer to be damaged.

Table 1.4 demonstrates the dissimilarity of normal articular cartilage thicknesses both across different synovial joints of the human body and using different measurement methods. The difference was also observed in the facet cartilage between the cervical and lumbar facet joints, and may indicate that the thickness of the facet cartilage varies along the length of the spine.

Table 1.4. Thickness of normal articular cartilage in human synovial joints.

Reference	Method	Cartilage	Thickness (mm)
Athesian, 1991	Stereophotogrammetry	Knee - Patella - Femur - Tibial plateau	3.33 ± 0.39 1.99 ± 0.12 2.92 ± 0.52
Athanasiou, 1991	Compression test using an indenter	Knee - Femoral condyle (lateral) -Femoral condyle (medial) - Patella groove	2.31 ± 0.53 2.21 ± 0.59 3.57 ± 1.12
Eckstein, 1995	MRI	Knee - Patella	$2.80 - 3.16$
Hall, 1980	Radiography	Knee - Femoral condyle (lateral) -Femoral condyle (medial)	3.7 ± 0.8 4.0 ± 0.8
Athanasiou, 1994	Compression test using an indenter	Hip - Femoral head - Acetabulum	$1.03 - 1.84$ $1.06 - 1.83$
Nakanishi, 2001	MRI	Hip - Femoral head	$1.14 - 2.84$
Rushfelt, 1981	Ultrasound	Hip - Acetabulum	$1.0 - 2.0$
Eckstein, 1997	Ultrasound	Hip - Femoral head/Acetabulum	$0.7 - 3.6$
Solowsky, 1992	Stereophotogrammetry	Shoulder - Humeral head - Glenoid	1.44 ± 0.30 2.16 ± 0.55
Vanwanseele, 1997	MRI	Shoulder - Humeral head	1.30 ± 0.06
Graichen, 2000	MRI	Elbow - Humerus - Radius - Ulna dorsal - Ulna ventral	1.35 1.20 1.23 0.99
Schenck, 1994	Compression test using an indenter	Elbow - Radial head - Capitellum	$0.87 - 1.17$ $1.02 - 1.42$
Athanasiou, 1995	Compression test using an indenter	Ankle - Tibial - Talar	$0.95 - 1.30$ $1.01 - 1.45$
Millington, 2007	MRI	Ankle - Talus - Tibia - Fibula	1.34 ± 0.14 1.21 ± 0.14 0.91 ± 0.08
Ziv, 1993	Micrometer	Facet - Superior lumbar spine - Inferior lumbar spine	1.45 ± 0.27 1.12 ± 0.25
Yoganandan, 2003	CT scan	Facet - Upper cervical spine - Lower cervical spine	0.73 ± 0.07 0.47 ± 0.02
Yoshioka, 2007	MRI	Wrist - Ulnar head - Lunate	0.80 ± 0.23 1.10 ± 0.24
Athanasiou, 1998	Compression test using an indenter	Toe - First metatarsophalangeal	0.75 ± 0.21
Al-Ali, 2002	MRI	Foot - Talocrural joint - Talotarsal joint - Intertarsal joint	0.86 ± 0.17 0.72 ± 0.09 0.64 ± 0.18
Koff, 2003	Stereophotogrammetry	Thumb - Trapezium - Metacarpal	0.8 ± 0.2 0.7 ± 0.2

1.5.3.4 Biomechanical Properties

Tensile test and compression test methods are commonly used to determine the biomechanical properties of the cartilage such as elastic modulus (E), Poisson's ratio (v), and permeability (κ). Tensile tests have been utilised to obtain single-phase cartilage properties such as elastic modulus, ultimate tensile stress, fracture stress and tensile fatigue properties (Kempson *et al.*, 1968, Kempson *et al.*, 1973, Weightman *et al.*, 1978, Akizuki *et al.*, 1986, Kempson, 1991). They have also been used to determine the Poisson's ratio of the cartilage in tension (Elliott *et al.*, 2002).

Compression tests are the most frequent method used to determine the biphasic properties of cartilage such as aggregate modulus (H) and permeability. This is because the test set-up can allow the cartilage to be submerged in the fluid during the test. There are three types of compression tests commonly used which are unconfined compression, confined compression, and compression tests using an indenter, as illustrated in Figure 1.20. The confined compression test compresses a disk-like cartilage sample in a confined chamber with a solid platform surface and a water permeable porous loading platen (Hori and Mockros, 1976, Korhonen *et al.*, 2002), while the unconfined test compresses the specimen in between two solid platens (Korhonen *et al.*, 2002). For the compression test using an indenter, the surface of a cartilage sample is compressed using a flat or a spherical indenter (Hori and Mockros, 1976, Athanasiou *et al.*, 1991, Korhonen *et al.*, 2002).
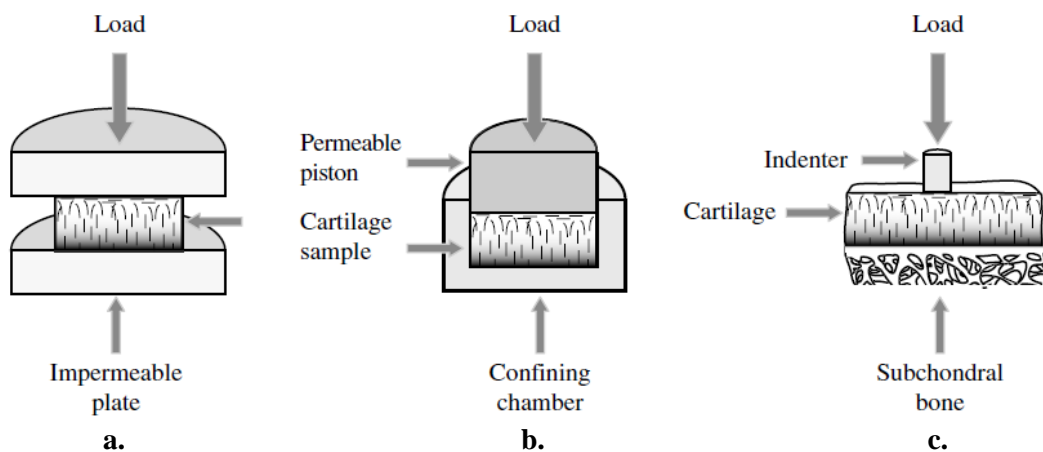
Figure 1.20. Commonly used mechanical testing configurations a. Unconfined compression, b. Confined compression c. Compression test using an indenter. Adapted from Knecht *et al.* (2006).

Extensive experimental studies have been carried out to characterise the linear biphasic properties of the cartilage in human synovial joints as shown in Table 1.5. Although most of the experiments deduced the Poisson's ratio, aggregate modulus and permeability, the elastic modulus is linearly related to Poisson's ratio and aggregate modulus by expression [1] (Mow and Huiskes, 2005),

$$H = \frac{E(1-v)}{(1+v)(1-2v)}$$ ………………………...[1].

The biomechanical properties of articular cartilage were found to vary between different synovial joints of human body. This could be due to the location of synovial joints being subjected to different loading conditions and having different cartilage contours. The mechanical properties of human facet articular cartilage have yet to be characterised.

Table 1.5. Linear biphasic biomechanical properties of articular cartilage in human synovial joints.

Reference	Method	Cartilage	Poisson's ratio, v	Aggregate modulus, H, (MPa)	Elastic modulus, E, (MPa)	Permeability, κ $\times 10^{-15}$ (m^4/Ns)
Armstrong, 1982	Confined Compression	Knee - patella	-	-	0.79 ± 0.36	-
Jurvelin, 2003	Confined/Unconfined Compression	Knee - femoral (parallel) - femoral (tangent)	0.158 ± 0.148 0.180 ± 0.046	0.845 ± 0.383 1.237 ± 0.486	0.581 ± 0.168 0.854 ± 0.348	1.75 ± 1.82 1.26 ± 0.76
Athanasiou, 1991	Compression test using an indenter	Knee - femoral condyle (lat.) - femoral condyle (med.) - patella groove	0.098 ± 0.069 0.074 ± 0.084 -	0.701 ± 0.228 0.588 ± 0.114 0.530 ± 0.094	- - -	1.182 ± 0.207 1.137 ± 0.160 2.173 ± 0.730
Athanasiou, 1994	Compression test using an indenter	Hip - femoral head - acetabulum	$0.013 - 0.058$ $0.011 - 0.097$	$0.679 - 1.816$ $1.072 - 1.424$	- -	$0.781 - 1.101$ $0.710 - 1.133$
Athanasiou, 1995	Compression test using an indenter	Ankle - tibial - talar	$0.02 - 0.08$ $0.02 - 0.06$	$0.94 - 1.34$ $0.92 - 1.25$	-	$0.93 - 1.79$ $0.80 - 1.64$
Schenck, 1994	Compression test using an indenter	Elbow - radial head - capitellum	$0.039 - 0.105$ $0.044 - 0.105$	$0.624 - 0.899$ $0.723 - 0.821$	-	$0.904 - 1.975$ $1.082 - 1.531$
Athanasiou, 1998	Compression test using an indenter	Toe - first metatarsophalangeal	0.07 ± 0.07	0.98 ± 0.50	-	2.02 ± 1.47

1.5.3.5 Biochemical Composition

Biochemical analyses are performed in order to quantify the biochemical composition in the cartilage such as content of water, collagen and proteoglycan. Generally the water content of the cartilage is assessed by measuring the wet weight (ww) percentage of the total cartilage weight (DiSilvestro and Suh, 2002). This was calculated by the percentage difference between the wet and dry weights as a proportion of the wet weight. *In vitro* measurement method using MRI were also utilised to quantify the water content (Lusse *et al.*, 2000). Table 1.6 tabulates the cartilage water content in the human synovial joints that have been characterised in previous studies. Although the percentage of the cartilage wet weight measured using the MRI was slightly lower, the water content was observed to be in a similar range.

Table 1.6. Water content of articular cartilage in the human synovial joints.

Reference	Method	Cartilage	Water, ww %
Armstrong, 1982	Weight measurement	Knee - patella	78.6 ± 3.9
Treppo, 2000	Weight measurement	Knee - tibial plateau - distal femur Ankle - talar	79.0 77.0 75.0
Fetter, 2006	Weight measurement	Knee - femoral condyle Ankle - talar	75.2 72.5
Lusse, 2000	MRI	Knee - tibial plateau - femoral condyle	70.5 ± 2.2 71.2 ± 1.1

The collagen and proteoglycan content can be analysed by qualitative and quantitative methods by using staining techniques. Histology is a qualitative method that studies the tissues by utilising the staining techniques under a light microscope. Hematoxylin and eosin (H&E) staining is the basic and most common histology procedure for cartilage to assess the presence of chondrocytes in the matrix as well as overall organisation (An and Martin, 2003). Histological analysis has also been used to assess the presence of proteoglycans, particularly aggrecan, using safranin O, toluidine blue, and alcian blue to stain the GAG side chains (Franz *et al.*, 2001, An and Martin, 2003). Another qualitative method is immunohistochemistry which allows for the visualisation of the tissue distribution of specific antigens through

antigen-antibody interactions. These interactions allow specific cartilage structure to be visualised such as collagen I, collagen II, collagen III or chondroitin sulphate (Paulsen and Tillmann, 1999).

In order to analyse the matrix content quantitatively, biochemical assays are performed where the proportions of biochemical tissue components can be determined. The total proteoglycan content is determined by measuring the amount of sulphated GAG using dimethylmethylene blue assay (Farndale *et al.*, 1986, Treppo *et al.*, 2000, Fetter *et al.*, 2006), while the hydroxyproline assay is used to obtain the total collagen content in the cartilage (Schwartz *et al.*, 1985, Treppo *et al.*, 2000). It has been reported that the highest content of collagen was found in the superficial zone and the highest concentration GAG was in the deep zone of the cartilage (Fetter *et al.*, 2006).

From previous studies, it appears that limited investigation has been carried out to characterise the biochemical composition of the facet cartilage. The collagen content of human facet cartilage was found to be between 54% and 62% of the total cartilage dry weight depending of the age of the subject (Ziv *et al.*, 1993), whilst the canine facet cartilage was found to be approximately 65% (Elder *et al.*, 2009). In addition, Elder *et al.* (2009) determined the GAG content in the canine facet cartilage and found it to be approximately 15% of the total cartilage dry weight.

1.5.4 Discussion

Experimental tests have been carried out in order to characterise the material properties of cartilage. In cartilage research, it is typically necessary for some period of storage particularly between the harvesting and testing of the cartilage. As well as testing fresh tissue, the cartilage specimens are commonly kept frozen at -20 ℃ and -80 ℃ prior to testing. There are conflicting opinions about the effect of freezing on the biomechanical properties of the cartilage. To date, it appears that no specific protocol for the storage of cartilage has been widely accepted.

Methods for measuring cartilage thickness such as pulse echo ultrasound, needle probe testing and stereophotogrammetry require either the joint capsule or even the cartilage layer to be destroyed. CT scan and MRI imaging techniques

overcome the problems where the assessment of cartilage thickness can be undertaken *in vitro*. Previous studies have shown that MRI provides better cartilage measurement accuracy compared to a CT scan (Eckstein *et al.*, 1998). However, advances have been made in CT scanning techniques which now produce more accurate scans of cartilage (El-Khoury *et al.*, 2004). For direct measurement methods such as compression tests using a needle indenter, validation against imaging is essential to ensure the needle pierces through the calcified cartilage, since it has been reported that the calcified zone is the stiffest cartilage zone as it forms a transitional zone of intermediate stiffness between the cartilage and the subchondral bone (Mente and Lewis, 1994).

Cartilage exhibits biphasic biomechanical properties, with the frictional drag force of interstitial fluid flow being the dominant factor controlling compressive creep and stress-relaxation behaviours. The biphasic theories developed by Mow and co-workers have been widely accepted to represent the biphasic nature of the cartilage compressive behaviour. Although multiphasic models have been introduced, the biphasic model describes the most efficient and idealised of the stress-strain and interstitial fluid flow compressive cartilage behaviour.

For the characterisation of the biomechanical biphasic properties, the compression test using an indenter is preferred compared to confined and unconfined compression tests. This is because of the ease at which the small tissue samples required can be prepared, and speed with which compression test can be carried out. The method has also been advanced to micro-compression testing for small cartilage samples (Li *et al.*, 2007). The same principle was also applied in the development of arthroscopic measurement of cartilage stiffness (Lyyra *et al.*, 1995). In contrast, the confined and unconfined compression tests require the cartilage to be isolated from the subchondral bone which could possibly damage the cartilage. Furthermore, the calcified cartilage is highly integrated with the subchondral bone and cannot be cleanly separated to permit its independent study (Mente and Lewis, 1994).

The aggregate modulus and permeability of normal cartilage are 0.5 to 2.0 MPa and 0.5 to 4.0×10^{-15} m^4/Ns, respectively. However, the cartilage condition such as age, cartilage degeneration and disease are the important factors in the characterisation of the cartilage properties and could produce significant differences in the properties (Armstrong and Gardner, 1977, Lane and Bullough, 1980, Burstein

et al., 2000, Eckstein *et al.*, 2006). Although compressive stiffness is obtained in an compression test using an indenter, computational methods have been incorporated to simulate the compression test in order to characterise the tensile properties (Mow *et al.*, 2000).

As demonstrated in Table 1.4 and Table 1.5, cartilage biomechanical properties are different in the different synovial joints of the human body. Although some studies have been carried out to characterise the facet cartilage behaviour such as thickness (Ziv *et al.*, 1993, Yoganandan *et al.*, 2003), hydration (Ziv *et al.*, 1993) and swelling (Tobias *et al.*, 1992), there is limited information of the facet articular cartilage properties. Therefore, it is crucial to obtain the mechanical properties of facet articular cartilage in order to develop computational models of the facet joint.

1.6 Computational Method

1.6.1 Introduction

The technical difficulties, limitations, and cost involved in *in vitro* and *in vivo* experimental studies as well as ethical concerns have prompted the use of computer modelling studies in various branches of orthopaedic biomechanics. Finite element analysis (FEA) has become a widely used tool in this field. It is a computer method suitable for determining stresses and strains at any given point inside a structure of arbitrary geometric and material complexity. A finite element (FE) models rely on accurate constitutive representation of material characteristics, geometric data, loading characteristics, and boundary and interfacial conditions.

FEA was first introduced to orthopaedic biomechanics in 1972 to evaluate stresses in human bones (Brekelmans *et al.*, 1972). The continuous evolution and availability of affordable powerful computers has increased the complexity of the models under investigation in musculoskeletal systems including the spine. FE models of the spine and its components are being used increasingly to assist in understanding the behaviour of the structures when healthy, diseased or injured, and to examine the effects of different surgical interventions and prostheses (Fagan *et al.*, 2002a, Jones and Wilcox, 2008).

1.6.2 Development of Spinal Models

FE models of the human spine may be classified into two categories: whole-spine models and vertebral-segment models, as shown in Figure 1.21. The whole-spine models normally consist of simplified components of the spine to examine the structural behaviour of the full spinal column (Dietrich *et al.*, 1991, Lee *et al.*, 1995). These models have been used to estimate the forces and stresses in the different elements for different positions of the spine. However, the models are unable to estimate accurate responses of soft tissues and vertebrae, and facet joints have been normally neglected. Therefore, vertebral-segment models have been developed for more detailed representation of spinal materials and geometries (Rohlmann *et al.*, 2006, Schmidt *et al.*, 2007b). In addition, recent advances in image analysis and geometrical reconstruction have also enabled the generation of specimen-specific and patient-specific models (Fagan *et al.*, 2002b, Wilcox, 2007).

a.   b.
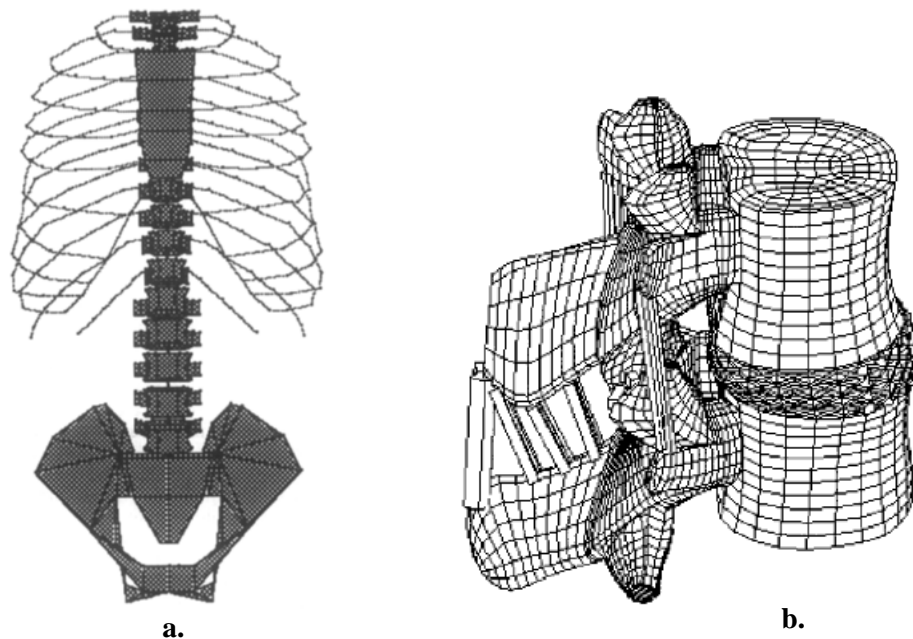
Figure 1.21. Two types of spinal models a. Whole-spine model (Lee *et al.*, 1995) b. Vertebral-segment model (Teo *et al.*, 2004).

1.6.3 Development of Facet Joint Modelling

In the previous FE models, the components that are often modelled in the facet joints are the facet articular processes bone, capsular ligament and cartilage layer.

The geometrical data of the facet processes bone are normally included in the development of the vertebral body model which is commonly obtained either using coordinate measuring machines (Maurel *et al.*, 1997, Teo and Ng, 2001a), MRI (Cyteval *et al.*, 2002) or computed tomography (CT) images (Breau *et al.*, 1991, Wilcox, 2006). The CT technique is the most frequently used due to the flexibility and clarity of bony geometry data. There are software packages that can convert the data from CT images into a format that can be interpreted by engineering computer aided drafting software, which can then be input into commercial FE software.

Although some studies neglected the curvature of the facet articular surface and assumed it to be flat, it has been reported that the curvature plays an important role in the facet joint modelling. A computational study has found that the facet curvature has a strong influence of the contact distribution which affected the shear forces in the facet joint compared with flat geometrical models of facet joints (Holzapfel and Stadler, 2006).

1.6.3.1 Articular Cartilage of the Facet Joint

Since there are limited data of the cartilage in the facet joint, the cartilage geometry and material properties are either assumed or adopted from other synovial joint studies. The cartilage is often neglected and represented using gap elements or spring elements between the two cartilages (Sharma *et al.*, 1995, Schmidt *et al.*, 2008).

The space between two cartilage surfaces has been defined using gap elements (Ueno and Liu, 1987, Sharma *et al.*, 1995), link elements (Shirazi-Adl *et al.*, 1986a), contact gap elements (Shirazi-Adl, 1994) or sliding surface contact elements (Teo *et al.*, 2004). Generally, all these element types were generated using a similar approach, where the thickness of the cartilage layer was assumed on each facet articular surface by incorporating a gap limit between articular surfaces of the facet joints. However, the material properties of the facet cartilage were applied using different approaches.

In the earlier facet joint modelling, the cartilage properties were represented by a constant linear axial and shear spring stiffness (Hakim and King, 1979, Ueno and Liu, 1987). Shirazi-Adl *et al.* (1986, 1987) then incorporated nonlinear stress-strain

characteristics with initial low modulus of elasticity in compression reaching a maximum equal to cortical bone and zero modulus of elasticity in tension. However, Sharma *et al.* (1995, 1998) represented the cartilage properties from an experimental compression stress-strain curve of the cartilage from the bovine knee joint (McCutchen, 1962). This approach was replicated by other researchers in their works to simulate the cartilaginous layer in the facet joints (Teo *et al.*, 2004, Rohlmann *et al.*, 2006, Schmidt *et al.*, 2007b, Schmidt *et al.*, 2008). The values of the cartilage properties applied in the previous FE models are shown in Table 1.7.

Continuum modelling approaches have been implemented to simulate the cartilage in the facet joint using solid elements, synovial fluid using fluid elements, and synovial membrane using membrane elements (Yoganandan *et al.*, 1996, Kumaresan *et al.*, 1998, Natarajan *et al.*, 2000). However, the definitions of the articular cartilage are lacking in these models and although various cartilage formulations have been developed as described in Section 1.5.3.1, the biphasic formulation has yet to be applied in facet cartilage.

Table 1.7. Previous FE models of the facet joint*.

Reference	Facet Joint Components	Element Idealisation	Material Properties
Hakim, 1979	Gap between facet bones	Gap	$k = 1050.8$ N/mm
Ueno, 1987	Gap between facet bones	Gap	$k = 1000$ N/mm
Sharma, 1995 Schmidt, 2007	Gap between facet bones	Gap	$E = 11.1 - 12000$ MPa
Shirazi-Adl, 1986 Shirazi-Adl, 1987	Gap between facet bones	Link	$C =$ max. 12000 MPa; $E = 0$ MPa
Shirazi-Adl, 1994	Gap between facet bones	Contact gap	$C = 75$ MPa
Teo, 2004	Gap between facet bones	Sliding surface contact	$E = 10000$ MPa; $v = 0.3$
Yoganandan, 1996	Articular cartilage	Solid	$E = 3.4$ MPa; $v = 0.4$
Kumaresan, 1998	Articular cartilage Synovial fluid	Shell Incompressible fluid	$E = 10.4$ MPa; $v = 0.4$ $\rho = 1000$ kg/m3
Natarajan, 2000	Articular cartilage	Solid	$E = 11$ MPa; $v = 0.4$

*E: Elastic modulus; C: Compression modulus; k: stiffness; v: Poisson's ratio; ρ: density.

1.6.3.2 Facet Joint Contact Modelling

In the earlier modelling of the facet joint, the joint was represented as a fixed problem until the facet joint contact model was introduced by Shirazi-Adl *et al.* (1986a) in order to articulate a realistic total motion of the vertebral segment. The contact of the joints were modelled using the moving contact problem which was based on the perpendicular distance between the nodal points on the inferior articular surface and triangular plane elements on the superior articular surface as shown in Figure 1.22. The perpendicular distance was computed after each load increment where the contact was assumed to have occurred when:

> *i*. the perpendicular distance between superior and inferior facets were smaller than the specified gap-limit,
>
> *ii*. the projection on the plane of the same lower triangle was inside of its boundary.
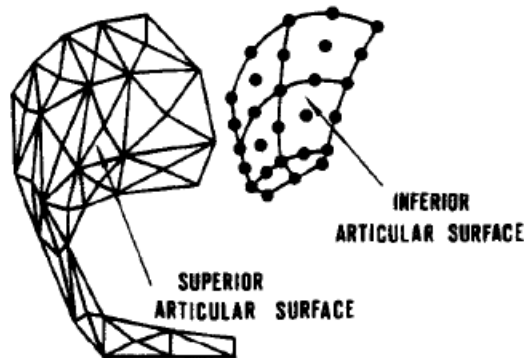
Figure 1.22. Articulating surfaces of segmental model. Adapted from Shirazi-Adl *et al.* (1986a).

However, the contact modelling on the basis of perpendicular distance difference may not be the best to represent the physical situation. In reality, the facet contact areas change or may no longer remain in contact during the application of incremental loading. Therefore, Sharma *et al.* (1995, 1998) developed an algorithm for more realistic representation of facet joint contact known as a nonlinear progressive contact problem. The articulation is modelled by the changing contact areas of the facet articulating surfaces with change in loading.

The nonlinear progressive contact problem has been widely used, but the contact constraints between the articular facets vary and depend on the type of element used. For instance, authors have used contact gap elements (Sharma *et al.*, 1995, Sharma *et al.*, 1998, Rohlmann *et al.*, 2006), nonlinear contact elements (Teo and Ng, 2001b), sliding surface contact elements (Teo *et al.*, 2004), and surface to surface contact elements (Schmidt *et al.*, 2007b, Schmidt *et al.*, 2008). Table 1.8 summarises the development of the facet joint contact modelling in FE models.

Table 1.8. FE model development of facet joint contact modelling*.

Reference	F.E. Model	Facet Articulation	Contact Element	Important Results
Shirazi-Adl, 1986a Shirazi-Adl, 1987 Shirazi-Adl, 1994	3D nonlinear model of L2-L3, L4-L5 motion segments: VB, DC, PC, FC, LG.	Nonlinear moving contact problem	Link	• Pure compression result 1-5% FL. • Combined loads (C+F, C+E) generate large FL. • Axial torsion yield large FL.
Sharma, 1995 Sharma, 1998 Rohlmann, 2006	3D nonlinear model of L3-L4 motion segment: VB, DC, PC, FC, LG.	Nonlinear progressive contact problem	Gap	• High FL in extension and anterior shear loading. • FL is sensitive to facet orientation and gap. • Facet important in torsion and extension but not in flexion. • Facets removal exposes high axial rotations of discs. • Disc degeneration level effected the FL.
Teo, 2001b	3D nonlinear model of C4-C6 motion segment: VB, DC, PC, FC, LG.	Nonlinear progressive contact problem	Nonlinear contact	• Facets and discs shared equal load on high compression. • Facet articulations contribute stability in compression. • Facet joints are important in resisting compression and extension loading.
Teo, 2004	3D nonlinear model of L2-L3 motion segments: VB, DC, PC, FC, LG.	Nonlinear progressive contact problem	Sliding surface contact	• Facetectomy greater than 75% alter the translational displacement and flexibilities of the motion segment.
Schmidt, 2007b Schmidt, 2008	3D nonlinear model of L4-L5 motion segment: VB, DC, PC, FC, LG.	Nonlinear progressive contact problem	Surface to surface contact	• Facets remained unloaded in flexion loadings. • For other load directions, higher loading results higher FL. • Maximum FL obtained when instantaneous centre of rotation at outside disc.

*VB: Vertebral body; DC: Intervertebral disc; PC: Processes; FC: Facet joints; LG: Ligaments; FL: Facet load; C: Compression; F: Flexion, E: Extension.

1.6.4 Modelling of Other Synovial Joints

In the previous studies of synovial joints, it appears that the hip and knee joint modelling have received more attention because of the assessment of total hip and total knee replacement. Although recent FE models have been generated based on subject-specific geometrical data, the cartilage in these models has only been represented as a linear isotropic material or an incompressible neo-Hookean hyperelastic material (Mesfar and Shirazi-Adl, 2005, Anderson *et al.*, 2007, Anderson *et al.*, 2008, Fitzpatrick *et al.*, 2011). These models tend to assume the cartilage to be a solid single-phased material which contradict the fluid-dominated nature of the cartilage. It has been shown that the fluid phase is capable of supporting more than 90% of the load thus resulting in low solid-to-solid contact and hence a lower effective coefficient of friction (Slotz and Ateshian, 1998, Park *et al.*, 2003).

However, recently synovial joint modelling has been developed to incorporate the biphasic material properties of the cartilage in the hip joint (Pawaskar *et al.*, 2011). The model was able to account for interstitial fluid pressurisation which influenced on the contact mechanics of the articular cartilage within the joint. Moreover, surface fluid flow boundary conditions based on a developed contact dependent flow were implemented in order to make the models more realistic.

1.6.5 Discussion

In order to simulate the facet joints, the material properties of the individual components of synovial fluid, capsular ligament, articular processes and articular cartilage, must be defined in the FE model. Since most of the facet joint components have not been characterised, data from other synovial joints of the human body have been adopted in the facet joint model (Teo *et al.*, 2004, Schmidt *et al.*, 2008). These properties could lead to inaccuracy in the results produced from the model, particularly for the important components of the joint such as the articular cartilage, where it has been demonstrated in Table 1.4 and Table 1.5 that the properties of articular cartilage vary across the synovial joints of the human body.

The nature of articular cartilage is that it is dominated by the fluid content, exhibiting 70-85% fluid while the remainder is solid. This results in the fluid pressure having a major role in the load distribution of the cartilage in the facet joint. Although the cartilage constitutive formulations described in Section 1.5.3.1 have incorporated the fluid phase, such as through the use of biphasic theories, and these have been implemented in modelling other synovial joints, it appears that only linear elastic elements have been used to represent the cartilage in the previous FE models of the facet joints (Kumaresan *et al.*, 1998, Natarajan *et al.*, 2000).

The progressive contact problem (Sharma *et al.*, 1995), which modelled the contact between the cartilage layer in the facet joint by the changing of the contact area, has been widely used in a previous FE model to simulate the motion of the facet joint. However, this contact model was unable to capture the fluid flow in the cartilage. Therefore, Pawaskar (2006) has developed a contact dependent flow algorithm by employing the contact stress at the cartilage surface nodes to change the fluid flow conditions on the cartilage surface. The contact model was then applied to the hip joint to investigate the fluid load support in the cartilage (Pawaskar, 2010). This algorithm has been shown to be more realistic in cartilage contact mechanics where it incorporates the biphasic formulation of the cartilage which allowed the fluid in the cartilage to flow during the contact.

In most of the facet joint studies, the FE models were validated by comparison to previous experimental results performed by other researchers (Sharma *et al.*, 1998, Teo *et al.*, 2004, Schmidt *et al.*, 2007b). The comparison among studies on spinal motion segments might not be accurate due to the difference of the specimen geometry where the size and orientation of the articular facets may vary from specimen to specimen as described in Section 1.4.2. Therefore, the use of specimen-specific FE models, both in terms of morphology and bone quality, could increase the accuracy of the FE model (Wilcox, 2006). The large number of modifications in the facet representation in FE models in recent years suggest that facet joint modelling is not yet completely satisfactory.

1.7 Animal Models

1.7.1 Introduction

In vitro models consisting of cadaveric spine specimens are useful in providing basic understanding of the functioning of the spine. One problem is the difficulty in obtaining fresh frozen human specimens, especially from the younger population. Another problem with the use of human specimens is the large variation in geometry and mechanical properties due to differences in age, sex, bone quality, and disc degenerative changes. These disadvantages of using human specimens have prompted the use of alternative animal models.

Animal models, such as porcine, bovine and ovine, have been commonly used for *in vivo* and *in vitro* spinal research (Allan *et al.*, 1990, Eggli *et al.*, 1992, Gurwitz *et al.*, 1993, Ahlgren *et al.*, 1994). Such animal specimens are more readily available and have more uniform geometrical and mechanical properties. To mimic the clinical situation, an appropriate animal should have as similar spinal characteristics to those in humans as possible.

1.7.2 Skeletal Maturity

Skeletal maturity is a measure of development incorporating the size, shape and degree of mineralisation of bone to define its proximity to full maturity. Skeletal maturity could become an important factor for the animal model if studies of the morphology and the synovial joints are to be carried out. This is because the growth plate, which is normally found at the end of the long bones including the vertebral body, will stop growing and form a new bone when the maturity age is reached. Table 1.9 shows the age of the skeletal maturity of the animal models that are often used in the spine research (Reinwald and Burr, 2008).

Table 1.9. Comparisons of skeletal maturity for animal models (Reinwald and Burr, 2008).

Criteria	Human	Bovine	Canine	Porcine	Hircine	Ovine
Skeletal maturity (yr)	18-25	2-4	1.3	>2.5	2-3	3
Life span (yr)	~70-80	-	10-12	10-15	10-15	10-15

1.7.3 Anatomy

Anatomical studies have been carried out to analyse the differences and similarities of the vertebrae between human and animal spines, so as to gauge the extent to which animal models resemble the human spine. Typically anatomical parameters of the vertebrae have consisted of the dimensions of vertebral body, spinal canal and pedicle, as shown in Figure 1.23.

A	Vertebral body width upper
B	Vertebral body width lower
C	Spinal canal depth
D	Spinal canal width
E	Pedicle width
F	Vertebral body depth
G	Vertebral body width
H	Vertebral body depth upper
I	Vertebral body height anterior
J	Vertebral body height posterior
K	Pedicle height
L	Vertebral body depth lower
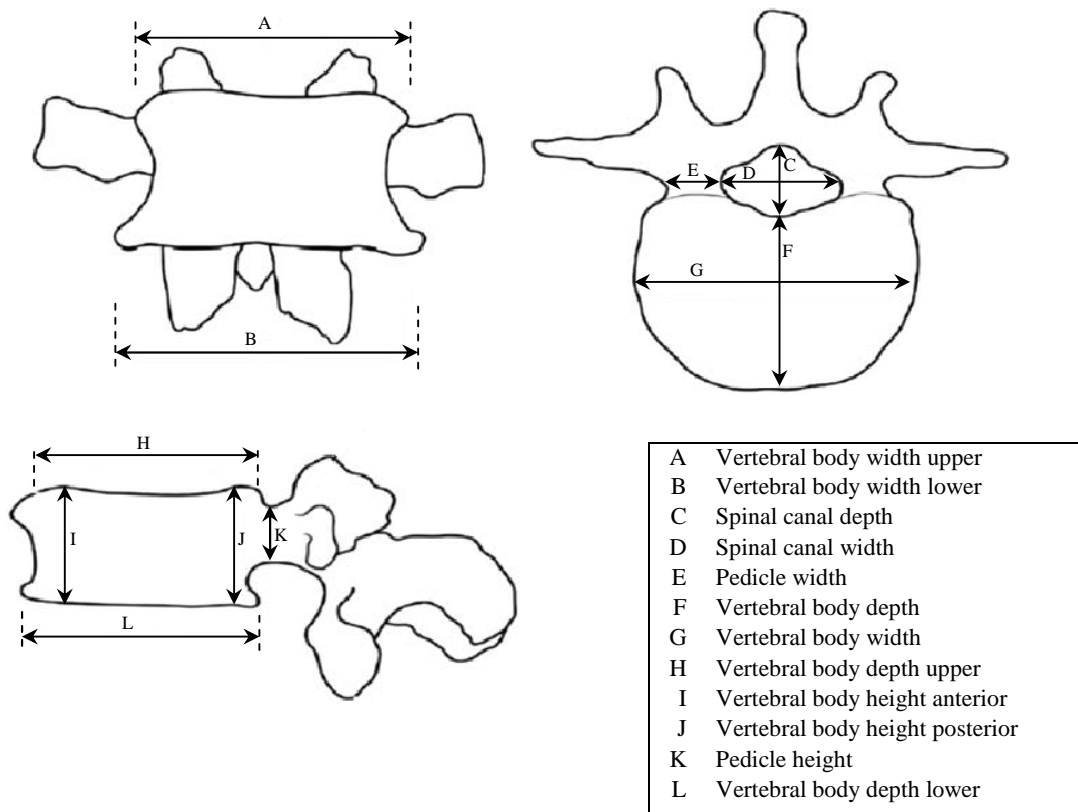
Figure 1.23. Typical anatomical parameters of vertebra. Adapted from Sheng *et al.* (2010).

In previous studies, various animal studies have been carried out to determine the anatomical data of the vertebrae. Table 1.10 shows the average of dimensional difference percentage comparisons between the animal and human vertebrae, while Table 1.11 shows the dimension trends compared to human vertebrae. Only the bovine (Cotterill *et al.*, 1986), porcine (Dath *et al.*, 2007) and ovine (Wilke *et al.*, 1997b) were included in these tables since these animals are the most often used in spinal research.

Table 1.10. Average dimensional difference percentage to the human vertebrae (Sheng *et al.*, 2010).

	Vertebral Body (%)	Spinal Canal (%)	Pedicle (%)
Cervical			
Ovine	85-320	57-74	200-500
Porcine	-	-	-
Bovine	-	-	-
Thoracic			
Ovine	61-190	45-79	146-164
Porcine	50-121	57-83	93-128
Bovine	-	-	-
Lumbar			
Ovine	57-181	44-50	57-250
Porcine	50-159	61-76	66-157
Bovine	61-135	76-95	83-121

Table 1.11. Dimension trend compared to the human vertebrae (Sheng *et al.*, 2010).

	Vertebral Body			Spinal Canal		Pedicle	
	width	depth	height	width	depth	width	height
Cervical							
Ovine	Opposite	Opposite	Opposite	Similar	Similar	Similar	Opposite
Porcine	-	-	-	-	-	-	-
Bovine	-	-	-	-	-	-	-
Thoracic							
Ovine	Similar	Opposite	Similar	Similar	Opposite	Similar	Similar
Porcine	Similar	Similar	Similar	Similar	Opposite	Similar	Similar
Bovine	-	-	-	-	-	-	-
Lumbar							
Ovine	Similar	Similar	Similar	Similar	Similar	Similar	Opposite
Porcine	Similar	Similar	Similar	Similar	Similar	Opposite	Similar
Bovine	-	-	-	-	-	-	-

Distinct anatomical differences of the vertebra dimensions were found between the human and animal spines as tabulated Table 1.10. Based on such variation of these animal models, it is difficult to interpret which species is the most suitable to be used to represent the human spine. However, similar trends in terms of the vertebra dimensions were found at certain spine regions, as shown in Table 1.11. Although it may not be definite in which animal model is the most appropriate from the anatomical data, the dimensional trend could be an important criteria for the selection.

1.7.4 Range of motion

Range of motion (ROM) studies have been carried out to examine the biomechanical behaviour of the vertebral segments in flexion, extension, axial rotation and lateral bending directions. The ROM was defined as the angular deformation at the maximum load needed to flex, bend and rotate the specimen (Wilke *et al.*, 1996). In the animal studies, skeletally immature bovine (Wilke *et al.*, 1996) and mature ovine (Wilke *et al.*, 1997a) spines were used to compare the ROM with the human spine. Although differences were found at certain vertebral segments, generally similar ROM were observed in all directions compared to human spine. Based on these studies, these species were suggested as appropriate animals for *in vitro* biomechanical models of the human spine.

In addition, the ROM for skeletally immature porcine spines were also investigated (Busscher *et al.*, 2010). It was reported that the segments were more flexible and a larger ROM was found compared to the human spine. The use of the immature pig, aged between five to six months old, could possibly be the reason for the differences in the flexibility. But the choice of age is limited by the availability of the tissue, and older porcine specimens are less frequently available. However, the ROM may not be the only criteria, as other selection choices for the animal model may have to take into consideration and this will depend on the interest of the study.

1.7.5 Discussion

Basic spine research and preclinical testing of new surgical methods often involve animal experiments because most tests cannot be carried out on humans or the availability of human specimens is limited. The spines from animal species such as pig, cow and sheep have often been used for *in vivo* and *in vitro* experimental studies. Although there have been concerns about the horizontal position of the quadruped spine, theoretical considerations show that the spine of the quadruped animal is mainly loaded along its long axis, similar to the human spine (Smit, 2002).

The selection of the animal model depends mainly on the application and the research area, where the differences in the skeletal maturity, anatomy and ROM between the species need to be considered. In addition, several factors such as

availability, costs, breeding and growth should be taken into account. For instance, for the *in vitro* experimental studies where skeletal mature animal model is required, the ovine spine could be chosen since there is limited availability of mature porcine and bovine spines. Therefore in order to select an animal model for spine research, all the selection criteria have to be considered in which the research interest will be the main priority.

1.8 Overall Summary

The high prevalence of low back pain results in high healthcare costs and also in working hours lost. The facet joints are well known to be a source of low back pain due to the influence of high mobility and large forces which can cause significant degenerative changes.

From the previous studies, limited facet cartilage data has been found to characterise the cartilage biphasic properties of the facet joint. This has led to the inaccurate application on the cartilage properties of the facet joint in the FE models. Furthermore, the cartilage was seen to be represented as a single-phased material, which contradicts the nature of the fluid-dominated behaviour. Therefore, the implementation of the biphasic properties for the cartilage in the facet joint is needed in order to simulate the facet joint in a more realistic manner.

In the spinal research, animal models have been used in *in vivo* and *in vitro* experimental studies since more uniform geometry and material properties conditions could be obtained compared to human cadaveric spine specimens. Although anatomical and range of motion studies of the animal models have been carried out, the suitability of the animal models to represent the human spine specifically for facet joint studies has yet to be investigated.

1.9 Aims and Objectives

1.9.1 Aims

The overall aim of this study is to characterise the anatomical and biomechanical behaviour of the spinal facet joints and evaluate the use of an ovine facet joint model as a representation of the human facet joint.

1.9.2 Objectives

The specific objectives of this study were:

- To develop a methodology to characterise the facet articular radius using an imaging method to evaluate ovine and human specimens.
- To investigate alternative storage methods for facet joint cartilage specimens.
- To perform compression tests using an indenter on ovine articular cartilage from the facet joint to determine the biomechanical behaviour.
- To determine the biomechanical properties of the cartilage using finite element models incorporating the linear biphasic formulation.
- To investigate the effect of the FE model sophistication, from idealised axisymmetric to specimen-specific on the derived cartilage properties.
- To examine the effects of the subchondral bone architecture on the derived cartilage properties.
- To apply the methods developed to human facet cartilage and determine the most appropriate methodology for future studies.

Chapter 2: Methods – Morphological Study of the Facet Joint

2.1 Introduction

This chapter will describe the materials, equipment and experimental methodologies employed to study the morphology of the facet joint. The first two sections describe the method used to prepare the specimens and the imaging methods to scan the specimens. This is followed by the facet joint morphological measurement methods including a new improved method to measure facet articular radius and facet orientation angle, which are based on the scan images. The final section outlines the statistical analysis used in this study.

2.2 Specimen Preparation of Ovine Vertebral Segment

All the vertebral segments were acquired from the spines of three female Texel sheep ($n=3$) aged between four and five years and weighing between 25 kg and 31 kg. A surgical scalpel was used to dissect the spines into two-vertebra segments from the lumbar region (L1L2, L3L4, L5L6), thoracic region (T2T3, T4T5, T6T7, T8T9, T10T11, T12T13) and cervical region (C2C3, C4C5, C6C7). During the dissection process, excessive connective tissues were removed whilst the facet joints between the vertebrae were preserved, including the surrounding tissues. Following preparation, the vertebral segments were stored at -20°C within two weeks prior to scanning (Section 2.3). Examples of the vertebral segments from each region are shown in Figure 2.1.
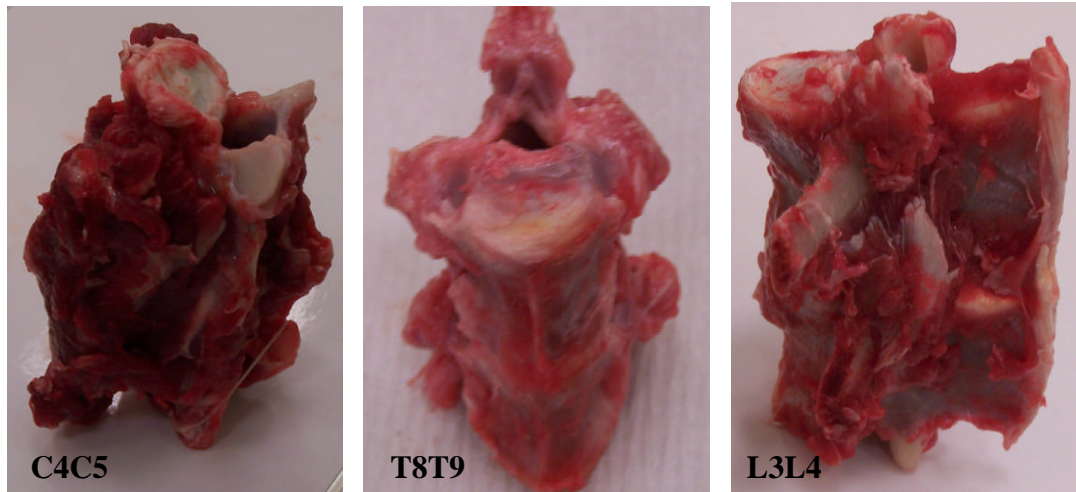
Figure 2.1. Ovine two-vertebra segments at different spinal regions.

2.3 Micro Computed Tomography Imaging

Micro computed tomography (µCT) is a medical imaging method that uses x-ray imaging and computed tomography to produce three-dimensional (3D) images of very high resolution. In this study, a specimen µCT system was employed (µCT80 Scanco Medical AG, Zurich, Switzerland) with a maximum resolution of 20 µm. The system operates by rotating the specimen between an x-ray source and sensor to capture a series of projection images which are then reconstructed to form a 3D image of the specimen. In this study, the scan data was subsequently converted to a series of two-dimensional slices through the specimen and saved in .tiff file format for the purposes of measurement and model development.

The µCT imaging technique was performed with the objective to study the morphology of the spinal facet joints. The following section will describe the scan specification and the set-up applied in this study.

2.3.1 Scan Set-up for Ovine Vertebral Segment

Ovine segments were prepared as described in Section 2.2 and imaging was performed at 70 kV pulse voltage, 114 µA current, and 300 ms integration time with a resolution of either 60 µm or 74 µm. The vertebral segments were placed in a vertical position during the scanning, with the upper endplate plane parallel to the transverse scan plane so as to obtain transverse cross-sectional image slices, as

shown in Figure 2.2. This also aligned the longitudinal axis of the vertebral segment with the vertical axis of the µCT specimen container. The orientation of the specimen in the specimen container was considered important for obtaining consistency in the images produced. Therefore, the orientation was made such that the spinous process of the vertebra was parallel to the walls of the x-ray tube, which vertically orientated the spinous process in the image. In order to ensure the position and orientation of the vertebral segment were maintained during the scanning process, dry foam (household sponge) was wrapped around the vertebral body and spinous process to avoid any movement.
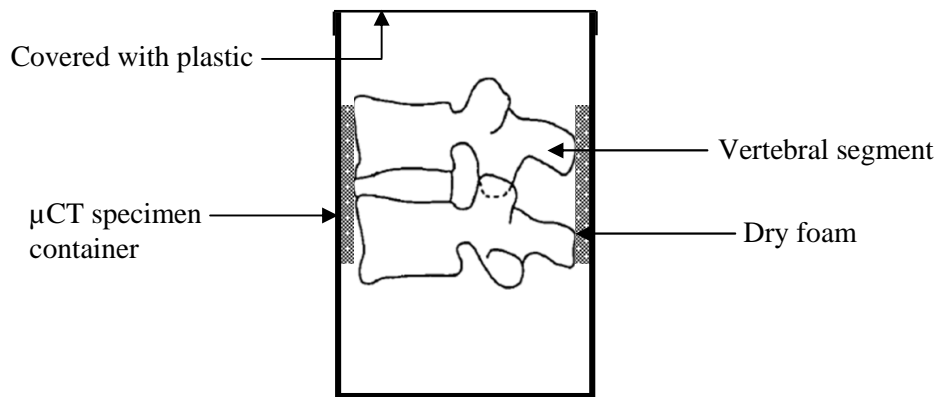
Figure 2.2. Schematic diagram of scan setup for the ovine vertebral segment.

2.3.2 Scan Set-up for Human Vertebra

The human vertebra scan data was obtained by Dr. S. Rehman (iMBE, University of Leeds). The specimens were acquired from the Medical School, University of Leeds and were aged between 81 and 102 years old. The vertebrae were from the lumbar region at the vertebral level of L1 (*n=2*), L2 (*n=1*), L3 (*n=3*) and L4 (*n=1*).

The vertebrae were scanned at 70 kV pulse voltage, 114 µA current, and 300 ms integration time with the resolution of 74 µm. Since the human vertebrae were larger than the ovine, the specimens were oriented such that the upper endplate plane was perpendicular to the transverse scan plane and parallel to the wall of x-ray tube, as shown in Figure 2.3. In some cases, either the transverse or spinous

processes were trimmed, without disruption of the facet articular region, to accommodate the vertebra within the μCT specimen container.
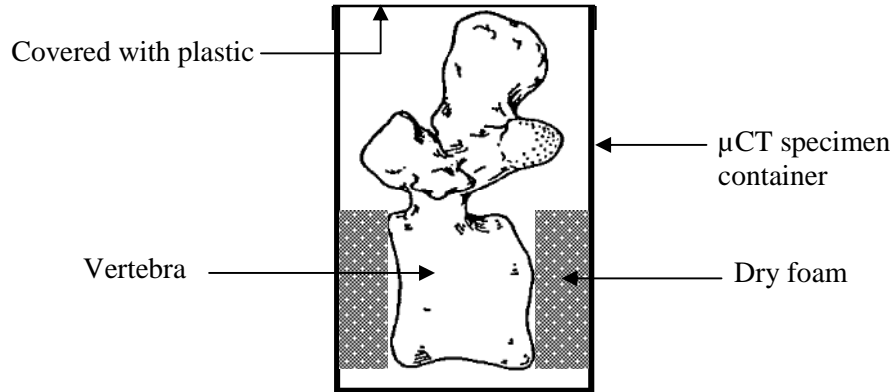
Figure 2.3. Schematic diagram of scan setup for the human vertebra.

2.4 Morphological Measurement

In this study, the morphological measurements were based on μCT images with the objective to characterise the vertebral dimensions, the facet articular radius, and the facet orientation angle. The scan data was converted to .tiff file format in order to analyse and evaluate the images.

2.4.1 Vertebral Dimensions

The measurements of the vertebral dimensions were made at the superior level of the vertebral body so as to obtain the maximum width (W) and depth (D). Two extreme points of measurement were manually selected from the scan images using image visualisation and measurement software (MATLAB V7.8.0 R2009a, MathWorks Inc, MA, USA) to obtain the coordinates, as shown in Figure 2.4. The distance between the two points was then converted to the actual distance using the scan resolution pixel size.
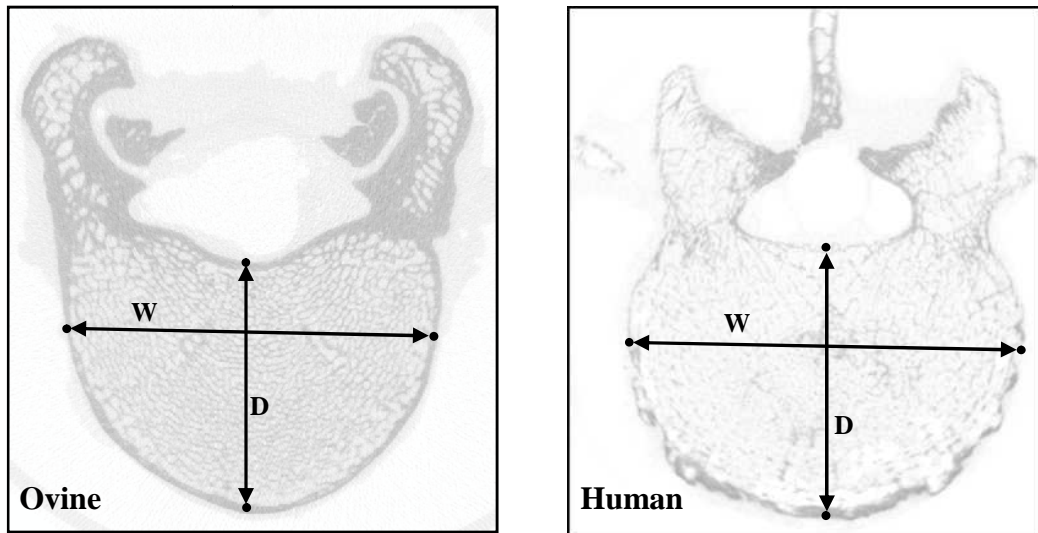
Figure 2.4. Measurements of vertebral body width (W) and depth (D).

2.4.2 Facet Joint Articular Radius

Both the superior and inferior facet articular radii were quantified using a custom-written algorithm (MATLAB V7.8.0 R2009a, MathWorks Inc, MA, USA). The transverse scan images were selected around the facet joint at every 0.6 mm to establish the average radius. In order to segment the contour rapidly, the image was sectioned into either left or right facet joints. The facet articular contour was accordingly segmented using an active contour segmentation method (Chan and Vese, 2001). Then, both the superior and inferior articular edges were detected using the *Canny* method available in the software, which is considered to be the most effective edge detector (Gonzalez *et al.*, 2004). Subsequently, two boundaries were created at the superior and inferior facet articular curvatures to extract the points along the curvatures. A circle was then fitted to each set of points using the least-squares method, in order to determine the radius for the superior and inferior facet articular regions. Figure 2.5 shows the process followed in the program to determine the radius.
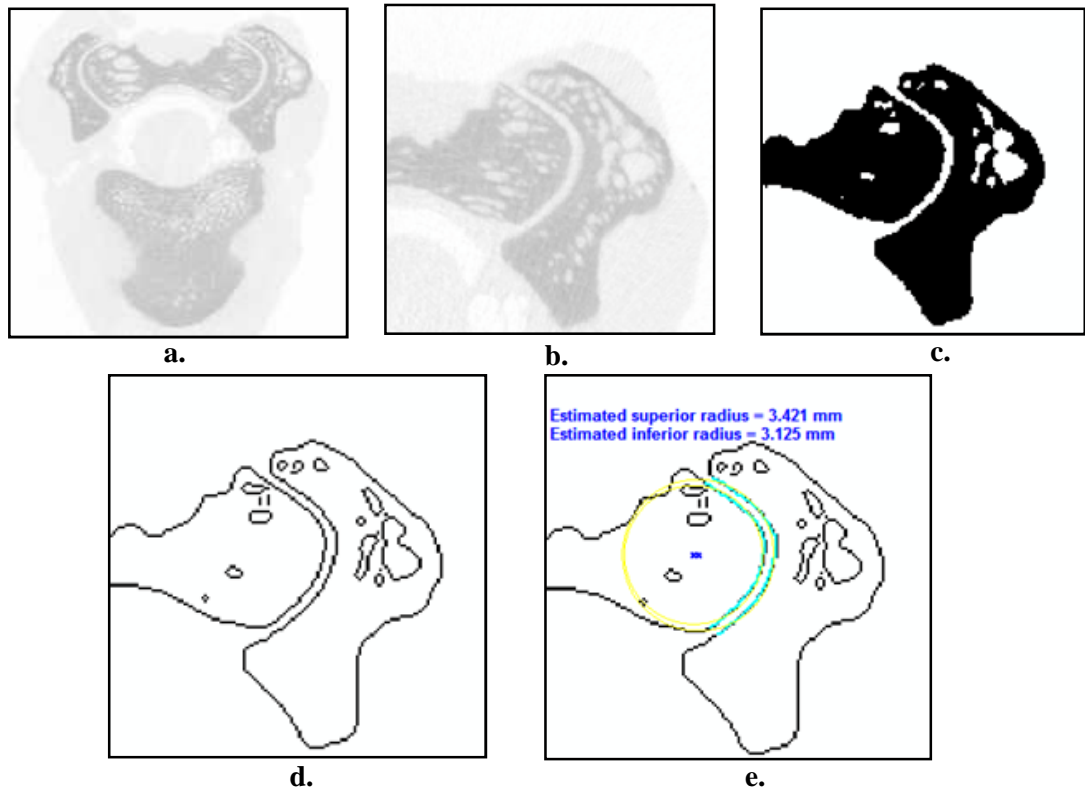
Figure 2.5. MatLab program steps to determine facet articular radii a. The µCT image slice, b. The selection of the facet region, c. The contour segmentation, d. The edge detection, e. The boundary trace and circles fit.

2.4.3 Facet Joint Orientation Angle

The transverse facet orientation angle was measured according to the work carried out by Masharawi *et al.* (2004) to enable comparison with previous data. The transverse scan images were selected around the facet joint at every 0.6 mm so as to obtain the average facet angle. From the scan image, two lines were created: one was constructed through the spinous process and midpoint of the vertebral body, whilst the other was created through two extremities points of the facet joint, as adopted from the Masharawi *et al.* (2004) study. The angle between these two lines determined the transverse facet angle, as shown in Figure 2.6.
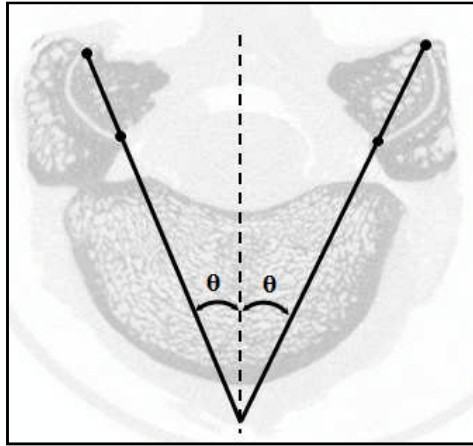
Figure 2.6. Facet orientation angle measurement.

2.5 Statistical Analysis

For the quantitative experimental data, mean and standard deviations were calculated and displayed as mean ± standard deviation (SD) unless stated otherwise. The following statistical methods were used in this study.

Student t-test

The facet articular radius and facet joint angle were statistically evaluated using the Student t-test (*p<0.05*) in order to evaluate the statistical significance between the left and right facet joint measurements. If no significant difference was found, the left and right measurements were averaged together to obtain the mean and standard deviation for both facet articular radius and facet angle. All the tests were performed using Microsoft Excel 2007.

Linear Regression Analysis

Linear regression analyses (*p<0.05*) were performed to observe linear correlations between the facet orientation angle and facet articular radius, between the facet orientation angle and axial rotation, and between the facet articular radius and axial rotation. A graph and coefficient of determination (R^2) value are presented for all regression analyses using Microsoft Excel 2007.

2.6 Summary

This chapter outlined the methodology used to characterise the morphology of the facet joint. A new methodology, which was improved from the method used previously, was developed to acquire comprehensive data of the vertebral body dimensions, facet joint angle, and facet articular radius. The measurements were carried out using image visualisation and measurement software (MATLAB V7.8.0 R2009a, MathWorks Inc, MA, USA) based on the μCT scan images. The methodology was for both ovine and human specimens.

Chapter 3: Methods – Characterisation of Facet Cartilage Biomechanical Properties

3.1 Introduction

This chapter will describe the materials, equipment, experimental methodologies and computational methodologies employed to characterise the biomechanical properties of the facet cartilage. The first two sections describe the methods used to prepare the specimens and the imaging methods to scan the specimens. In order to characterise the facet cartilage biomechanical properties, both experimental and computational methods were employed. Therefore, detailed descriptions of the creep compression test using an indenter and finite element models are presented including a novel specimen-specific modelling method. The final section outlines the statistical analysis used in this study.

3.2 Material and Specimen Preparation

3.2.1 Phosphate Buffered Saline

Throughout this study, phosphate buffered saline (PBS) was used for irrigation purposes during the dissection procedures and also to equilibrate the cartilage during the compression tests. It was prepared using a PBS tablet (MP Biomedicals, Solon, USA) dissolved in sterile distilled water at the ratio of one tablet to 100 ml, as recommended by the manufacturer (www.mpbio.com). The PBS tablets were composed of inorganic salts, as shown in Table 3.1.

Table 3.1. Formulation of the PBS tablets used in this study.

Component	Concentration (mg/L)	Molecular Weight (Da)	Molarity (mM)
Potassium Chloride (KCl)	200.0	74.55	2.68
Potassium Phosphate Monobasic (KH$_2$PO$_4$)	200.0	136.09	1.47
Sodium Chloride (NaCl)	8000.0	58.44	136.89
Sodium Phosphate Dibasic (Na$_2$HPO$_4$)	1150.0	141.96	8.10

3.2.2 Ovine Facet Cartilage Pin

The connective tissue surrounding the facet joints was first removed with a surgical scalpel in order to expose the facet joint and make the joint easy to separate. As the joint was separated, the facet cartilage surfaces were irrigated with PBS in order to wash away any synovial fluid and to further avoid any potential dehydration of the cartilage. The cartilage surface was then visually inspected for any obvious signs of damage, disease or scalpel cuts, and promptly rejected in the case of any such discoveries.

The cartilage pin specimens were plugged using hand-held tools and an electric drill, as shown in Figure 3.1. The 4 mm diameter cylindrical pin specimens were only plugged from facet joints of the cervical spine because the cartilage surfaces here possessed a sufficient area and flatness compared with the other regions. Throughout the extraction process, the whole of the joint surfaces were kept hydrated with regular PBS washes.
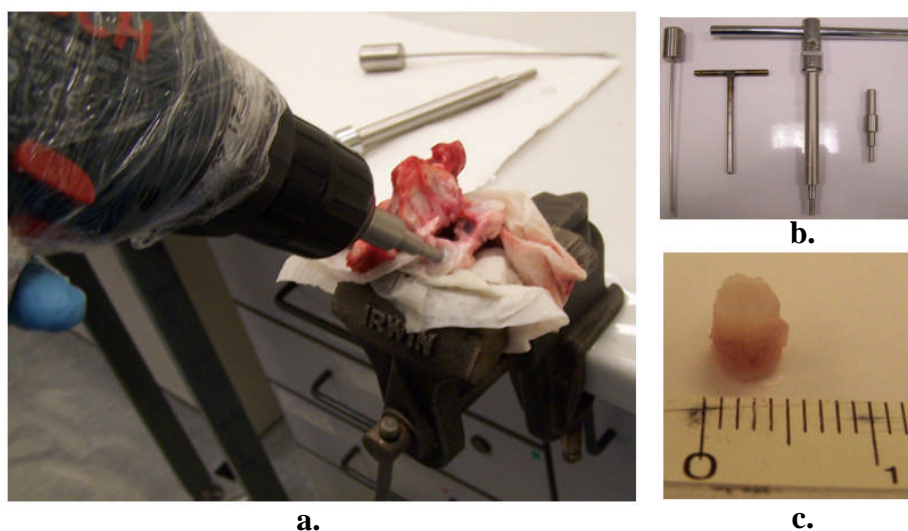
Figure 3.1. a. The hand drill on facet surface used to extract the specimen, b. Tools used to plug out the pin specimen, c. The cartilage pin specimen.

The cartilage pin specimens were prepared in three different conditions with the intention of examining the storage effects on the cartilage biomechanical properties. Firstly (*fresh*, *n=10*), the specimens were extracted from fresh joints and either tested following the extraction, or otherwise stored at 2ºC in moist conditions and tested within 24 hours. A schematic diagram that illustrates the storage method to maintain cartilage specimens in moist conditions is shown Figure 3.2. Secondly (*frozen joint*, *n=5*), the intact facet joints were subjected to a freeze-thaw cycle, and the cartilage pins were subsequently extracted from the joint. Thirdly (*frozen pin*, *n=4*), the cartilage pin specimens were extracted from fresh facet joints and then subjected to a freeze-thaw cycle. Notably, all the frozen joint and frozen pin specimens were frozen at -20 °C within two weeks and equilibrated in PBS for 60 minutes prior to testing.
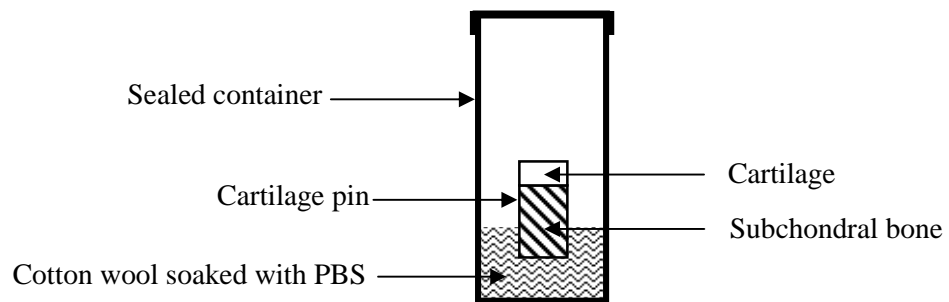
Figure 3.2. Schematic diagram of the cartilage specimen storage in a moist environment.

3.3 Micro Computed Tomography Imaging for Facet Cartilage Pin

The μCT imaging technique described in Section 2.3 was performed on the cartilage pin specimens to measure the cartilage thickness and to further provide geometrical data for the development of the three-dimensional computational model of the cartilage pin. The specimens were prepared as described in Section 3.2.2 and the scan was performed at 70 kV pulse voltage, 114 μA current, and 300 ms integration time with a resolution of 20 μm. The cartilage pin was positioned vertically in the μCT specimen container, as shown in Figure 3.3. Dry foam was used to wrap around the subchondral bone so as to hold the cartilage pin in place and thereby avoid any movement during the scanning process. The cartilage had to be exposed in order to produce a clear image of the tissue. Furthermore, the contact

between the cartilage and the foam had to be avoided to prevent the fluid from seeping through the foam and consequently affecting the cartilage image produced. PBS-soaked cotton wool was placed at the bottom of the μCT specimen container and the top of the tube was covered in order to maintain moisture and avoid any possibility of cartilage dehydration during the scanning process.
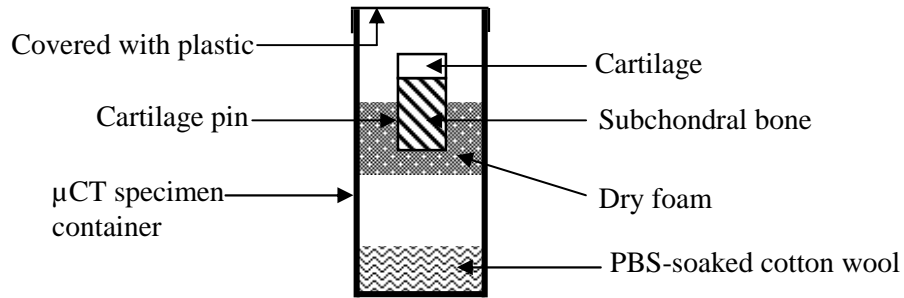
Figure 3.3. Schematic diagram of scan setup for the cartilage pin.

3.4 Compression Test Procedure

3.4.1 Apparatus

The apparatus used to perform compression test and thickness measurements of facet joint articular cartilage is shown in Figure 3.4. The equipment comprised of a shaft attached to a force transducer with a 2 mm diameter spherical indenter at its lower end. The overall weight of the shaft assembly was 0.24 N. The movement of the shaft was monitored by linear variable differential transformer (LVDT) mounted at the top of the shaft. At the same time, the force was detected via a piezoelectric force transducer fitted above the indenter. The data from the LVDT and force transducer were accordingly transferred through an analogue-to-digital converter and stored in a computer using data acquisition software (LabVIEW 8.0, National Instruments Corporation, Austin, TX, USA).

In order to avoid any movement during the testing process, the cartilage pin was press-fitted in a specimen holder. The holder was then fitted in a fix-based fixture containing a PBS solution to hydrate the cartilage during the test.
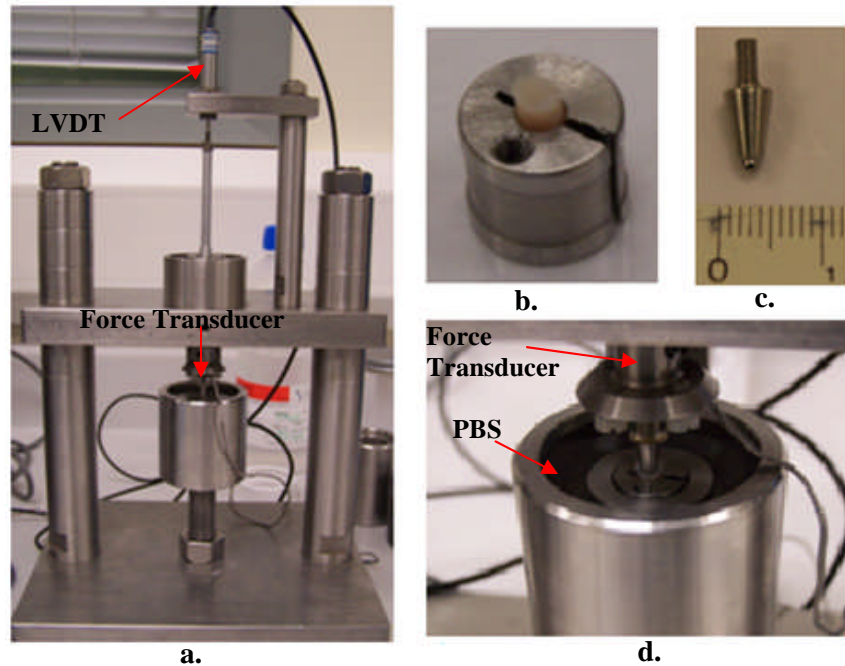
Figure 3.4. Apparatus for compression test a. Compression test rig, b. Cartilage pin specimen fitted in the specimen holder, c. 2mm diameter of the spherical indenter, d. Close view on the indented specimen.

3.4.2 Calibration Procedure

Calibration of the LVDT and force transducer was conducted prior to performing the compression tests, and at intervals during the testing programme. This was undertaken to obtain the calibration factor for the displacement and the load. The calibration factors were used to convert from the voltage data to the actual distance and load produced from the LVDT and force transducer during the test.

The displacement LVDT was calibrated using standard stainless steel step height gauges. The changes in the output voltage from the LVDT were recorded during the addition or removal of the step height gauges whilst maintaining the weight during the process. The data was plotted in a linear regression fit of the voltage against the displacement which produced the linear line equation as a calibration factor, shown in Figure 3.5a.

In order to calibrate the force transducer, the displacement of the indenter was held constant and the load increased gradually by addition of dead weights. The voltage data was recorded, and a linear regression fit graph plotted between the voltage and the load so as to obtain the calibration factor, as shown in Figure 3.5b.

This process was repeated three times to gather average values and also to evaluate the repeatability of the measurement.

a.

b.
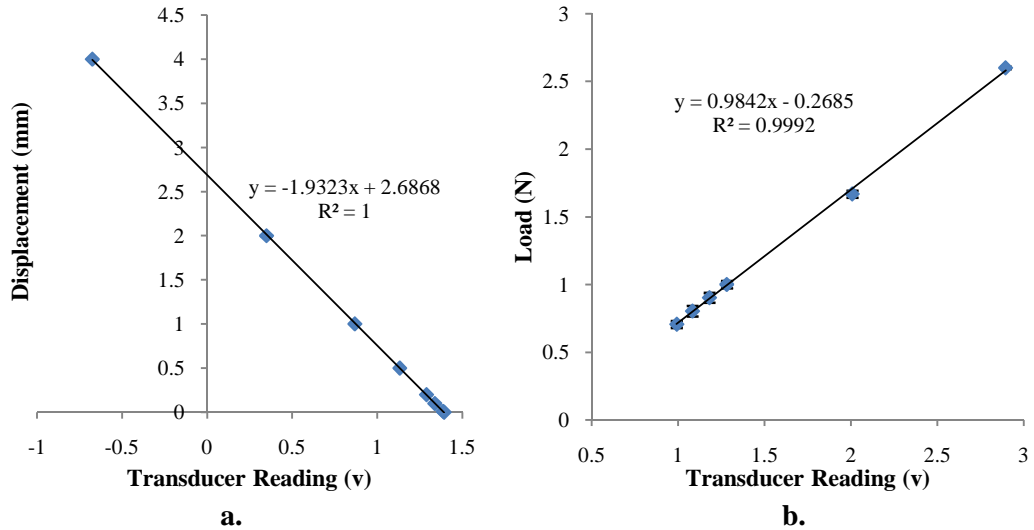
Figure 3.5. Graphs represent the mean (± SD) of the measurements taken in the compression apparatus calibration. a. Displacement calibration, b. Load calibration.

3.5 Creep Compression Test

Creep compression tests using an indenter were performed to provide experiment data to characterise the biphasic properties of the cartilage. The tests were carried out using a 2 mm diameter spherical indenter subjected to 0.24 N compression force. In addition, a 6.3 mm diameter indenter were also utilised on fresh cartilage specimen (*n=6*) to investigate the effects of the indenter size on the derived cartilage biphasic properties. Throughout the test, the cartilage pin was submerged in the PBS solution to prevent the cartilage from becoming dehydrated.

The indenter was set as close as possible to the cartilage surface; this was confirmed by observing the load indicator and establishing whether the indenter has made any contact with the cartilage surface. The indenter was then released and the displacement and force readings were recorded continuously at a sampling frequency of 0.01s for 50 minutes, by which time the displacement had reached equilibrium. There was significant noise in the deformation readings so the data were evaluated using a statistical software package (Origin 8, OriginLab

Corporation, MA, USA), in order to fit a curve of best fit to the experiment data (Figure 3.6) using the exponential function [2],

$$y = y_0 + A_1 e^{-(x-x_0)/t_1} + A_2 e^{-(x-x_0)/t_2}$$ .... [2]

where y_0 is offset, x_0 is centre, A_1 and A_2 are amplitudes, and t_1 and t_2 are decay constants.
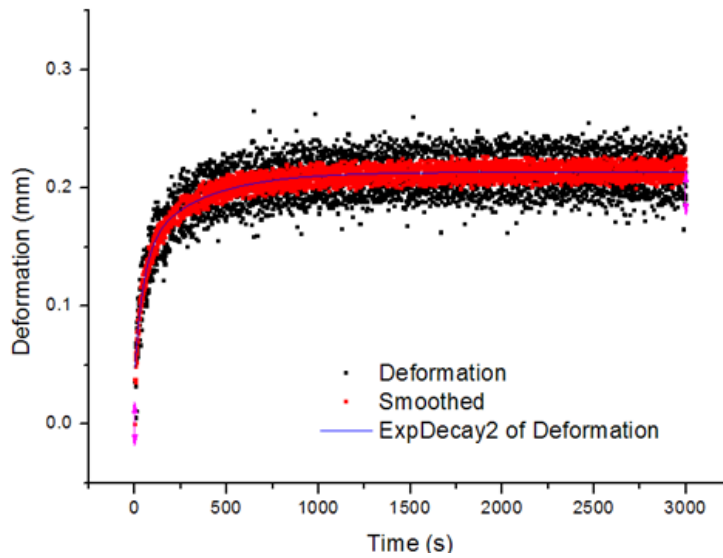
Figure 3.6. Experiment data curve-fit using Origin 8 software.

3.5.1 Compression Test Repeatability

The experiment repeatability test was carried out using five fresh cartilage pin specimens (*n=5*) with the purpose of investigating the repeatability of the compression test on the same specimen. Three tests were performed on each specimen, all with the same contact indentation point. Between each test, the specimens were permitted to equilibrate in PBS solution for one hour.

3.5.2 Compression Test of Subchondral Bone

Creep compression tests using an indenter on the subchondral bone were performed on six ovine fresh cartilage pin specimens (*n=6*) to observe any

deformation of the underlying bone. For this purpose, the cartilage was removed from the pin specimens using a surgical scalpel.

3.6 Cartilage Thickness Measurement

The cartilage thickness was evaluated using the compression test method and accordingly verified using the µCT imaging method. This section will describe both methods in detail.

3.6.1 Compression Test

The cartilage thickness was measured using a needle indenter, which was subjected to various compression forces with the objective to identify the most suitable for penetration of the cartilage but not the subchondral bone. The displacement and load readings were recorded at the frequency of 0.001s so as to establish more accurately the contact load. The thickness of the cartilage was obtained by determining the difference between the position of the needle when it contacted the cartilage surface and when it contacted the subchondral bone, as shown in the experiment graph in Figure 3.7. Penetration was terminated when a significant increase in the measured force was witnessed, thereby indicating that the needle was in contact with the subchondral bone.
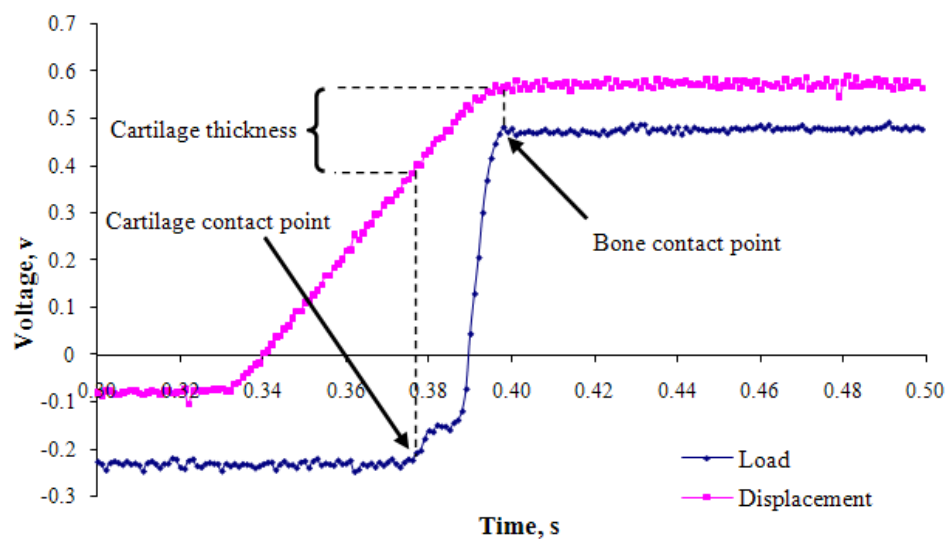
Figure 3.7. Compression test result to determine cartilage thickness.

3.6.2 Micro computed tomography

Only the middle slice image produced from the µCT scan was selected owing to the fact that the cartilage pin was indented at the centre in the compression test method. The cartilage thickness was evaluated using image measurement software (MATLAB V7.8.0 R2009a, MathWorks Inc., MA, USA) in order to contrast the scan image between the specimen and background. Two points were selected at the edges of the cartilage and the thickness was calculated based on the distance between these points. The measurements were carried out at the centre of the pin and four other points within a 0.2 mm interval in order to obtain the average thickness, as illustrated in Figure 3.8b.

a.   b.
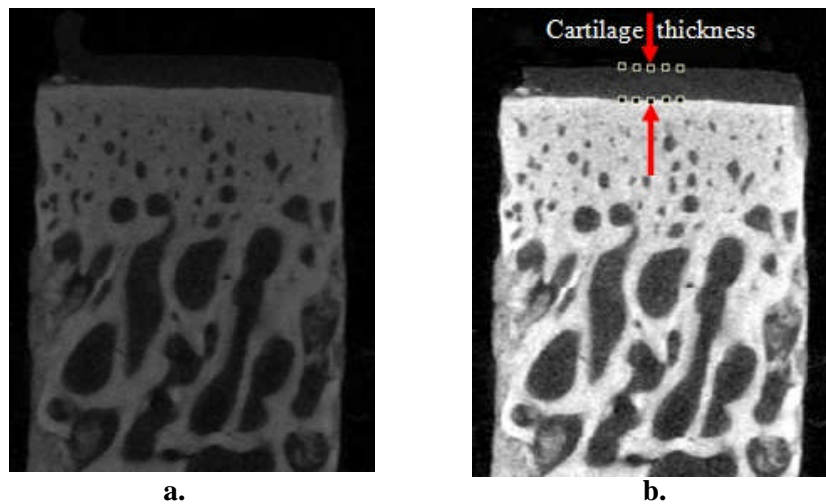
Figure 3.8. a. Image from µCT scan, b. Cartilage thickness measurement after image processing.

3.7 Computational Methods

Computational models were developed in order to simulate the creep-deformation phenomenon performed in the compression test experiment. All the finite element models were processed using Abaqus 6.9-1 (DS Simulia Corp., Providence, RI, USA). An idealised axisymmetric biphasic poroelastic model was used to characterise the cartilage biphasic properties of permeability (κ) and elastic modulus (E) for the cartilage pin specimens. Subsequently, a three-dimensional idealised model was constructed in order to develop the methodology which was then followed with the generation of a three-dimensional specimen-specific model.

The specimen-specific model was utilised in order to investigate the effects of the cartilage surface geometry and the underlying bone structure on the derived cartilage properties compared to the idealised model.

3.7.1 Idealised Axisymmetric Model

3.7.1.1 Implementation of Contact Dependent Flow

A contact dependent flow algorithm developed by Pawaskar (2006) was implemented to account for the change in the flow conditions between the free surface and the region where the indenter was in contact with the cartilage. It could also be applied in a three-dimensional model (Pawaskar, 2010). In this algorithm, the contact stresses at the cartilage surface nodes were recorded and evaluated. For the stress which was above the set threshold (0.0 MPa), indicating contact with the indenter, a sealed (no-flow) condition was applied at the node, otherwise a free flow condition was applied. The effectiveness of the algorithm can be observed in Figure 3.9 where the fluid flow in the contact nodes were completely stopped as impermeable indenter was used.
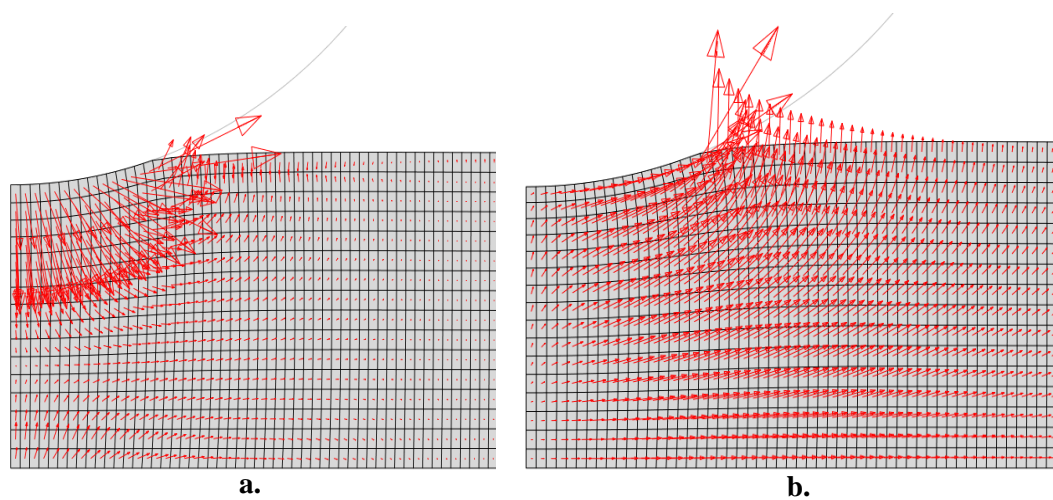
Figure 3.9. Direction of fluid velocity vector at a. 2 seconds, b. 1000 seconds.

3.7.1.2 Model Development: Repeat of Previous Study

As a first step, the model which was established by Pawaskar (2006) was reconstructed in order to validate the implementation of the contact-dependent flow detection algorithm. The compression test was simulated using an axisymmetric model with a 3 mm thickness and 20 mm radius of cartilage and a rigid spherical indenter of 5 mm radius, as shown in Figure 3.10. The cartilage consisted of 3200 (200×16) four-node bilinear displacement and pore pressure, reduced integration with hourglass control (CAX4RP) elements.
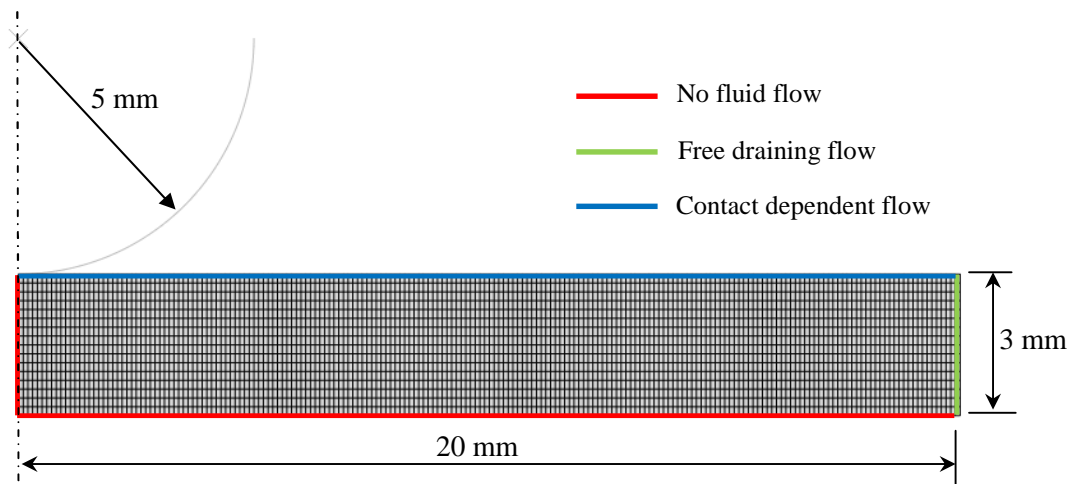
Figure 3.10. FE model for contact dependent flow implementation using an axisymmetric model with the axis of symmetry on the left (Pawaskar, 2006).

Boundary and interface conditions were applied on the cartilage and indenter, according to Pawaskar (Pawaskar, 2006, Pawaskar *et al.*, 2010). The bottom nodes of the cartilage were constrained in both horizontal and vertical directions, whilst the nodes on the axis were constrained in the horizontal direction. The spherical indenter was only permitted to move in a vertical direction, as the horizontal direction and rotational movements were constrained. For the cartilage fluid flow, as illustrated in Figure 3.10, the bottom and vertical symmetry axis of the cartilage surfaces were prevented from permitting fluid to flow whilst the outer edge nodes of the cartilage were maintained at zero pore pressure so as to allow unrestricted fluid flow as demonstrated in Figure 3.9. For the cartilage surface which was in contact with the indenter, the contact dependent flow algorithm was imposed. Table 3.2 shows the cartilage properties applied in the previous study.

Table 3.2: Cartilage material properties for FE validation model (Pawaskar, 2006).

Parameter	Value
Young's modulus, E	0.54 MPa
Poisson's ratio, v	0.08
Permeability, κ	4.0 x 10^{-15} m^4/Ns
Void ratio, e	4.0 (80% interstitial fluid)

For comparison purposes, both stress-relaxation and creep-deformation were simulated (Pawaskar, 2006). The stress-relaxation was simulated by applying 10% deformation over a ramp time of two seconds, and then the indenter position was maintained for a further 1,000 seconds. The creep-deformation simulation was then performed by applying a ramp load of 0.9 N on the indenter for two seconds with the load maintained for a further 1,000 seconds. In addition, the NLGEOM parameter was included so as to take account of the geometric nonlinearity which occurred within the model, as it affected the contact and pore pressure distributions at the cartilage surface after two seconds of ramp deformation.

3.7.1.3 Model Development: Simulation of Experimental Compression Tests

An axisymmetric biphasic poroelastic finite element model was generated to simulate the compression test experiment on the facet cartilage pin. The cartilage pin was modelled individually according to the measured cartilage thickness, whilst the bone was modelled at a constant 1.5 mm height. Four-node CAX4RP elements were selected to model the cartilage, because it has been shown that there were no marked differences of the contact pressure and pore pressure within the contact region as compared with an eight-node element (CAX8RP), whilst four-node bilinear elastic elements (CAX4) were used to represent the underlying bone (Pawaskar *et al.*, 2010). The 1 mm radius rigid spherical indenter was modelled as an analytical rigid body. A diagram of the finite element mesh for the cartilage and subchondral bone is shown in Figure 3.11.
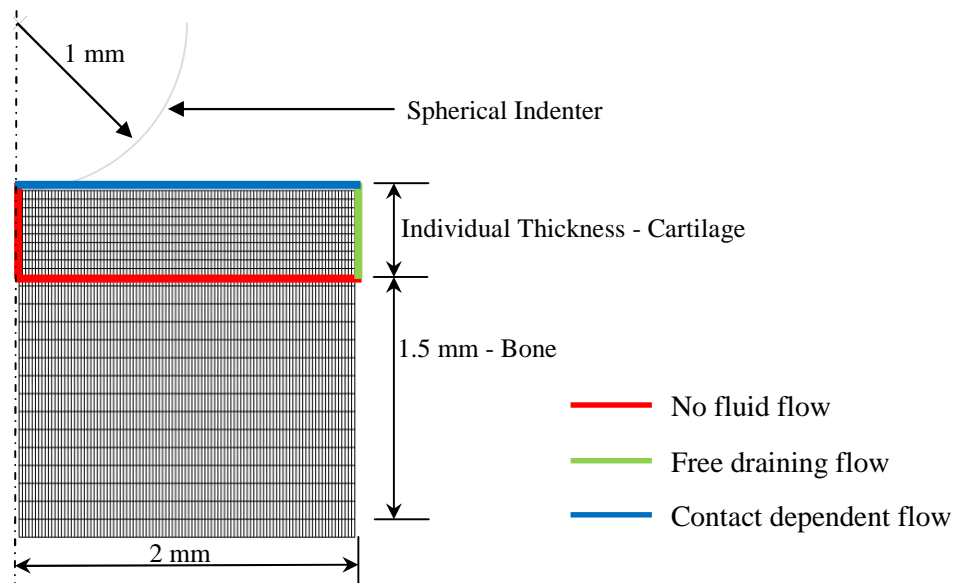
Figure 3.11. Axisymmetric FE model of cartilage pin.

Boundary and interface conditions were applied on the cartilage and indenter, to imitate the experimental creep compression test set-up. The bottom nodes of the bone were constrained in both horizontal and vertical directions, whilst the nodes on the axis were constrained in the horizontal direction. The spherical indenter was only permitted to move in the vertical direction, as the horizontal direction and rotational movements were constrained. For the cartilage fluid flow, as illustrated in Figure 3.11, flow was prevented at the bottom and vertical symmetry axis of the cartilage surfaces whilst the outer edge nodes of the cartilage were maintained at zero pore pressure so as to allow unrestricted fluid flow. For the upper cartilage surface, the contact dependent flow algorithm was imposed where the flow conditions at the nodes were changed depending on the contact stress.

In order to simulate the creep-deformation phenomenon, a ramp load from 0 to 0.24 N, matching the experiment, was applied on the indenter for two seconds, and the load was then maintained at 0.24 N for a further 3,000 seconds. The two seconds ramp period was based on an experimental study, which found that the minimum time at which creep compression test of the cartilage could be compared reliably was two seconds after the application of the load (Kempson *et al.*, 1971). The two-second ramp load was also used in previous computational studies (Warner *et al.*, 2001, Pawaskar *et al.*, 2010). Although the automatic time increments were applied in the model, the increments were controlled using the UTOL parameter,

which specified the allowed maximum pore pressure change in one increment at a typically small value of 600 kPa so as to produce acceptable results (Goldsmith *et al.*, 1995, Warner *et al.*, 2001, Pawaskar, 2006).

3.7.1.4 Mesh Sensitivity Analysis

Mesh sensitivity analysis was carried out in order to obtain an optimised model for the cartilage. The FE model, as described in Section 3.7.1.3, was implemented using the cartilage properties shown in Table 3.2 to simulate the creep-deformation phenomenon. The elastic modulus and Poisson's ratio of the underlying bone were taken as 2 GPa and 0.20 respectively (Pawaskar *et al.*, 2010).

The mesh density of the cartilage was uniformly generated, which consisted of 160 (40×4 in the horizontal and vertical directions respectively), 360 (60×6), 640 (80×8) and 1440 (120×12) elements. In addition, a concentrated mesh density at the contact area consisting of 300 elements, as shown in Figure 3.12b, was also generated for comparison.

a. **b.**
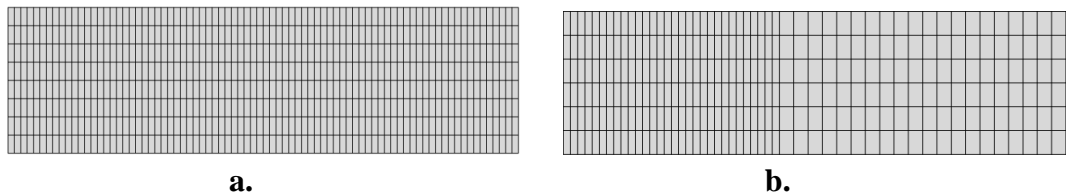
Figure 3.12. Examples of finite element mesh for mesh sensitivity analysis. a. Uniform mesh 640 elements (80×8), b. Concentrated mesh at contact area 300 elements.

3.7.2 Idealised Three-Dimensional Model

An idealised three-dimensional (3D) model was developed to provide a framework for the generation of specimen-specific models. The geometry, boundary and interface conditions from the axisymmetric model, as described in Section 3.7.1.3, were implemented for the purpose of validation. However, an additional step was introduced in order to initiate the contact between the indenter and cartilage surfaces. The cartilage was represented using eight-node trilinear displacement and pore pressure, reduced integration elements (C3D8RP) and for the bone, eight-node linear brick elements (C3D8) were applied (Pawaskar *et al.*, 2010). The concentrated

mesh density around the contact area, as in the axisymmetric model as shown in Figure 3.13, was implemented using the material properties derived from the axisymmetric model.
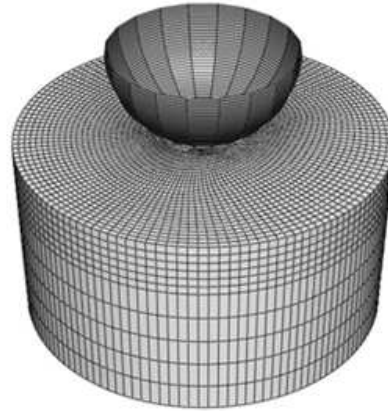
Figure 3.13. Idealised three-dimensional FE model.

The results obtained from this model were compared with the axisymmetric model for verification. The results between the axisymmetric and three-dimensional models were found to be very similar in terms of the cartilage displacement and contact pressure shown in Figure 3.14. Therefore, this protocol was deemed applicable to be implemented in the specimen-specific model development.
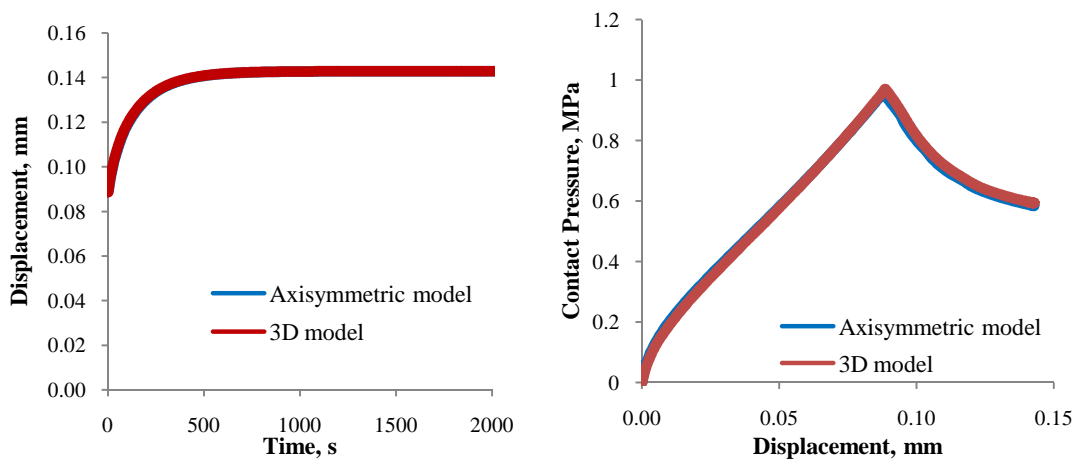
Figure 3.14. Comparisons of the results produced from the idealised axisymmetric and 3D models

3.7.3 Specimen-Specific Model

3.7.3.1 Model development

The specimen-specific model was developed using the 3D geometrical data of the cartilage pin obtained from the µCT scan. The data, with a resolution of 20 µm, was converted into a series of .tiff format images, which were subsequently segmented using ScanIP v3.2 (Simpleware Ltd, Exeter, UK) software. In the segmentation process, the images were first filtered to reduce the noise effects on the image. Two masks were then created to define the shapes of the cartilage and underlying bone. The masks were generated using global threshold operation which was applied to all the images where the cartilage and the bone were differentiated based on the specified range of the image voxel. A flood-fill operation was used to separate the main object from the mask generated from surrounding noise and more importantly to ensure the connectivity of the main object. Subsequently, the 3D solid model was generated from the final masks as shown in Figure 3.15b.

a.   **b.**   **c.**
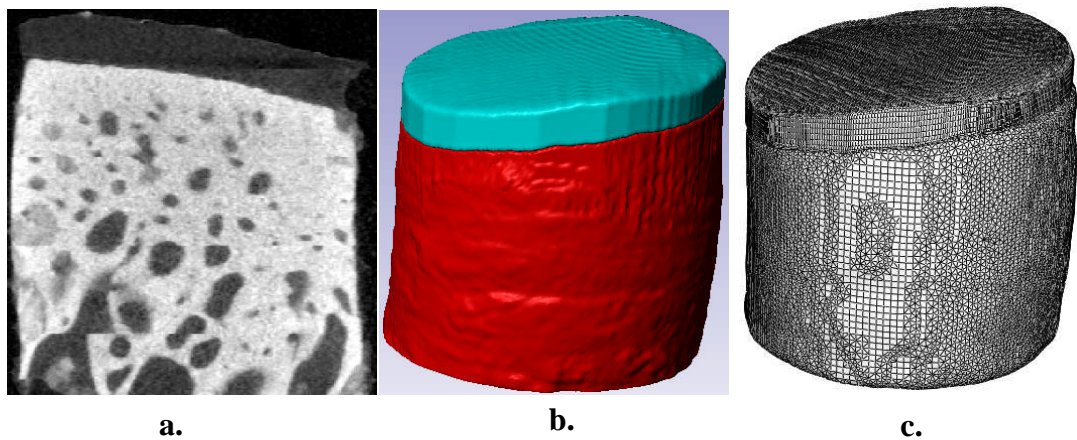
Figure 3.15. Development of three-dimensional specimen-specific FE model. a. µCT scan image, b. 3D solid model, c. FE model.

The solid model was then meshed into finite elements, where the cartilage was meshed using IA-FEMesh 1.0 software (University of Iowa, IA, USA) to generate hexahedral mesh whilst the bone was meshed using ScanFE v3.1.4 (Simpleware Ltd, Exeter, UK) software to generate a mixed mesh of hexahedral and tetrahedral elements as shown in Figure 3.15c. Eight-node trilinear displacement and pore pressure, reduced integration elements (C3D8RP) were used in the cartilage mesh whereas both eight-node linear brick elements (C3D8) and four-node linear

tetrahedral elements (C3D4) were used in the bone mesh. The bottom surface of the cartilage was tied to the top surface of the bone to prevent any relative movement between the two during the simulation.

However, owing to the curvature at the edge of the cartilage, the hexahedral mesh generated was not smooth, and produced distorted elements. This subsequently affected the convergence of the solution. Therefore, a cuboid specimen-specific model representing the central region of the specimen was developed in order to eliminate the effect at the cartilage curvature, as described in the next section.

3.7.3.2 Cuboid Specimen-Specific Model

Similar segmentation and meshing protocols used to generate the specimen-specific model described in Section 3.7.3.1 was implemented in the development of cuboid specimen-specific model. In addition, a square region of interest (Figure 3.16a) for both the cartilage and underlying bone was created throughout the images using unpaint operation tool in ScanIP v3.2 (Simpleware Ltd, Exeter, UK) software. This was then followed by generating the 3D solid model and meshing the model as described in Section 3.7.3.1 and shown in Figure 3.16b.

a.   **b.**
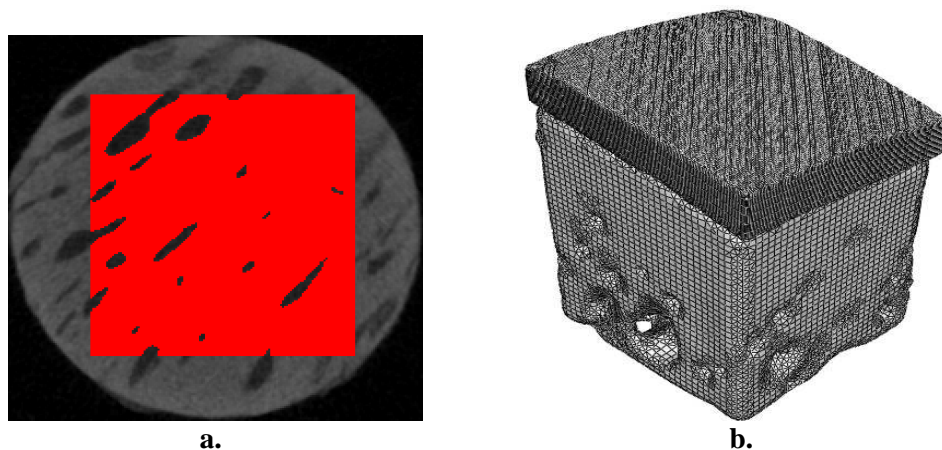
Figure 3.16. a. Image segmentation into square shape, b. Cuboid specimen-specific FE model.

3.7.3.3 Cartilage Width Sensitivity Analysis

A cartilage width sensitivity analysis was performed to investigate the consequences of reducing the dimensions of the cuboid model. Since the

computational time to run the cuboid model was high, the sensitivity study was performed using an axisymmetric model to simulate the creep-deformation phenomenon, and the cartilage width from the symmetry axis to the edge was varied from 2 mm to 1 mm. The minimum cartilage width of 1 mm was determined by the lowest distance from the contact centre point to the edge in the cuboid specimen-specific model, which was 1.06 mm, as shown in Figure 3.17. The results from the axisymmetric model for 1 mm cartilage width were then compared with the cuboid three-dimensional idealised model using the same dimensions, which was developed to observe the effect in three-dimensional model.
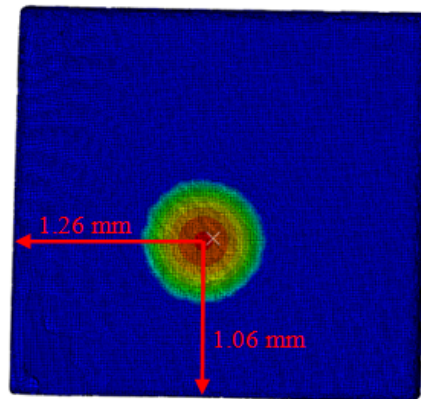
Figure 3.17. The distance from the contact point to the edge.

Comparison of the cartilage deformation curve was performed because this data would be utilised in order to estimate the equilibrium biphasic properties. Figure 3.18 shows the cartilage deformation curve at the maximum contact pressure node for the different diameter axisymmetric models and the three-dimensional model. The axisymmetric models were found to be very similar and insignificant effect was observed to the three-dimensional model which possess 1 mm cartilage width to the centre point. Based on this finding, it was concluded that the specimen-specific cuboid model, with half-edge dimensions of 1 mm, could be applied to generate the cartilage deformation curve for the cartilage biphasic properties characterisation.
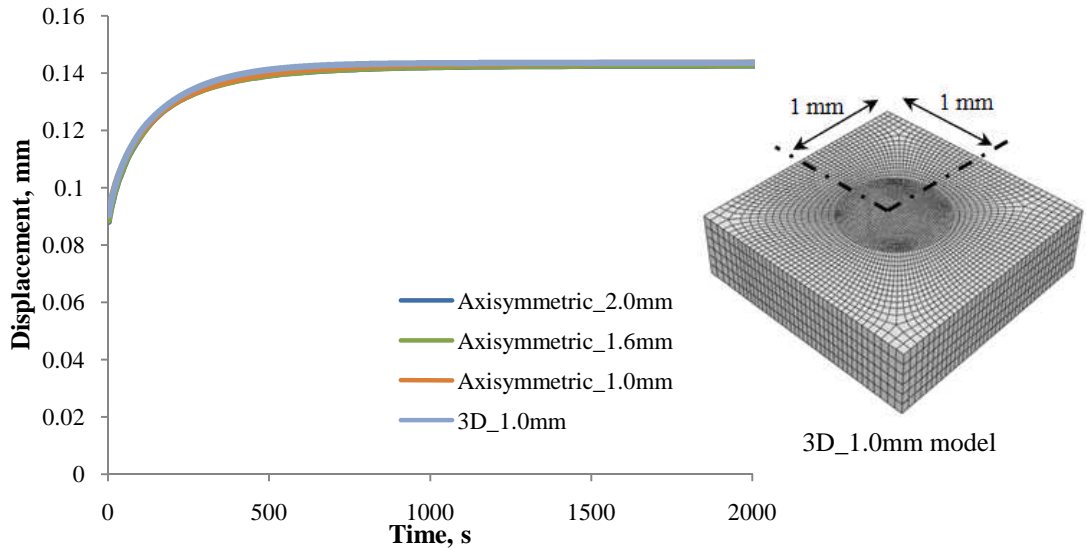
Figure 3.18. Cartilage deformation results for the cartilage model width sensitivity analysis.

3.8 Cartilage Biomechanical Properties Characterisation

The cartilage equilibrium biphasic properties of elastic modulus and permeability were characterised by combining both experimental and computational methods. The axisymmetric biphasic poroelastic FE model described in section 3.7.1.3 was implemented to simulate the experimental creep compression test performed on the cartilage pin. The Poisson's ratio of the cartilage was assumed and maintained at 0.0 to allow maximum compressibility (Jin *et al.*, 2000), and the cartilage water content of 74.7% was imposed (Elder *et al.*, 2009). For the subchondral bone, the elastic modulus and Poisson's ratio were taken as 1510 MPa (Mitton *et al.*, 1997) and 0.3 (Shirazi and Shirazi-Adl, 2009) respectively.

The cartilage biphasic elastic modulus (*E*) and permeability (*κ*) were estimated by matching the cartilage deformation curve generated from the FE model to the experimental deformation curve using a least-squares method to resolve the function [3] (Lei and Szeri, 2007, Pawaskar, 2010),

$$f(\kappa_0, E_0) = \sum_{i=1}^{N} [U_{t_i}(\kappa_0, E_0) - U_{e,t_i}]^2$$

....................[3]

where N is the total number of observations, $U_{t_i}(\kappa_0, E_0)$ and U_{e,t_i} are predicted from FE model and experimental displacements, respectively, at time t_i of the ith observation. During the analysis, the inequality constraints of the parameters were specified as, $0 < \kappa_0 < \infty$ and $0 < E_0 < \infty$.

In order to optimise the nonlinear least-squares problem, a programme developed by Pawaskar (2010) was applied which imposing 'lsqnonlin' function in MATLAB software. Initial values of equilibrium elastic modulus and permeability of the cartilage were used to begin the iteration and the final optimised values were obtained when the function reached the minimum specified convergence criteria or minimal squared error occurred between the curves.

3.8.1 The Effects of Cartilage Poisson's Ratio and Void Ratio

In previous studies from other synovial joints, the cartilage biphasic Poisson's ratio was characterised to be between 0.02 to 0.098 using compression testing as shown in Table 1.5. However in this study, the Poisson's ratio was initially assumed to be 0.0 in the characterisation process to achieve the maximum cartilage compressibility (Jin *et al.*, 2000). To study the sensitivity to this parameter, the Poisson's ratio was varied from 0.0 to 0.2 in the axisymmetric FE model and the effects on the cartilage deformation curve, which was utilised to derive the properties, was observed.

Furthermore, the effect of the cartilage void ratio on the cartilage deformation curve was also investigated using the axisymmetric FE model. The void ratio was varied between 3.0 and 4.25 representing the fluid phase of the cartilage water composition of 60-85% (Mow and Huiskes, 2005).

3.8.2 The Effects of Subchondral Bone Elastic Modulus

In this study, the effect of the subchondral bone elastic modulus was investigated on the cartilage deformation curve. An initial elastic modulus of 1510 MPa was applied which assumed to be a normal healthy bone for the ovine specimens. The elastic modulus was varied down to a value of 20 MPa, representing the lowest value likely in severely osteoporotic bone. This was again undertaken in

the axisymmetric FE model and the effects on the predicted cartilage deformation examined.

3.8.3 The Effects of Indenter Radius

The cartilage properties characterisation was also performed using a larger indenter size of 6.3 mm diameter, which was also as undertaken in the experimental testing. This would enable the effect of using larger indenter size on the estimated cartilage biphasic properties to be evaluated. For this study, the axisymmetric FE model described in Section 3.7.1.3 was adapted to represent the 6.3 mm diameter indenter.

3.8.4 The Effects of Cartilage Surface Curvature

Although some curvature was observed in the cartilage pin specimens, the cartilage surface was assumed to be flat in the axisymmetric FE models used for the characterisation of the cartilage properties. In this study, the effects of the cartilage surface curvature on the characterised cartilage properties were examined using the axisymmetric model. Although the curvature generated from the axisymmetric model was different compared to the actual cartilage curvature (Figure 3.19a), this step was undertaken to evaluate if the outputs were sensitive to curvature in general.

The cartilage pin that had the most curvature, shown in Figure 3.19a, was selected and the measurement of the cartilage surface radius was carried out using the method described in Section 2.4.2 and shown in Figure 3.19b. The radius was determined to be 19.3 mm. To assess the possible effect of this curvature, the axisymmetric model was adapted to include a curved surface. Two cartilage surface radii of 20 mm and 40 mm were employed, including both concave and convex shapes of the curve. Figure 3.19c shows an example of axisymmetric FE model of the 20 mm radius cartilage curvature with convex curve.
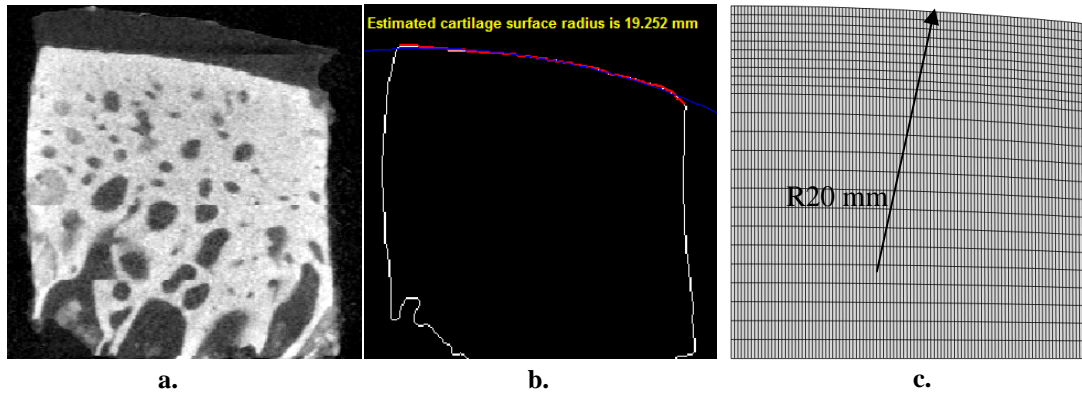
Figure 3.19. a. µCT scan image of the most curvature cartilage pin, b. Measurement of the cartilage surface radius, c. Axisymmetric FE model of 20 mm radius with convex curve.

Further investigation was carried out using the specimen-specific model to examine the cartilage deformation of the actual three-dimensional curvature. In addition, a gradient three-dimensional model shown in Figure 3.20 was generated which had an approximately 10º gradient angle at one plane measured from the actual image in Figure 3.19. This enabled the three types of the cartilage surface, which were flat, gradient and specimen-specific curvature, to be explored.
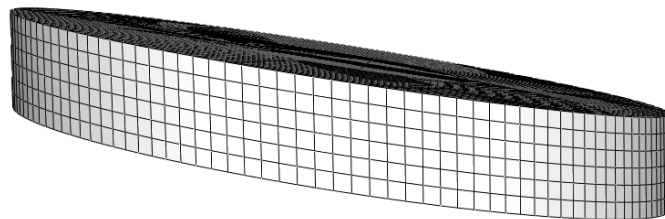
Figure 3.20. Idealised gradient three-dimensional FE model.

3.9 Statistical Analysis

For the quantitative experimental data, mean and standard deviations were calculated and displayed as mean ± standard deviation (SD) unless stated otherwise. The following statistical methods were used in this study.

Student t-test

The Student t-test was also used to determine statistical differences ($p<0.05$) for the derived biphasic properties of elastic modulus and permeability between the 2 mm diameter and 6.3 mm diameter indenters. All the tests were performed using Microsoft Excel 2007.

One-Way Analysis of Variance (ANOVA)

One-way ANOVA ($p<0.05$) was carried out to examine statistical differences for the derived biphasic properties of elastic modulus and permeability within the fresh cartilage pin, frozen joint cartilage pin and frozen pin samples. The analysis was performed using SPSS PASW Statistics 17.0 (IBM Corporation, NY, USA) software.

3.10 Summary

This chapter outlined all of the experimental and computational methodologies used to characterise the biomechanical properties of the facet cartilage. The compression test experiment method using an indenter was performed to provide experimental data to characterise the biphasic properties of the cartilage. The cartilage deformation curve generated from the biphasic poroelastic axisymmetric FE model was matched to the experimental deformation curve in order to estimate the cartilage properties of the elastic modulus and permeability. Furthermore, a novel specimen-specific model was developed to study the three-dimensional geometrical effect of the cartilage surface on the estimated biphasic properties of the cartilage.

Chapter 4: Results – Morphological Study of the Facet Joint

4.1 Introduction

This chapter presents the results and analysis of the facet joint morphological study. The first section presents the outcome of the ovine and human facet joints morphology and comparisons between the two species. This is followed with the investigation of the correlation between the measurement parameters and finally discussed the overall results in the final section.

4.2 Facet Joint Articular Radius

The superior and inferior facet articular radius values for the three ovine spines ($n=3$) are presented in Figure 4.1 and Figure 4.2. The left and right radii were averaged together to obtain the mean and standard deviation because difference between the two was found not to be statistically significant using a t-test analysis ($p<0.05$). From the measurements, most of the thoracic vertebral segments were found to be flat with the exception of T2T3 and T12T13, both of which are at the transitions between the spine regions. The facet joint scan images of Spine 2 are shown in Appendix I at all levels of the vertebral segment.
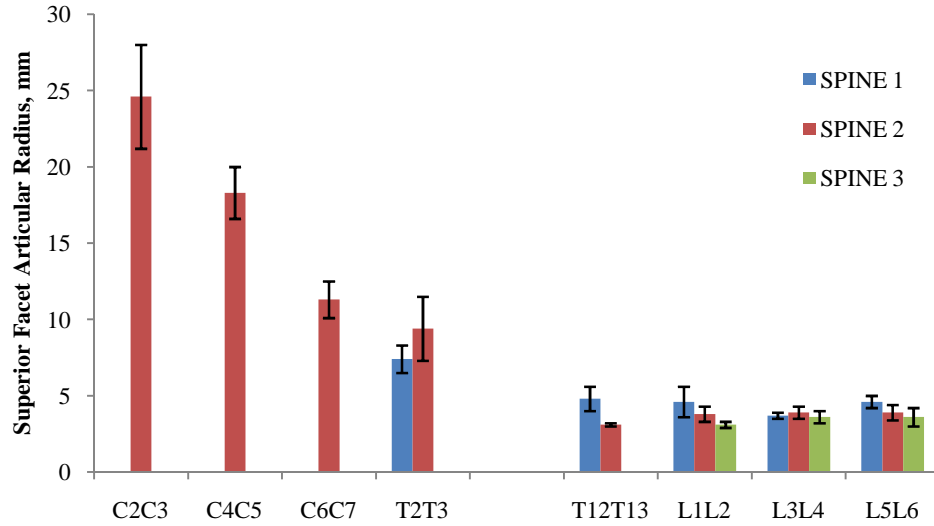
Figure 4.1. Superior facet articular radius of ovine vertebral segment. The bars represent the mean (± SD) of at least six measurements taken on the left and right facet joint at each level.
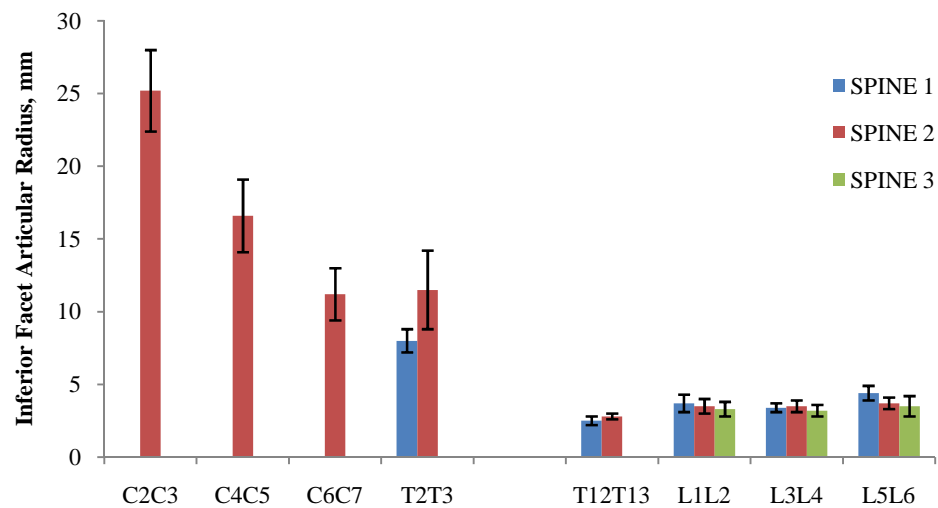
Figure 4.2. Inferior facet articular radius of ovine vertebral segment. The bars represent the mean (± SD) of at least six measurements taken on the left and right facet joint at each level.

In the cranial direction, the facet radius increased gradually from T2T3 to C2C3, reaching a maximum value of 25.2 mm. However, only one spine was found with curved facet joints at the cervical region, whilst the other two spines were flat. This curved facet joint possessed higher variation of the radius measurements, which denotes the irregular curvature throughout the cervical facet joints. Figure 4.3 shows an example of the flat and the curved facet joint at cervical region. Towards the

caudal direction, a relatively consistent facet radius was seen in the joints between T12T13 and L5L6, ranging between 3.1 mm and 4.8 mm for the superior radius while the inferior radius ranged between 2.5 mm and 4.4 mm.
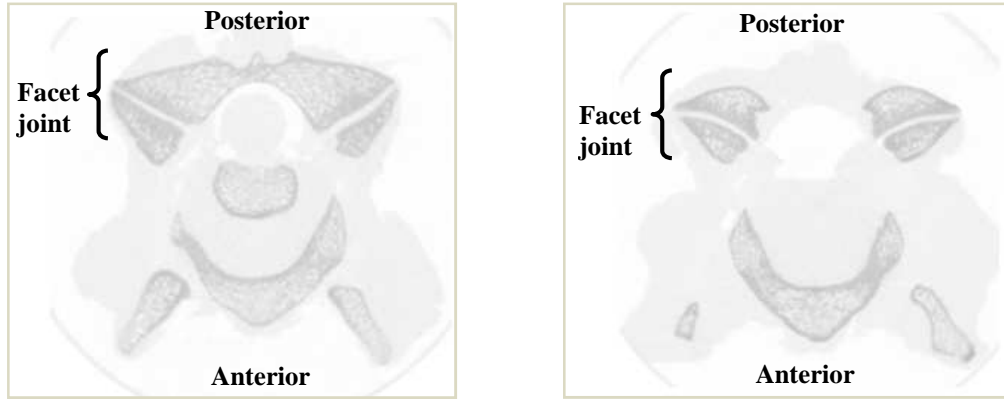
Figure 4.3. μCT scan image of C4C5 vertebral segment a. Flat facet joint of Spine 3, b. Curved facet joint of Spine 2.

For the human facet joint, the superior facet radius from the L1 to L4 vertebra level ranged from 6.3 mm to 8.8 mm, as shown in Figure 4.4. Although the radius at L4 measured in the present study was considerably lower than the average radius at that level measured by van Schaik and van Pinxteren (1999) at 13.7 mm, it was still within the range of the extensive measurement variation (±5.8 mm) published in the study.
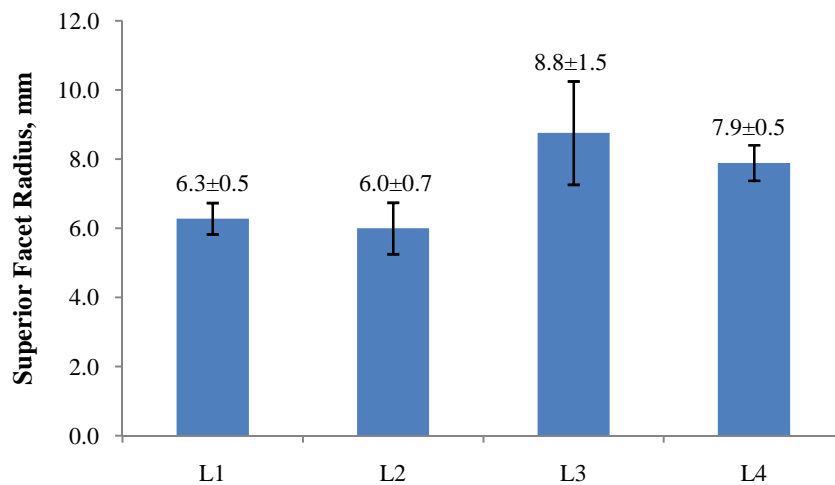
Figure 4.4. Superior facet articular radius of human vertebrae. The bars represent the mean (± SD) of at least eight measurements taken on the left and right facet joint at each level.

4.3 Comparison of Facet Articular Radius between Ovine and Human L4 Vertebra

Limited data on facet articular radius in the previous literature meant that the comparison was only undertaken at the L4 vertebra level. The human vertebral dimensions in the present study were taken from one vertebra (*n=1*) because it was the only data available. The measurement of the facet articular radius (R), the width (W) and depth (D) of the vertebral body are illustrated in Figure 4.5.
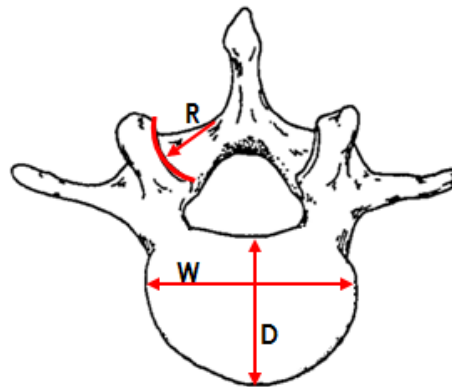
Figure 4.5. Schematic diagram of vertebral dimension measurement.

Comparisons of the ovine and human L4 vertebra dimensions are tabulated in Table 4.1. In order to verify the measurement method, the dimensions were compared to the previous studies. As can be seen, the dimensions were comparable and within the range of the previous measurement, although a considerable difference was found for the average human facet radius. However, the difference of the facet radius was mainly attributed to the method applied in the previous study, where only three points were used in order to determine the radius, which would be likely to result more error in the measured facet radius.

Table 4.1. Vertebral dimensions (mean ± SD) of ovine and human L4 vertebra.

Dimension (mm)	Ovine		Human		Ovine/Human Present Study (min–max)
	Present Study	Previous Study	Present Study	Previous Study	
W	27.3±1.2	27.6 (Sheng, 2010)	48.0	51.2±5.6 (Berry 1987)	0.56 (0.54-0.59)
D	19.2±1.0	20.7 (Sheng 2010)	33.4	34.9±3.4 (Berry 1987)	0.57 (0.54-0.60)
R	3.7±0.3	4.0 (McLain 2002)	7.9±0.5	13.7±5.8 (van Schaik 1999)	0.47 (0.40-0.54)

All of the dimensions were larger for the human specimens than for the ovine specimens. The dimensional ratios between the ovine and human were examined in order to observe the relationship between the two species. From the table, the ratios of the dimensions were found to be within the same range, although a marginal difference was found for the facet radius. Despite the limitation of measuring only one human L4 vertebra, the dimensions were comparable with the previous studies. The outcome of this comparison is a useful factor in justifying the suitability of the ovine lumbar vertebra to represent the human lumbar facet joint in range of motion studies.

4.4 Facet Joint Orientation Angle

The transverse facet joint orientation angles, as described in Section 2.4.3, of three ovine spine ($n=3$) are presented in Figure 4.6. The left and right angle measurements were averaged together to obtain the mean and standard deviation because the difference between the two was found to not be statistically significant using a t-test analysis ($p<0.05$). Based on the results, the angles could be grouped into three main categories, which were approximately associated with the three spinal regions.
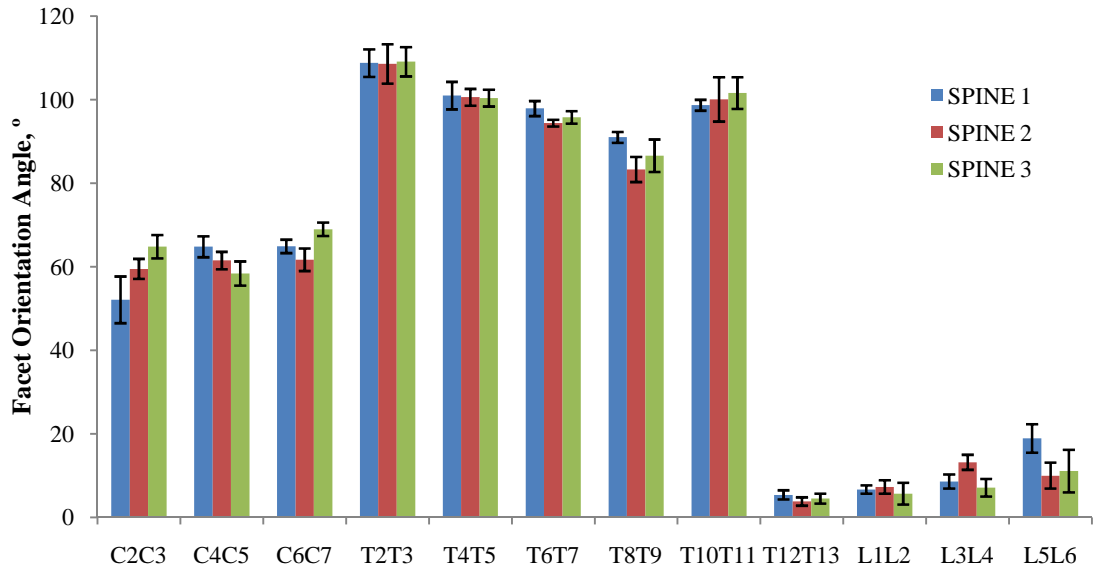
Figure 4.6. Transverse facet joint orientation angle of ovine vertebral segment. The bars represent the mean (± SD) of at least six measurements taken on the left and right facet joint at each level.

The first group includes the angles from the cervical region C2C3 to C6C7 where the angles slightly increased from 52.1º to 69.0º. In the second group which was in the thoracic region from T2T3 to T10T11, the angles ranged between 83.3º and 109.1º without any clear trend. Furthermore, the facet angles were facing the anterior side of the vertebra, or were more than 90º, as shown in Figure 4.7b. Finally, in the most caudal group, from the last thoracic T12T13 to the last lumbar L5L6 vertebral segments, the angle increased considerably from 3.8º to 18.9º. Furthermore, the facet angles were the most narrow as shown in Figure 4.7c.
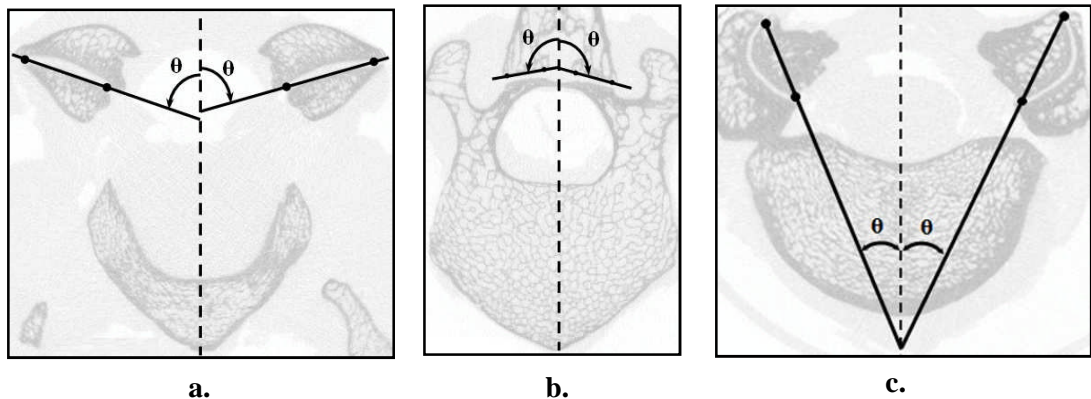
Figure 4.7. Facet joint orientation angle classification a. Group 1: C2C3-C6C7, b. Group 2: T2T3-T10T11, c. Group 3: T12T13-L5L6.

The facet joint angles of the human lumbar spines were found to vary between 13.8º and 31.0º. In order to verify the facet angle measurement method, the transverse facet angles of human vertebrae were compared with a previous study. Although the present results were found to be lower than the study carried out by Masharawi *et al.* (2004), the values were nevertheless within the measurement range, as illustrated in Figure 4.8. Moreover, the trend of the results was similar where the angles decreased from the L1 to L2 vertebra level, and then increased to the L4 level.
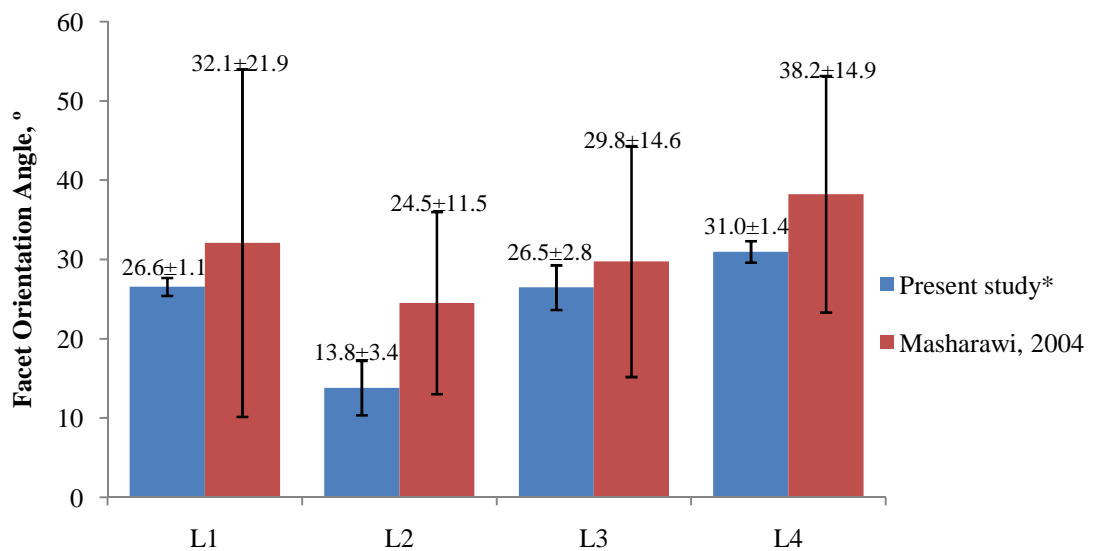
Figure 4.8. Comparison of the transverse facet joint orientation angle of human vertebra between the present study and Masharawi *et al.* (2004).

* Note: The bars represent the mean (± SD) of at least eight measurements taken on the left and right facet joint at each level.

4.5 Comparison of Facet Joint Orientation Angle between Ovine and Human Spine

The ovine facet angles were compared with the human facet angles reported by Masharawi *et al.* (2004). Since very limited data on the human cervical facet angles were published in the previous literature, comparisons were only performed at the thoracic and lumbar regions. As illustrated in Figure 4.9, both of the spines have similar angle trends in each of the spine regions. However, it is noteworthy to

highlight that a considerable difference was established at ovine T12T13 and human T12L1 levels, which could be due to the transition point between the regions, as these two species have a different number of vertebrae in each region.
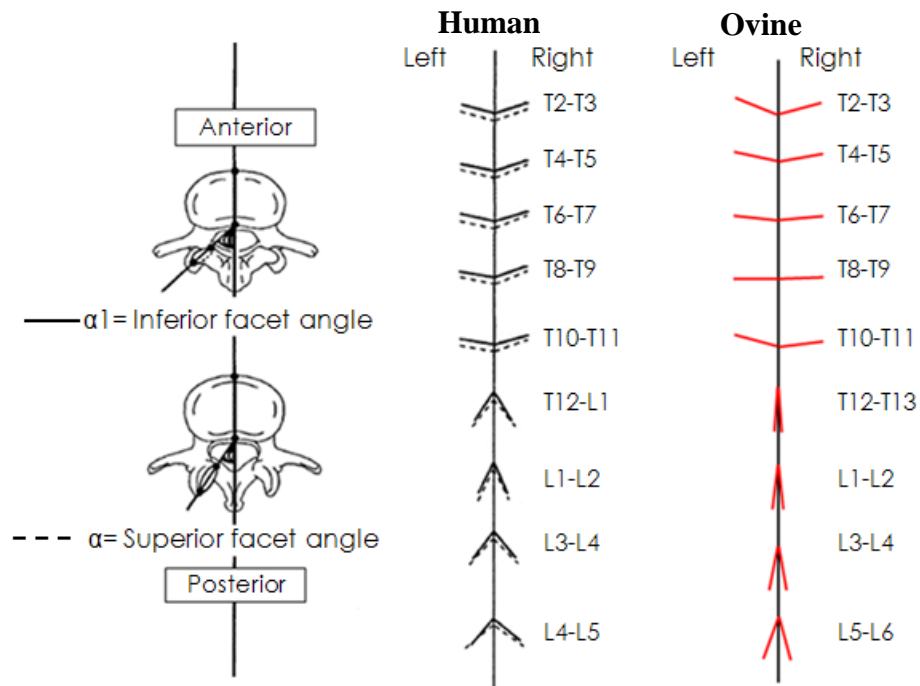
Figure 4.9. Comparison of the facet orientation angle in transverse plane along vertebral column between the present results of the ovine spine and the human spine study by Masharawi *et al.* (2004).

4.6 Relationship between Facet Orientation Angle and Facet Articular Radius

Although the relationships between facet orientation and radius have been studied previously, it is not possible to compare the results directly with the present study, because different methods and criteria were applied. For instance, van Schaik and van Pinxteren (1999) observed the relationship between the facet radius and the facet orientation circle instead of facet orientation angle, in which the methods have been described earlier in Section 1.4.2.2. However, no conclusive relationship could be found between those parameters. Therefore, in the present study, the relationship between the facet radius and orientation angle were examined to determine if there was a correlation. The relationships were evaluated based on the linear regression analysis for ovine and human vertebrae.

4.6.1 Ovine Vertebral Segments

The ovine vertebral segments were examined from T12T13 to L5L6 because the facet radius at the thoracic region was flat, and only one from three spines was found to curve at the facet articular surfaces in the cervical region. The correlation between facet angle and the facet radius was weak and was found to be insignificant ($p>0.05$), as shown Figure 4.10.

R² = 0.1932
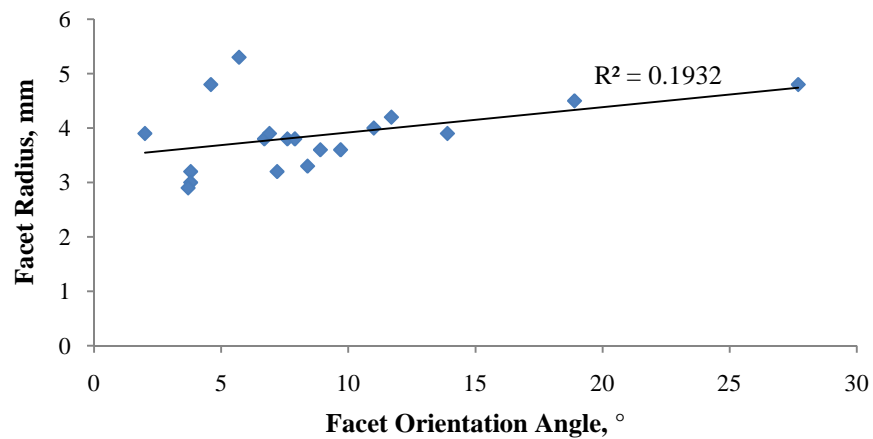
Figure 4.10. Correlation between facet orientation angle and facet articular radius of ovine vertebral segments.

4.6.2 Human Vertebrae

The relationship between the facet angle and the facet radius for the human vertebrae was examined from L1 to L4 vertebral level due to the limited scan data. Similarly to the ovine, no correlation ($p>0.05$) was found between the facet angle and facet radius as shown in Figure 4.11.
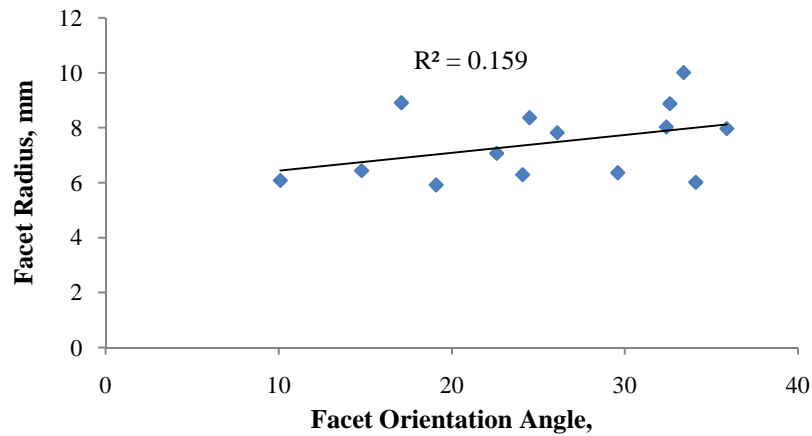
Figure 4.11. Correlation between facet orientation angle and facet articular radius of human vertebrae.

Therefore, these results confirm that geometrically there is no relationship between the facet orientation angle and facet radius for both ovine and human vertebrae.

4.7 Relationship between Facet Orientation Angle and Axial Rotation

It has been reported that the asymmetry of the facet joint angle, known as facet tropism, has no correlation with intervertebral disc degeneration and facet joint osteoarthritis (Vanharanta *et al.*, 1993, Boden *et al.*, 1996, Kalichman *et al.*, 2009). However, the facet joint angle alone has certainly been associated with those diseases (Farfan *et al.*, 1972, Boden *et al.*, 1996, Fujiwara *et al.*, 2001, Kalichman *et al.*, 2009). Ahmed *et al.* (1990) found a lack of correlation between the facet angle and axial rotation, despite the fact that mechanically it would be expected that the two would be related. Therefore, this relationship was again investigated with the use of ovine vertebral segments and human vertebrae based on the linear regression analysis.

4.7.1 Ovine Vertebral Segments

The mean of the facet orientation angles of the ovine vertebral segments for three spines (*n=3*) were plotted together with the mean range of motion in axial

rotation studied by Wilke *et al.* (1997a) against the vertebral level. The angle and axial rotation were seen to possess similar trends, which can be divided into three groups approximating to the spine regions, as demonstrated in Figure 4.12.
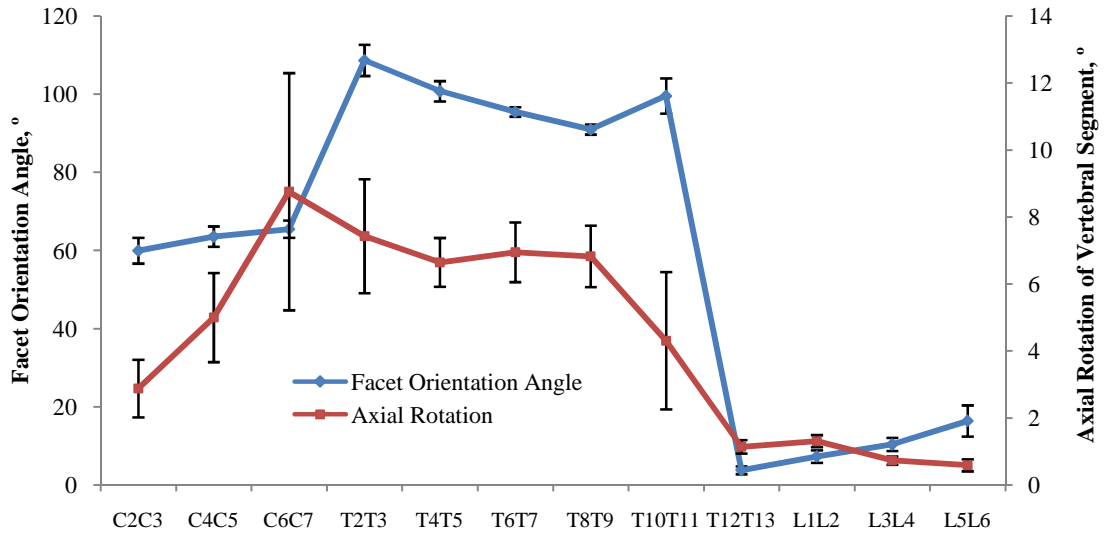
Figure 4.12. Relationship between mean (± SD) of the facet orientation angle from the current study and axial rotation (Wilke *et al.*, 1997a) of ovine vertebral segments.

The mean of the facet angle were then plotted against the mean of the axial rotation to determine if there was a relationship between these two parameters. A significant correlation ($p<0.05$) was found between the facet angle and axial rotation where the axial rotation of the vertebral segment increased with increasing facet orientation angle as shown in Figure 4.13.
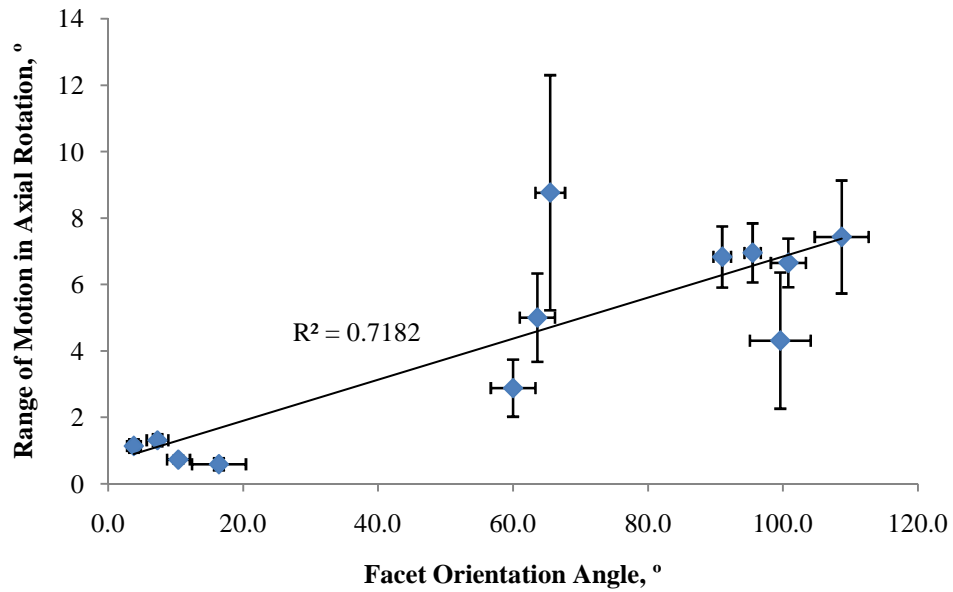
Figure 4.13. Correlation between the mean (± SD) of the facet orientation angle and axial rotation (Wilke *et al.*, 1997a) of ovine vertebral segments.

4.7.2 Human Vertebrae

For the human vertebrae, the relationships were evaluated at the L1L2, L2L3 and L3L4 vertebral segments. Figure 4.14 shows the graph of the facet orientation angle against the range of motion in axial rotation data for the human vertebral segments were obtained from the previous studies (Yamamoto *et al.*, 1989, Panjabi *et al.*, 1994). Statistically, the facet angle was significantly correlated ($p<0.05$) to the axial rotation measured by Yamamoto *et al.* (1989). Conversely, insignificant correlation ($p>0.05$) was obtained with the axial rotation measured by Panjabi *et al.* (1994).
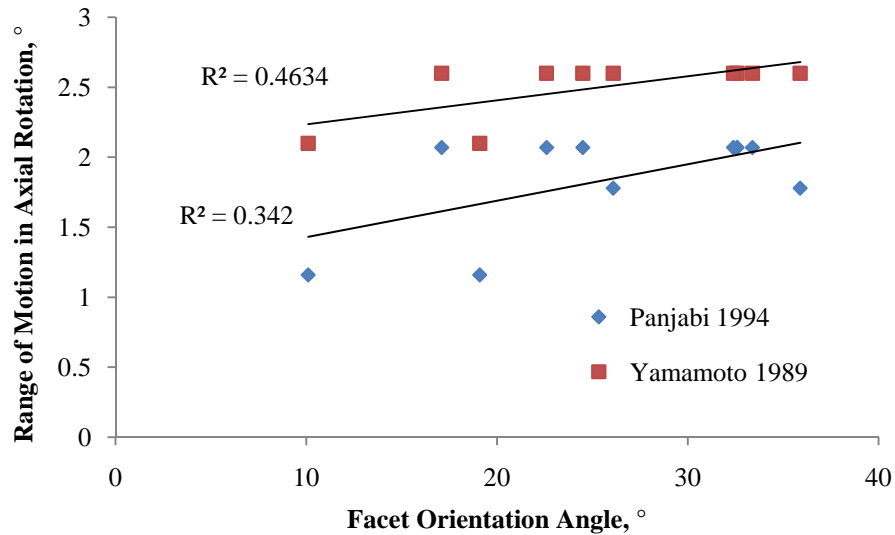
Figure 4.14. Correlation between facet orientation angle and axial rotation (Yamamoto *et al.*, 1989, Panjabi *et al.*, 1994) of human vertebral segments.

However, these conflicting results were mainly caused by the experiment methodology of the axial rotation measurement. Panjabi *et al.* (1994) applied a compressive preload of 100 N along the longitudinal axis of the specimen throughout the experiment whereas no preload was applied in Yamamoto *et al.* (1989) experiment. There are other factors that could contribute to the variation of the axial rotation measurement such as the experimental set-up, amount of preload and axial torque applied, and whether a two-vertebra segment (Ahmed *et al.*, 1990, Wilke *et al.*, 1997a) or the whole intact lumbar spine (Yamamoto *et al.*, 1989, Panjabi *et al.*, 1994) was used. The variation of the axial rotation measurement has been presented in Panjabi *et al.* (1994) work illustrated in Figure 4.15.
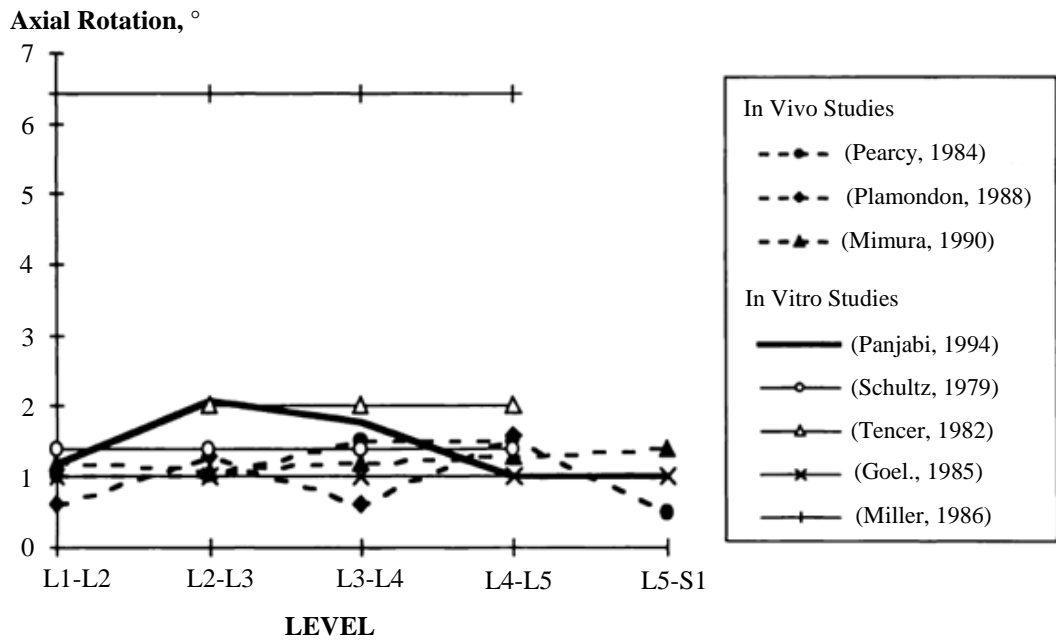
Axial Rotation, °

Figure 4.15. The variation of the axial rotation range of motion in the experimental studies for the human vertebral segments. Adapted Panjabi *et al.* (1994).

4.8 Relationship between Facet Articular Radius and Axial Rotation

In previous studies, the relationship between the facet radius and axial rotation has not been evaluated, which is probably due to the lack of studies and information on the facet curvature. Although there was no relationship between the facet radius and angle for both ovine and human vertebrae as demonstrated in Section 4.6, this investigation could provide better understanding of the facet joint behaviour in both species.

4.8.1 Ovine Vertebral Segments

The relationship was examined at T12T13, L1L2, L3L4 and L5L6 for the ovine vertebral segments where the facet joints were found to be curved compared to the other vertebral segments. The axial rotation motion of the vertebral segments was again taken from Wilke *et al.* (1997a). As shown in Figure 4.16, no correlation ($p > 0.05$) was observed between the axial rotation and the facet radius.
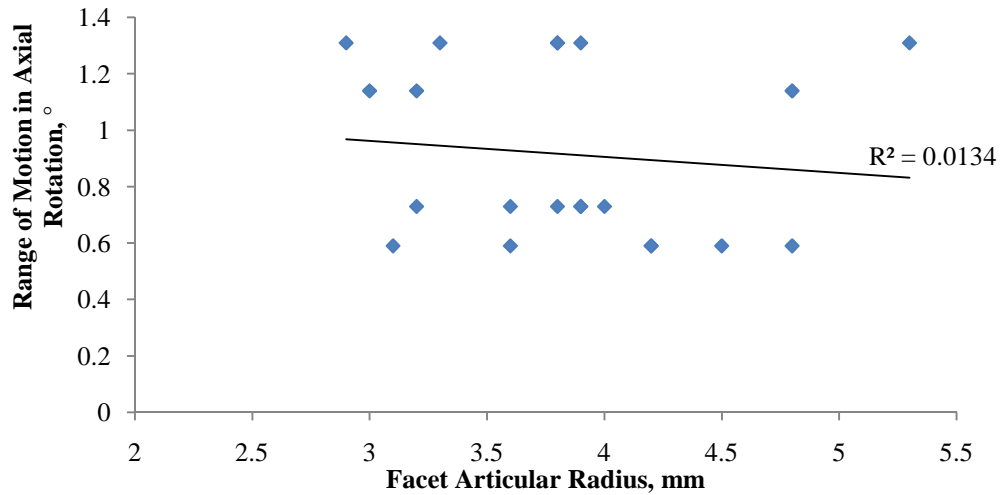
Figure 4.16. Correlation between facet articular radius and axial rotation (Wilke *et al.*, 1997a) of ovine vertebral segments.

4.8.2 Human Vertebrae

The relationship for the human vertebrae was observed at L1L2, L2L3 and L3L4 vertebral segments. Axial rotation data of the human vertebral segments from Panjabi *et al.* (1994) and Yamamoto *et al.* (1989) were once again used for the comparison. Statistically, significant correlations ($p<0.05$) were found between the facet radius and both experiment results of the axial rotation, where the axial rotation increased with the increasing of the facet radius as shown in Figure 4.17.
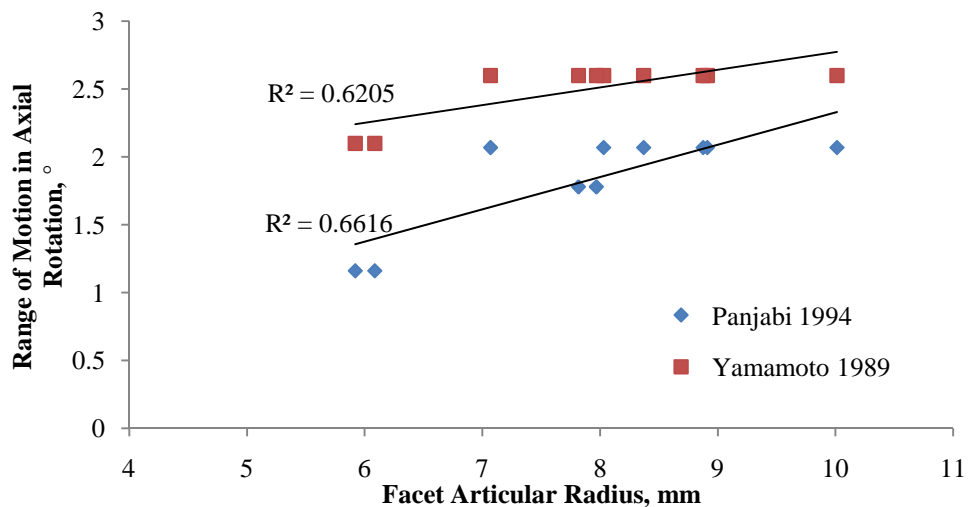
Figure 4.17. Correlation between facet articular radius and axial rotation (Yamamoto *et al.*, 1989, Panjabi *et al.*, 1994) of human vertebral segments.

4.9 Discussion

This study has presented a comprehensive set of morphological data for the facet joints of the ovine spine. The data were produced based on the μCT images of the vertebral segments to obtain the facet articular radius using an improved method while the facet orientation angle was determined according to the previous studies. In addition, human vertebrae were also evaluated for comparison purposes to investigate the similarity between these two species.

A previous experimental study has found that the range of motion in flexion, extension, axial rotation and lateral bending between the ovine and human spines were in similar range (Wilke *et al.*, 1997a). Since the spinal facet joints play an important role of the spine kinematic (Stokes, 1988, Miyazaki *et al.*, 2010), the similarities of the facet joints morphology between the ovine and human spines, such as similar trends of facet orientation angle and similar range of dimensional ratio of the facet articular radius, vertebral body width and vertebral body depth, observed in this study add evidence to support the premise that the ovine spine possesses a similar range of motion to the human spine. Based on the spinal motion similarities and the results from the present facet joint morphological study, the ovine facet joint could be used as a model to represent the human facet joint functional study, particularly at the L4 vertebral level. However, measurements of all human vertebral levels are needed in order to ensure it can be applied to other vertebral levels.

The present study indicates that a positive correlation is apparent between the facet angle and axial rotation although insignificant correlation was found with the axial rotation measured by Panjabi *et al.* (1994). This conflicting evidence was mainly due to the experiment methodology used to measure the range of motion as described by Panjabi *et al.* (1994). The correlation between the facet angle and axial rotation is also in disagreement to the previous study from Ahmed *et al.* (1990). However, this could be caused by facet angle measurement method: in their study, the measured angles were significantly higher than both the present and previous studies. The measured angles also varied substantially ranging from 5º to 55º for the L2L3 joint and 10º to 85º for the L4L5 joint (Ahmed *et al.* 1990). It appears that both the methodology to measure the facet angle and to measure the axial rotation are crucial in order to deduce the relationship between these two parameters.

In another parametric relationship, apparent correlation was observed between the facet radius and axial rotation for the human vertebrae, despite the lack of correlation found for the ovine vertebrae. In contrast, there was certainly no correlation between the facet articular radius and facet orientation angle for both ovine and human spines. However, data from only seven scans of the human vertebra were obtained in lumbar spine region between L1 and L4 vertebral level. The lack of the human vertebra data used in this morphological study may have influenced the variability of the measured facet articular radius and facet orientation angle. Therefore, more scan images of the human vertebra at all vertebral levels are needed in order for a more thorough analysis of the facet joint morphology to be carried out. Furthermore, the mean results obtained in the present study were only compared with the mean results from the literature. In future, these relationships could be revisited and may become more obvious if the measurement of the facet morphology and the range of motion could be carried out on the same specimens.

The present study has investigated simple two-dimensional properties in the transverse plane whereas in reality the joint is contained in an integrated complex three-dimensional anatomy. However, experimental studies of spine motions were mostly based on a single plane including axial rotation, lateral bending, flexion and extension, so making comparisons in two dimension is appropriate. Therefore, the methods used in this study could be useful in order to select which animal model would be appropriate to represent the human spine based on the morphological data for a particular area of research. This study indicated the potential usage of the ovine spine to represent human spine, especially in lumbar spine region, for lumbar facet joint range of motion studies.

Chapter 5: Results - Characterisation of Facet Cartilage Biomechanical Properties

5.1 Introduction

This chapter presents the results and analysis of the characterisation of the biomechanical properties of the facet cartilage. The first section presents the compression experiment results of the cartilage including the creep compression tests and the thickness measurements. The validation of the idealised computational axisymmetric model is outlined in the second section which was then utilised to derive the cartilage properties. This is followed with the outcome of the characterisation of the facet joint cartilage properties and the related parametric studies, and the overall results are discussed in the final section.

5.2 Biomechanical Measurement

5.2.1 Compression Test Repeatability

The repeatability of the compression test using a indenter was performed to demonstrate the reproducibility of the test methodology using the methods presented in Section 3.5.1. The mean and standard deviation (SD) of the cartilage deformation from the three repeated compression tests on the same specimen using five fresh ovine cartilage pins ($n=5$) are shown in Figure 5.1.
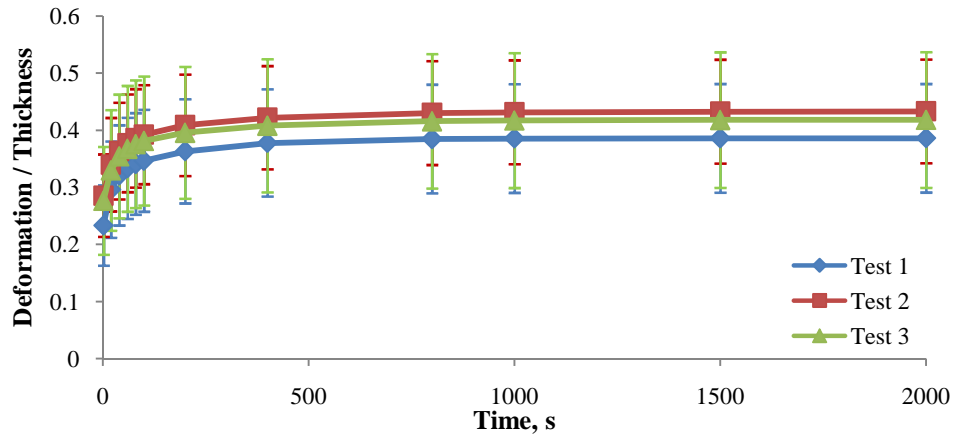
Figure 5.1. Cartilage deformation (mean ± SD) of three repeated compression tests undertaken on the same specimens. Between tests, the specimens were equilibrated in PBS solution for one hour.

Although the second and third test result mean values were higher than the initial test mean values by between 8% and 22%, they were still within a similar range to the initial test, due to the relatively large standard deviations between specimens. There was no clear trend between the results from second and third compression tests, however two distinct sets of results (Figure 5.2) were obtained from the tests which produced the large standard deviations between the specimens.
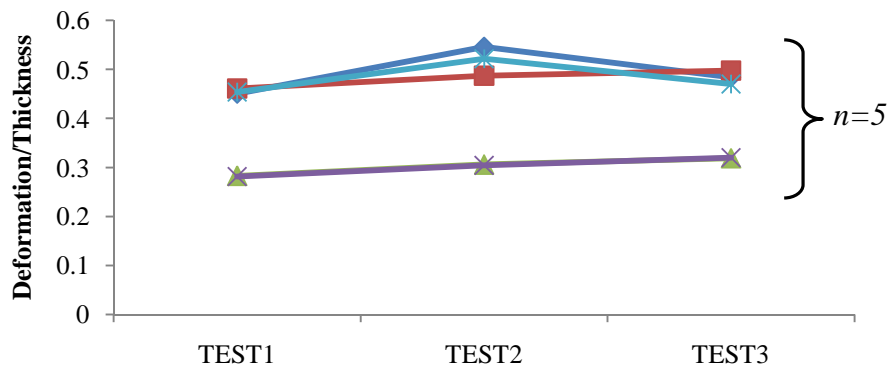
Figure 5.2. Cartilage deformation of three repeated compression tests for five cartilage pins at 2000 seconds.

In the present study, the cartilage pins were only submerged for one hour in the PBS solution before each test. A previous study using patellofemoral articular cartilage acquired from bovine knee joints has found that the cartilage should equilibrate in PBS for two hours prior to another test in order to obtain similar

deformations to the initial tests (Katta, 2007). However, the average thickness of the cartilage was 2.01 ± 0.25 mm and the compression test was subjected to 0.98 N force. Despite the cartilage equilibration time, the cartilage thickness and the compression force, the results demonstrate that the test methodology produced considerably repeatable results and the deformation curve trends were in good agreement with the results obtained from previous studies (Mow *et al.*, 1989, Pickard *et al.*, 1998).

5.2.2 Cartilage Thickness

The µCT imaging measurement method was undertaken in order to verify the cartilage thickness measured using the compression test. The percentage of the cartilage thickness difference measured between the two methods for seven fresh cartilage pins (*n=7*) is shown in Table 5.1 and Figure 5.3 using various compression forces. A slight difference of between 3% and 5% was found when the compression force was increased to 3.5 N. At 4.4 N, the difference was less than 2% and a distinct peak force was observed which suggested that the needle went through the cartilage straight to the bone, as shown in Figure 5.4b.

Based on the results, it is suggested that the appropriate compression force to measure the ovine facet cartilage is at least 3.5 N. The mean cartilage thickness measured from ten fresh cartilage pins (*n=10*) using the compression method was found to be 0.52±0.1 mm. The cartilage thickness was observed to be relatively uniform across the specimen as shown in Figure 5.5.

Table 5.1. Comparison of the cartilage thickness measured between compression test and µCT.

Sample	Compression Force, N	Cartilage Thickness, mm		Thickness Difference, %
		Compression Test	µCT	
Specimen 1	1.6	0.25	0.44	43.2
Specimen 2	1.6	0.26	0.52	50.0
Specimen 3	2.6	0.27	0.32	15.6
Specimen 4	2.6	0.39	0.47	17.0
Specimen 5	3.5	0.41	0.43	4.6
Specimen 6	3.5	0.37	0.38	2.6
Specimen 7	4.4	0.59	0.60	1.7
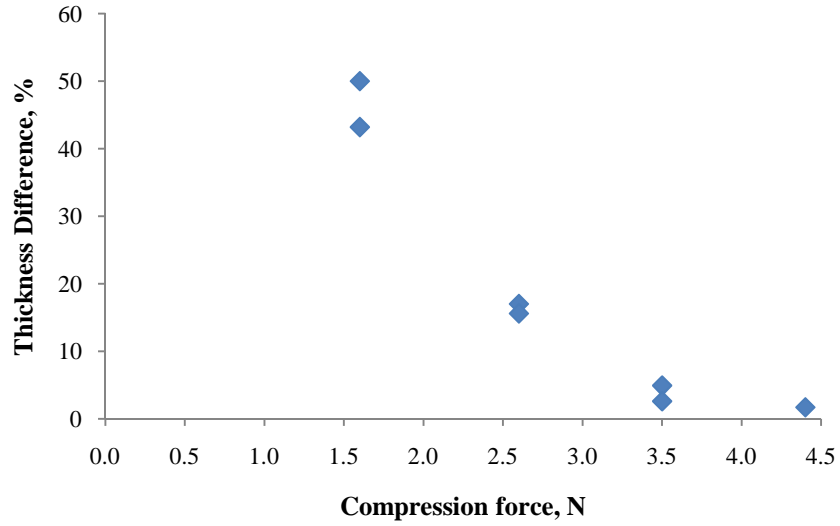
Figure 5.3. Percentage of the cartilage thickness difference between μCT and compression test measurements.
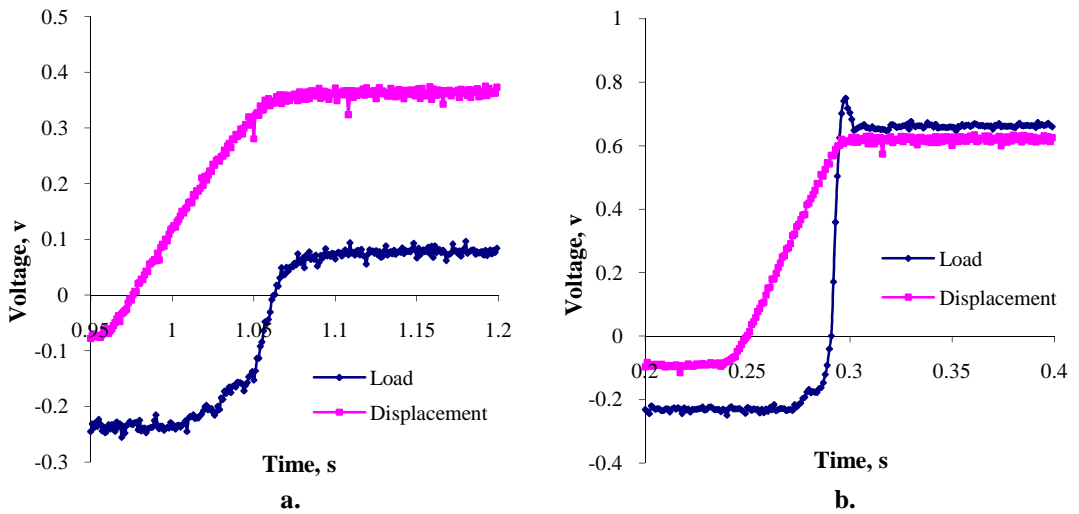
Figure 5.4. Examples of cartilage thickness compression test result using different compression force a. 1.6 N b. 4.4 N.
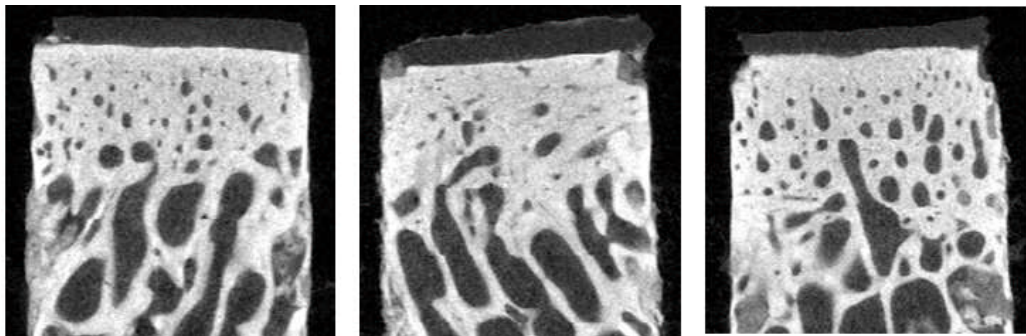
Figure 5.5. Examples of μCT scan image of cartilage pins at middle slice.

5.2.3 Compression Test of the Ovine Facet Subchondral Bone

The creep compression tests using an indenter were performed on six ovine subchondral bone specimens (*n=6*) using the methods described in Section 3.5.2. However, negligible deformation was recorded on all of the bone specimens, as shown in Figure 5.6. This is probably due to the density of the bone (Figure 5.5), where the specimens were extracted from relatively young sheep between four and five years old compared to the skeletal maturity of the sheep at 3 years old and life span between 10 to 15 years (Reinwald and Burr, 2008). This result confirms that the ovine subchondral bone did not influence the cartilage deformation in the compression test.
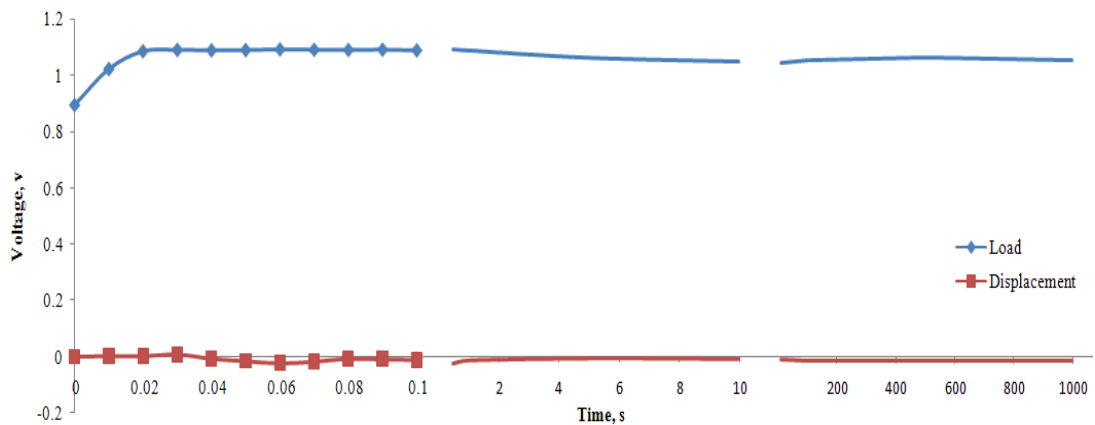
Figure 5.6. Example of ovine subchondral bone creep compression test, showing three time intervals to illustrate the lack of displacement over the whole test period.

5.3 Computational Results for Idealised Axisymmetric Model

5.3.1 Implementation of Contact Dependent Flow

The contact dependent flow algorithm was developed in order to change the flow conditions depending on the contact stress at the cartilage surface nodes. The present results were compared to the results generated by Pawaskar (2006) to verify the algorithm implementation as described in Section 3.7.1.2. Figure 5.7 demonstrates the comparisons of the contact pressure distribution on the cartilage surface at 2 s and 1000 s for both stress-relaxation and creep-deformation simulations. In addition, the pore pressure distribution on the cartilage surface of the

creep-deformation is also compared in Figure 5.8. As can be seen, the present results were identical with the results produced by Pawaskar (2006) which confirmed the correct implementation of the contact dependent algorithm.
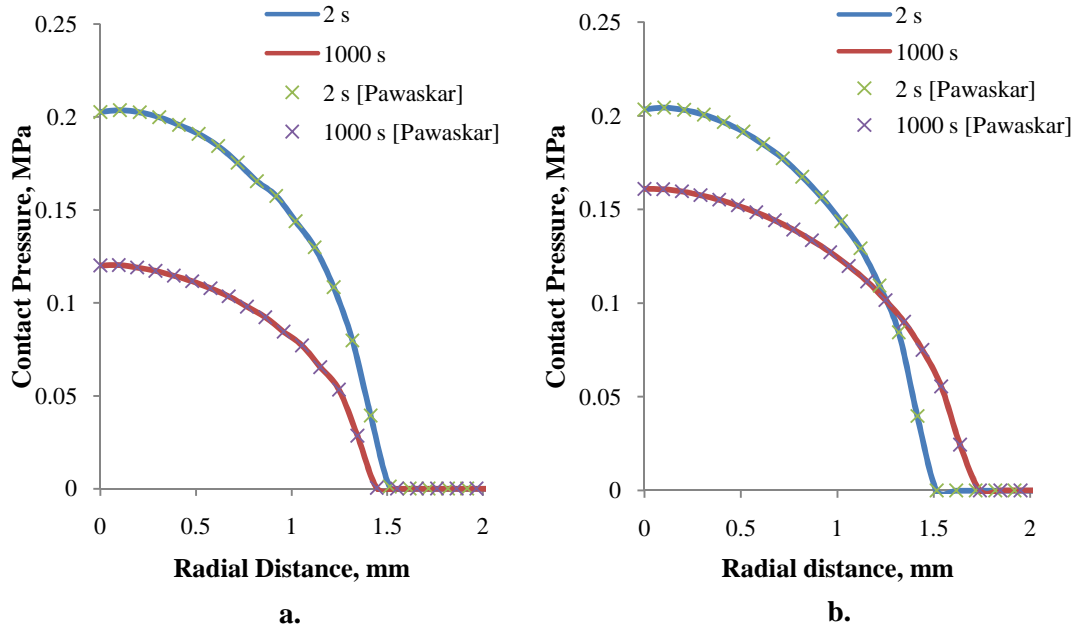
Figure 5.7. Contact pressure distribution at cartilage surface, a. Stress-relaxation b. Creep-deformation, showing comparison between current study and the previous results of Pawaskar (2006).
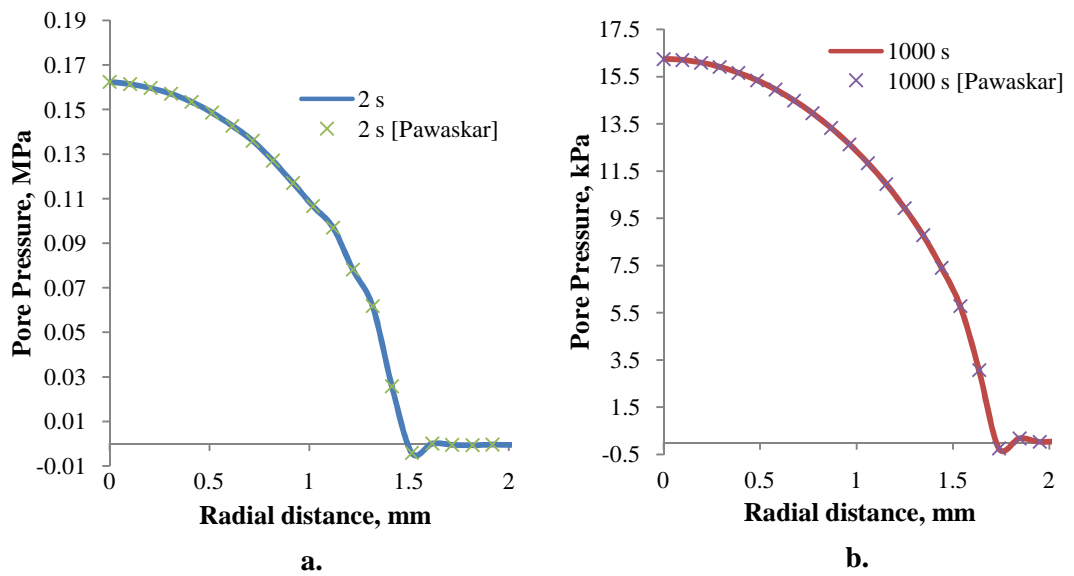
Figure 5.8. Pore pressure distribution at cartilage surface of creep-deformation, a. 2 seconds b. 1000 seconds, showing comparison between current study and the previous results of Pawaskar (2006).

5.3.2 Mesh Sensitivity Analysis

The mesh sensitivity analysis was performed to obtain an optimised mesh density for the axisymmetric model as described in Section 3.7.1.4. The FE meshes were varied such that the width and height of the cartilage were maintained at ten to one element ratio respectively from 160 to 1440 elements. In addition, a concentrated mesh density at the contact area consisting of 300 elements was included to observe the efficiency.

The contact pressure and deformation of the cartilage during 1000 s did not show any marked difference for all the meshes observed, as shown in Figure 5.9. In addition, comparisons of the contact pressure distribution on the cartilage surface at 2 s and 1000 s were examined and illustrated in Figure 5.10. Although the distributions were similar along the contact distance, slight differences were observed at the edge of the contact. The concentrated mesh was found to be optimum due to the accuracy and the computational time required. The results produced from the concentrated mesh were the most similar to the one produced from 1440 elements mesh. However, the computational time required for the concentrated mesh was only 96 s compared to 214 s for the 1440 elements mesh. Although the magnitude of the difference in the computational time was insignificant, it would increase tremendously in the three-dimensional model because substantial differences in the element numbers would be generated.
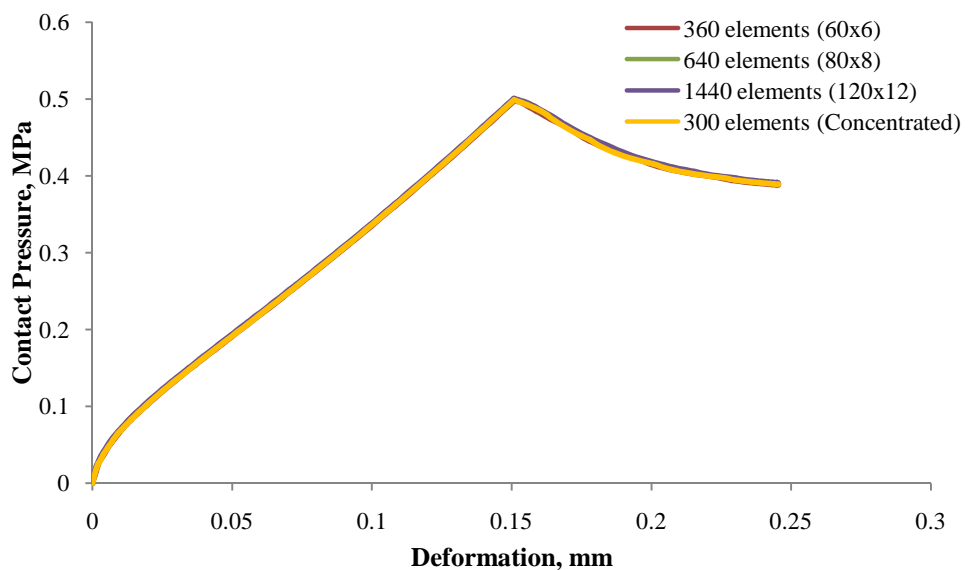
Figure 5.9. Contact pressure versus deformation of the cartilage during 1000 seconds.
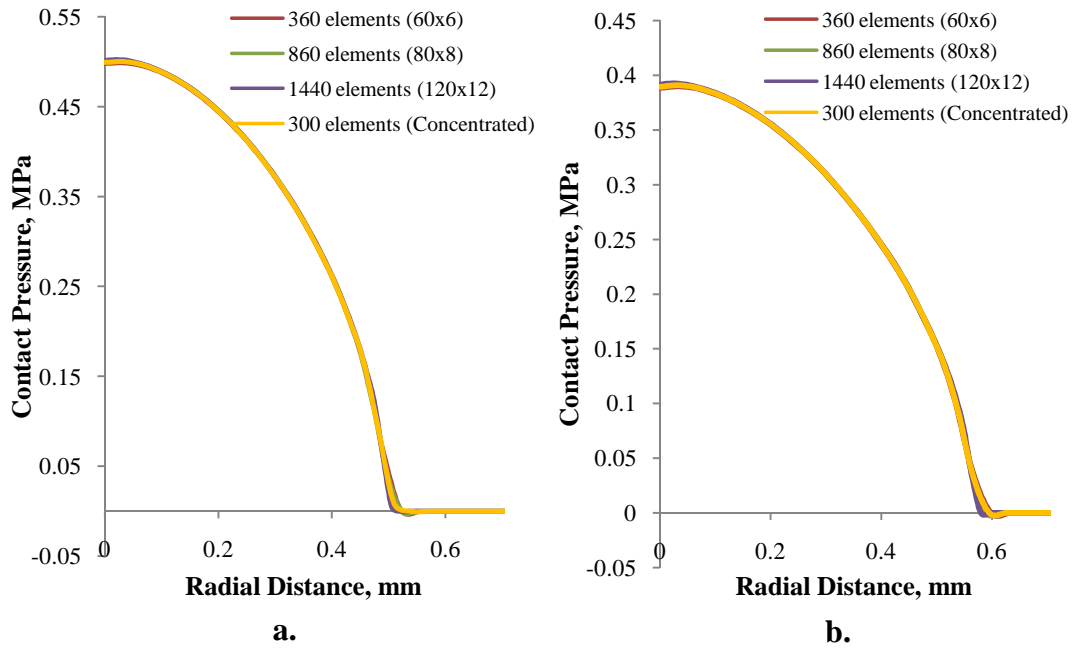
Figure 5.10. Contact pressure distribution on cartilage surface a. 2 seconds b. 1000 seconds.

5.4 Cartilage Biomechanical Properties

5.4.1 The Effects of Cartilage Storage

The objective of this study was to investigate if there was an alternative storage method of the cartilage pin specimens in order to maintain the cartilage properties comparable to the fresh cartilage. Three different conditions of cartilage pin storage were studied to examine the effect on the derived biphasic cartilage properties of elastic modulus and permeability as described in Section 3.8. Figure 5.11 shows the comparison of the properties for ten fresh cartilage pins (*n=10*), five frozen joint cartilage pins (*n=5*) and four frozen cartilage pins (*n=4*) from the ovine facet joints.
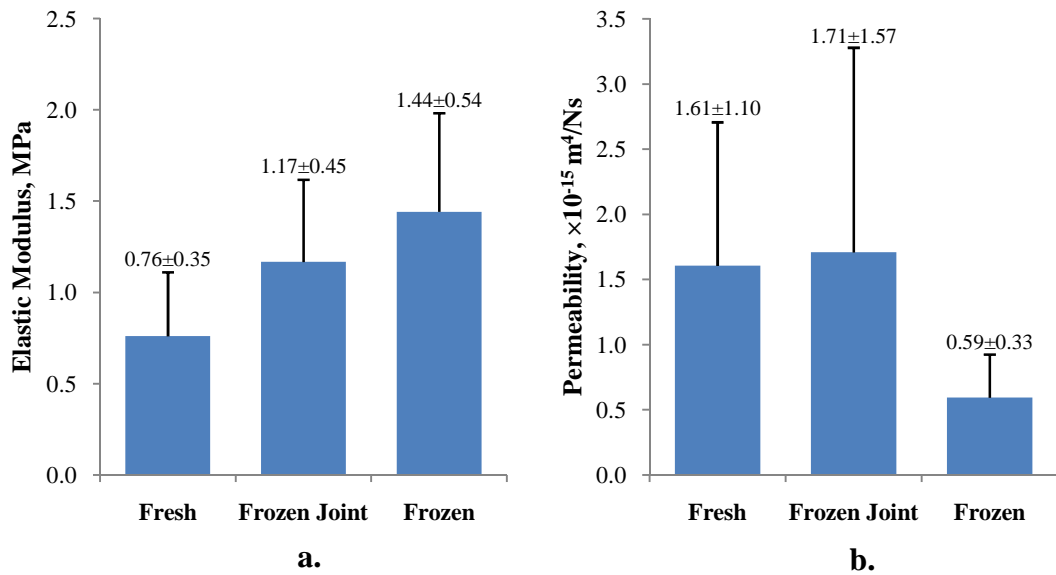
Figure 5.11. Comparison of the cartilage biphasic properties (mean ± SD) for different storage conditions a. Elastic modulus b. Permeability.

The cartilage biphasic elastic modulus and permeability derived from the fresh cartilage pins were 0.76 ± 0.35 MPa and $1.61\pm1.10 \times 10^{-15}$ m^4/Ns respectively. A one-way ANOVA statistical analysis ($p<0.05$) indicated that there was no statistical difference in the elastic modulus and permeability between the fresh and frozen joint cartilage pin. However, significant differences were found for both properties between the fresh and the frozen cartilage pins. Based on these results, it would appear that the freeze-thaw cycle does not change the cartilage elastic modulus and permeability compared to the fresh cartilage pins providing that the whole facet joint is frozen in an intact state.

5.4.2 The Effects of Cartilage Poisson's Ratio and Void Ratio

This parametric study was carried out, as described in Section 3.8.1, to demonstrate the effect of the cartilage Poisson's ratio and void ratio on the cartilage deformation curve because the curve was utilised to derive the cartilage properties. Figure 5.12a shows the difference of the cartilage deformation curves for each Poisson's ratio applied in the biphasic poroelastic axisymmetric FE model. Similar curves were obtained when the value of the cartilage Poisson's ratio was varied between 0.0 to 0.12. Although the cartilage Poisson's ratio characterised previously

were below 0.12, a higher value of 0.20 was also applied and approximately 9% difference was found in the deformation curve compared to the initial curve.
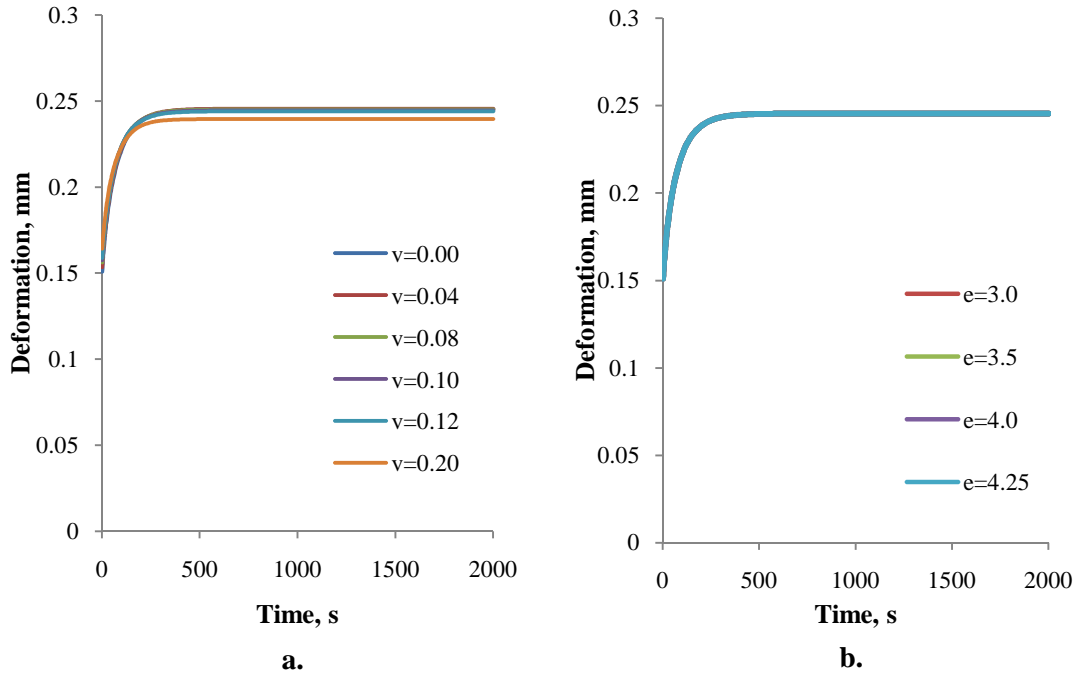
Figure 5.12. Cartilage deformation curve a. Cartilage Poisson's ratio sensitivity, b. Cartilage void ratio sensitivity.

A similar protocol was applied to examine the sensitivity of the void ratio of the cartilage. Figure 5.12b shows the curves generated from 3.0 to 4.25 void ratio of the cartilage were almost identical. This therefore confirms that the void ratio has no difference on the cartilage deformation curve generated from the axisymmetric FE model.

5.4.3 The Effects of Subchondral Bone Elastic Modulus

The effects of the subchondral bone elastic modulus on the cartilage deformation was investigated using the axisymmetric FE model as described in Section 3.8.2. Figure 5.13 shows the curves generated from 1510 MPa to 50 MPa elastic modulus of the subchondral bone were almost identical. The curve started to distort when 20 MPa elastic modulus was applied to the subchondral bone and finally around 7% difference was found in the deformation curve compared to the initial curve when using 10 MPa. Furthermore, the subchondral bone was found to

deform when using 10 MPa elastic modulus for the subchondral bone compared to 1510 MPa, as illustrated in Figure 5.14.
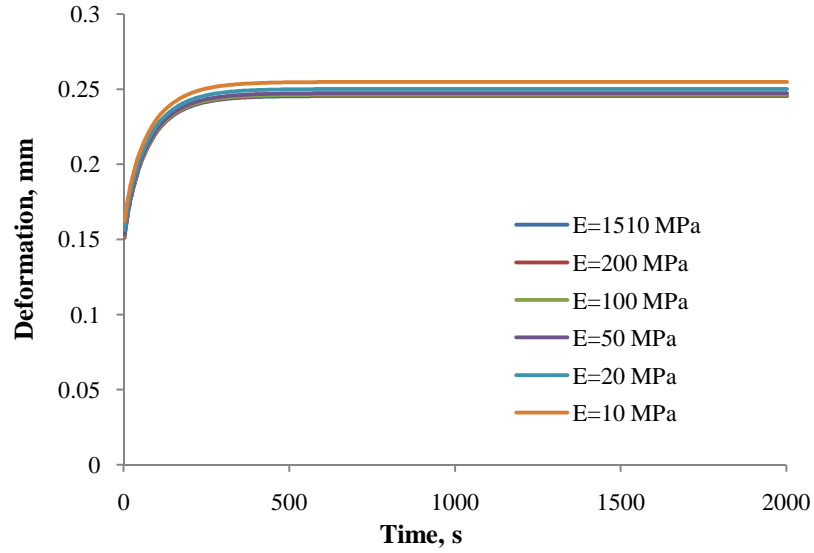
Figure 5.13. Cartilage deformation curve of subchondral bone elastic modulus sensitivity.
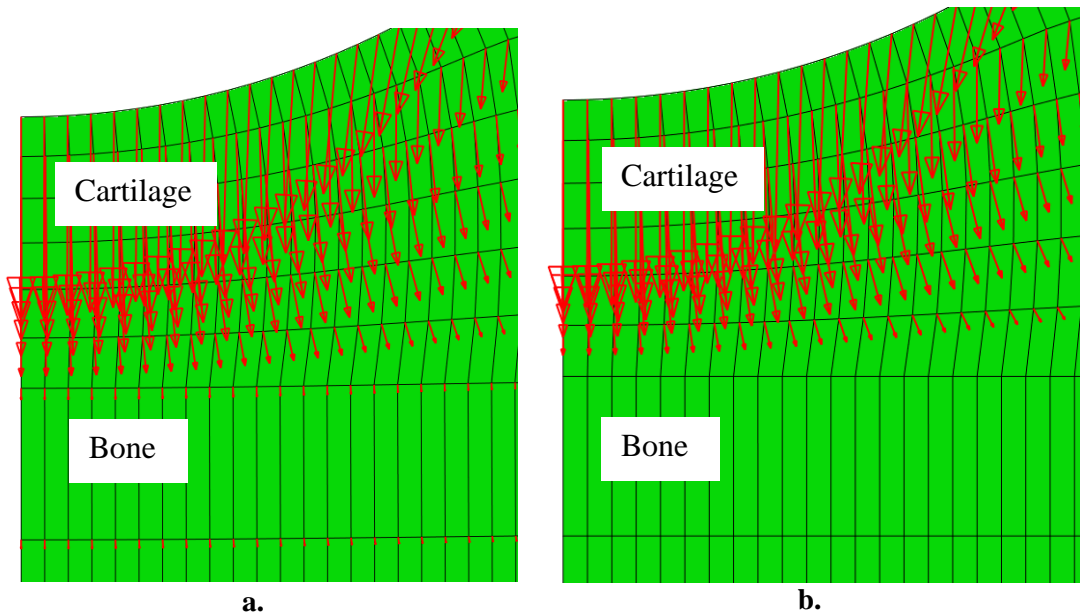
Figure 5.14. Spatial deformation at nodes for elastic modulus of the subchondral bone at 2000 s. The red arrows show the direction of the deformation. a. *E*=10 MPa, showing deformation in the bone b. *E*=1510 MPa, showing no bone deformation.

5.4.4 The Effects of Indenter Radius

Comparisons of the characterised cartilage properties were carried out to examine the effect of using a different size of indenter diameter. The compression tests were performed on six fresh cartilage pins (*n=6*) using a 6.3 mm diameter spherical indenter as described in Section 3.8.3. Figure 5.15 shows the cartilage properties obtained from both indenter sizes.
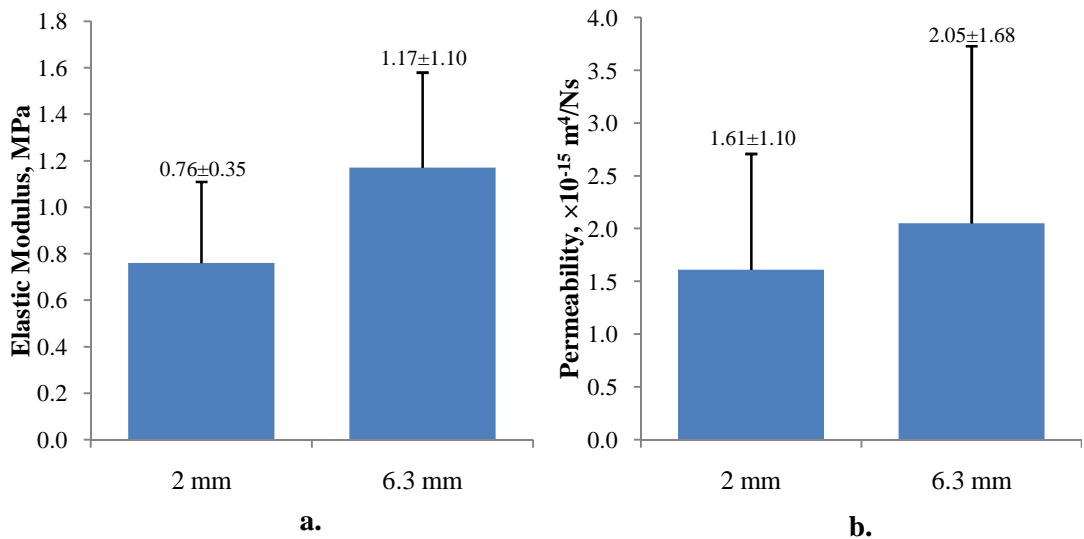
Figure 5.15. Comparison of the cartilage biphasic properties (mean ± SD) for 2 mm and 6.3 mm indenter diameter a. Elastic modulus b. Permeability.

The mean cartilage properties characterised from 6.3 mm diameter indenter were higher compared to the 2 mm diameter indenter. Furthermore, the variations in the estimated properties were also increased when 6.3 mm diameter indenter was used. However, statistical t-test analysis (*p<0.05*) shows that differences were not significant for either the elastic modulus or the permeability of the cartilage between the two indenter sizes.

5.4.5 The Effects of Cartilage Surface Curvature

The cartilage surface curvature sensitivity study was carried out to observe the effects on the characterised properties in the axisymmetric FE model. Both concave and convex curvatures were evaluated with the cartilage surface radius of 20 mm and 40 mm. Figure 5.16 shows the differences in the derived cartilage elastic

modulus and permeability obtained from different radii of curvature. The negative and positive values of the radius represent the concave and convex curves respectively.
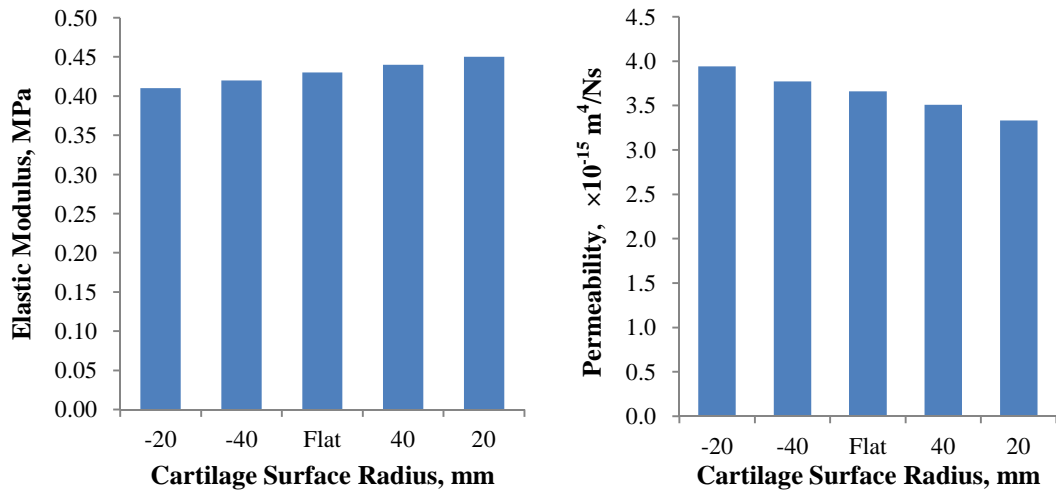
Figure 5.16. Cartilage biphasic properties characterised from different cartilage surface radius.

Based on the results, the cartilage curvature had an effect on the estimated cartilage properties. The smaller cartilage surface of 20 mm radius produced higher difference of the characterised properties compared to the 40 mm radius. In addition, the 20 mm radius cartilage surface generated 9% difference in the permeability and 5% difference in the elastic modulus, compared to the flat cartilage. This indicates that the cartilage permeability would be most affected by the cartilage curvature during the characterisation process. However, the curvature produced from the axisymmetric model was not best to represent the three-dimensional curvature of the actual cartilage pin specimen. Therefore, this study was extended using specimen-specific model to model the actual three-dimensional curvature of the cartilage pin.

5.4.6 The Effects of Three-Dimensional Curvature of Cartilage Surface

The results obtained from the axisymmetric model indicated that the curvature of the cartilage surface influenced the characterised cartilage properties. Therefore, further investigation was performed using the specimen-specific model to examine the cartilage deformation of the actual three-dimensional curvature as described in

Section 3.8.4. This enabled the three types of the cartilage surface, which were flat, gradient and specimen-specific curvature, to be explored. However, the specimen-specific model greatly increased the computational time, and approximately 1390 hours were needed to complete the simulation. Figure 5.17 shows the comparison of the cartilage deformation curves produced from the three different models.
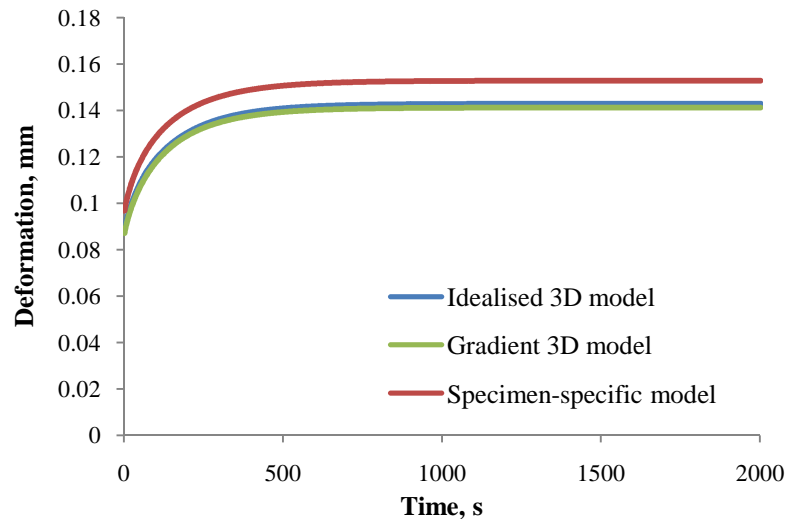
Figure 5.17. Comparison of the cartilage deformation between the specimen-specific and idealised 3D models.

The gradient model did not significantly alter the cartilage deformation compared to the flat model. However, the specimen-specific model increased the deformation by approximately 7% compared to the flat model.

In order to determine how this difference in the simulated deformation would affect the derived cartilage properties, ideally the properties in the specimen-specific model would have been iteratively changed until the predicted deformation matched the experimental results, and the properties compared with the axisymmetric case. However, substantial computational time would have been required in order to characterise the cartilage properties using the specimen-specific model to curve-fit the experiment data because the process may lead up to 20 complete simulations, each lasting approximately 1400 hours. Therefore, in order to estimate the differences in the cartilage properties generated from the actual three-dimensional curvature model, the axisymmetric model was utilised to characterise the properties because its deformation curve was very similar to the idealised 3D model (Figure

3.14). The axisymmetric model was simulated and iterated to match to the deformation curve generated from specimen-specific model (Figure 5.18) and the derived cartilage properties are shown in Figure 5.19.
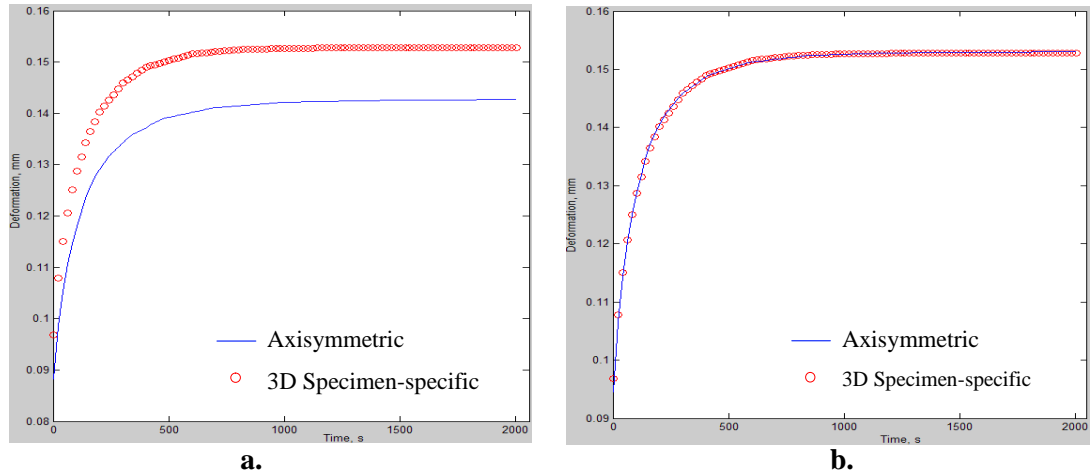
Figure 5.18. The cartilage deformation curve matching process to the specimen-specific model a. Showing initial simulation of both models with the same biphasic properties b. After iteratively changing the properties of the axisymmetric model until it fitted the 3D specimen-specific model.

A higher percentage difference was again observed for the cartilage permeability compared to the elastic modulus. The actual three-dimensional curvature altered the characterised cartilage permeability by 35% and the elastic modulus by 13% as compared to the flat cartilage.
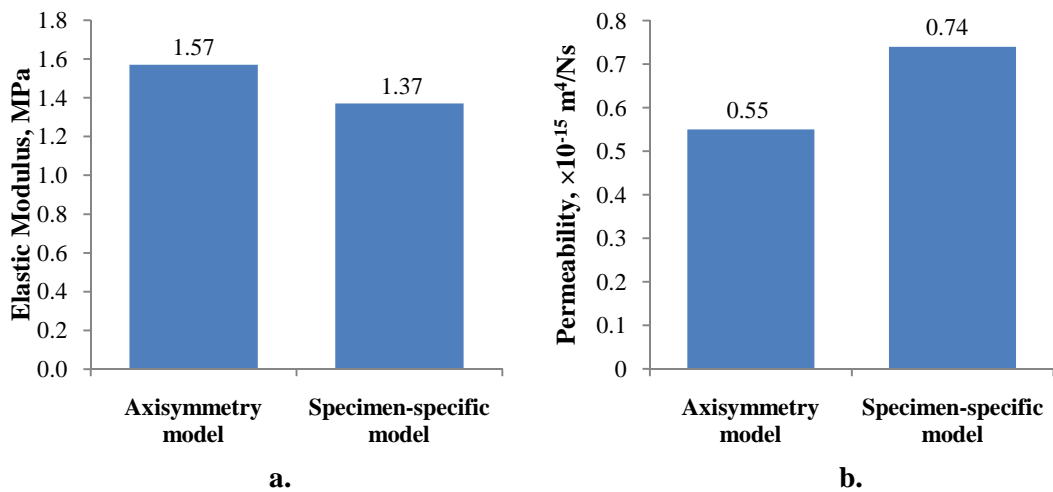
Figure 5.19. Comparison of the cartilage properties characterised from the specimen-specific and axisymmetric models a. Elastic modulus b. Permeability.

5.5 Discussion

In the present study, the cartilage biomechanical properties of the ovine facet joints were characterised for the first time. The developed experimental methodology of the compression test using an indenter performed on the facet cartilage pin generated reproducibility and repeatability in the results. This was crucial because the cartilage deformation data from the compression test was used to derive the cartilage biphasic properties.

Experimental protocols in cartilage research typically require some type of storage protocol particularly between harvesting and testing. Although there are conflicting opinions on the effect of freezing to the cartilage biomechanical properties as discussed in Section 1.5.3.2, it has been shown in the present study that freezing at -20 ℃ altered the biomechanical properties of the cartilage when it was stored as extracted pins. This is supported by another study where freezing at -20 ℃ altered the biomechanical properties resulting from the damage to the extra-cellular matrix (ECM) and cells (Willet *et al.*, 2005). Instead of this method of cartilage storage, some studies have proposed that the cartilage should be maintained as normal using tissue culture methods (Black *et al.*, 1979, Brighton *et al.*, 1979, Kwan *et al.*, 1992, White *et al.*, 1999).

However, this study has found the cartilage extracted from the frozen intact facet joint which was kept at -20 °C within two weeks subjected to a freeze-thaw cycle to have comparable biomechanical properties to the fresh cartilage. It indicates that the cartilage tissue was able to survive the freezing and thawing cycles when enclosed within the intact facet joint, in terms of maintaining the biomechanical properties. This storage protocol of keeping the cartilage in an intact joint could potentially be applied to other synovial joints for future mechanical studies on the cartilage. Furthermore, the storage protocol could be implemented for the functional spinal unit such as in range of motion and load-displacement studies, where the experiment can be undertaken on specimens following a freeze-thaw cycle without concern that the facet cartilage properties will have been substantially altered. However, no biological characterisation of the tissue was undertaken in this study and so the efficacy of this storage method for biological studies would require further testing.

Generally, cartilage thickness has been measured using either an imaging method such as MRI or direct method using a compression test using a needle indenter as described in Section 1.5.3.3. However, it appears that the thickness measured from imaging methods has been higher than that measured using the compression test, as shown in Table 5.2. Moreover, the plane resolution of the MRI scan was between 0.25 mm and 0.5 mm with the image section thickness between 0.3 mm and 3 mm, compared to µCT scan resolution of 20 to 40 µm. Therefore, this study utilised the compression test using a needle indenter to determine the cartilage thickness of the ovine facet joints and then compared the results to µCT scan information. Based on the thickness measured from these two methods, it was observed that the compression force was important to determine the thickness of the cartilage since the lower force caused the cartilage thickness to be underestimated. The mean thickness of the ovine facet cartilage was found to be 0.52±0.1 mm and the compression force needed to be at least 3.5 N. As demonstrated in Table 1.4, the cartilage thickness varies for each of the synovial joints in human body and therefore, the required compression force to measure the thickness is likely to also vary. This is because the resistance to the indenter is to some extent provided by the frictional shear forces on the shaft of the indenter, so the thicker tissue has more of the shaft of the indenter in contact with the tissue and the greater frictional resistance.

Table 5.2. Comparison of the cartilage thickness measured between MRI and compression test.

Cartilage	MR Imaging (mm)	Compression Test (mm)
Hip-Femoral head	1.14 - 2.84 (Nakanishi, 2001)	1.06 - 1.83 (Athanasiou, 1994)
Ankle-Tibia	1.21 ± 0.14 (Millington, 2007)	0.95 – 1.30 (Athanasiou, 1994)
Elbow-Radial head	1.20 (Graichen, 2000)	0.87 – 1.17 (Schenck, 1994)

In order to characterise the cartilage biphasic properties, both experimental and computational methods were required to be incorporated. A contact dependent flow algorithm developed by Pawaskar (2006) was implemented in the biphasic poroelastic axisymmetric FE model to simulate the experimental creep compression test using an indenter performed on the cartilage pin. Parametric studies of the

cartilage Poisson's ratio, cartilage void ratio and subchondral bone elastic modulus were performed because the properties for these tissues had to be assumed. Although in previous studies the Poisson's ratio was determined to be less than 0.1, similar cartilage deformations were observed when values between 0.0 and 0.12 for the cartilage Poisson's ratio were applied. Moreover, the cartilage deformation curves were almost identical for the void ratio values from 3.0 to 4.25 which represented 60% to 85% of fluid in the cartilage that has been reported in the literature (Mow 2005). For the subchondral bone, consistent cartilage deformation curves were found when the elastic modulus was varied from 1510 MPa to 50 MPa and the curve only started to distort when a modulus of 20 MPa was imposed.

Although there have been extensive studies to characterise the biphasic properties of the cartilage in human synovial joints, limited studies have been carried out to characterise the biomechanical properties of the cartilage in the spinal facet joint. Based on these characterised properties, it appears that the cartilage properties vary in different joints in order to accommodate the function of the joint as shown in Figure 5.20. The functional characterisation of the facet joint articular cartilage has only been studied recently using the canine spine (Elder *et al.*, 2009). However, the compression test using a porous flat-ended indenter was performed on the cartilage that had been separated from the subchondral bone using a scalpel and the biphasic properties were derived using the analytical solution for linear biphasic theory. Although the bone itself is unlikely to have affected the characterised cartilage properties, the method of extraction may cause greater damage to the tissue than using the full cartilage-bone plug. In contrast, this study has characterised the cartilage biphasic properties of the ovine facet joints where the compression test was performed on the cartilage attached to the subchondral bone. The biphasic properties were derived using computational method based on the experiment where the elastic modulus and permeability were 0.76 ± 0.35 MPa and $1.61\pm1.10 \times10^{-15}$ m^4/Ns respectively, which within the range of the previous characterised properties.
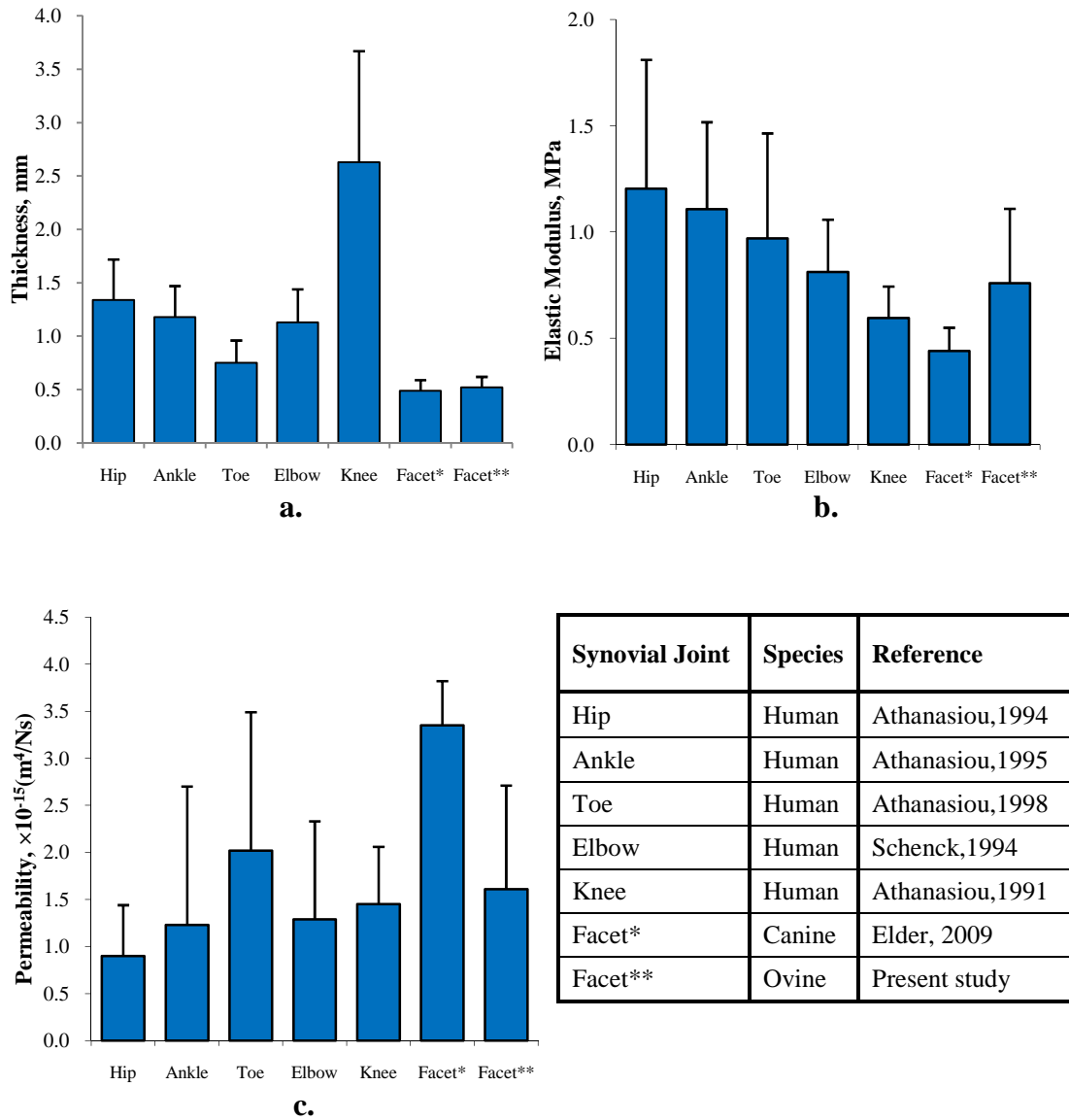
Figure 5.20. Comparisons of cartilage biomechanical properties from different synovial joints. a. Thickness b. Elastic modulus c. Permeability. The species used and references for each study are shown.

During the cartilage properties characterisation, the cartilage surface in the biphasic axisymmetric FE model was assumed to be flat since this appears to have been assumed in most of the previous studies in order to evaluate the cartilage behaviour (Warner *et al.*, 2001, Jin and Lewis, 2004, Choi and Zheng, 2005). However, this assumption was not appropriate in this study because most of the cartilage pin specimens were found to be curved. Therefore, a specimen-specific FE model was developed to replicate the actual three-dimensional curvature of the cartilage surface and simulate the creep-compression test performed in the experiment. The difference of the characterised cartilage properties between the

actual three-dimensional curvature and the flat cartilage surface was 35% for the permeability and 13% for the elastic modulus. Based on these results, it clearly indicates that the cartilage curvature does affect the cartilage deformation in the creep-deformation simulation. Moreover, this phenomenon was also observed in another computational study where the facet curvature play an important role in the contact stress distribution in the facet joint (Holzapfel and Stadler, 2006).

Chapter 6: Application of Specimen-Specific Modelling Methods to the Human Facet Joint

6.1 Introduction

This chapter presents a pilot study where the methodology developed in the previous chapters for the experimental testing and specimen-specific modelling of ovine facet cartilage pins was extended to evaluate cartilage pins extracted from human facet joints. Due to the limited availability and age of the tissue, the number of specimens obtained was small, and they were found to have completely degenerated cartilage with weak subchondral bone. Therefore, the methodology was adapted to evaluate the effects of the weak underlying bone. This chapter outlines the methodology used and the results obtained from the pilot study, and makes recommendations for further testing of human facet cartilage in the future.

6.2 Methods

6.2.1 Specimen Preparation of Facet Cartilage Pin

Following approval by the Joint MAPS Engineering Ethics Committee, University of Leeds (Reference: MEEC 09-088), the thoracic region between T1 and T4 from a human spine (age and sex unknown) was used in this study. The 4 mm diameter facet cartilage pins were extracted according to the procedure described in Section 3.2.2. However, extra care had to be taken during the pin extraction because the facet underlying bone was in weak condition which could damage the trabecular bone architecture easily during the coring process. From visual observation, the cartilage was found to be totally degenerated in all of the facet joints and, due to the fragility of the bone, only two facet cartilage pins ($n=2$) were successfully extracted, both from the T3T4 facet joints.

6.2.2 Scan Set-up for Facet Cartilage Pin

The scan set-up described in Section 3.3 was adapted to scan the human facet pins. The µCT scans were performed in order to generate the three-dimensional specimen-specific model from the scan data. The scan images also enabled better visualisation of the bone and cartilage conditions. As can be seen from the scan images taken from the two specimens in Figure 6.1, the cortical bone was still present with underlying weak trabecular bone, but virtually no cartilage was detected on either specimen.

a.   **b.**
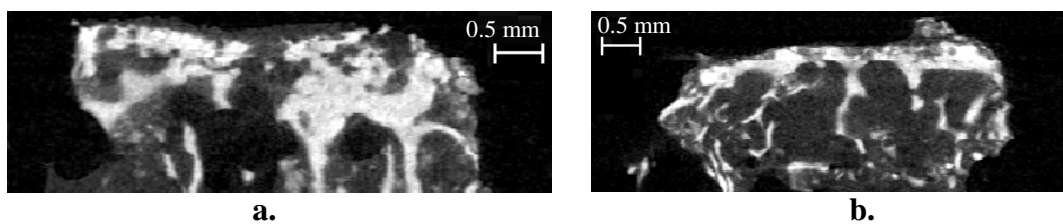
Figure 6.1. µCT scan image of the human facet pin a. Specimen 1 b. Specimen 2.

6.2.3 Creep Compression Test

Although there was very little cartilage on the facet pins observed in the µCT scan image, creep compression tests using an indenter were carried out to evaluate the potential of the procedure for use on human tissue and observe the deformation of the underlying bone in weak condition. The experimental data was then used to characterise the biphasic properties of the facet pins as the pins were submerged in PBS during the test. The creep compression tests on the two human facet pins (*n=2*) were performed according to the protocol described in Section 3.5. An indenter weight of 0.24 N, as was used to characterise the ovine facet cartilage, was applied using a 2 mm diameter spherical indenter.

6.2.4 Characterisation of Biphasic Properties Using Axisymmetric Model

The characterisation of the biphasic properties was performed to determine the composite elastic modulus ($E_{composite(axi)}$) and permeability of the facet pin which consisted of the bone and fluid. The compression test using an indenter was

simulated using an axisymmetric biphasic poroelastic FE model consisting of a flat-ended bone of radius 2 mm, with the thickness measured from the µCT scan image, and a rigid spherical indenter of 1mm radius. The model was then discretised into a finite element mesh which consisted of 1000 CAX4RP elements with concentrated mesh density around the contact area, as shown in Figure 6.2.
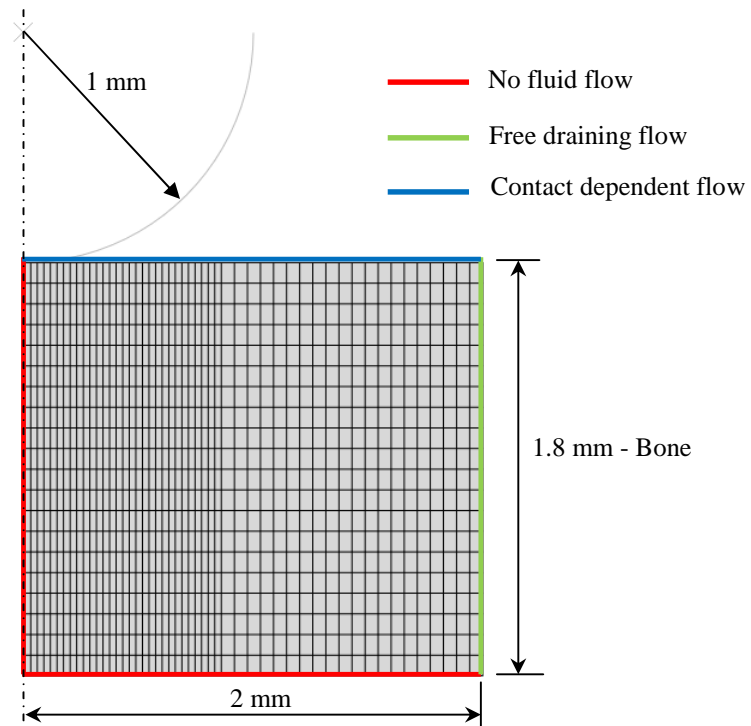
Figure 6.2. Axisymmetric FE model of the human facet pin.

Boundary and interface conditions were applied on the bone and indenter, according to details described in Section 3.7.1.2. The bottom nodes of the bone were constrained in both the horizontal and vertical directions, whilst the nodes on the axis were constrained in the horizontal direction. The spherical indenter was only permitted to move in the vertical direction, as the horizontal direction and rotational movements were constrained. The fluid flow, as illustrated in Figure 6.2, was prevented on the bottom and vertical symmetry axis (in the horizontal direction) of the bone surfaces whilst the outer edge nodes of the bone were maintained at zero pore pressure so as to allow unrestricted fluid flow. For the bone surface which was in contact with the indenter, the contact dependent flow algorithm (Pawaskar, 2006) was imposed.

The Poisson's ratio of the subchondral bone was assumed to be 0.3 (Shirazi and Shirazi-Adl, 2009) and the void ratios of both specimens were calculated by dividing the difference between the total volume and the bone volume, over the total volume where both of the volumes were determined using image processing software (ScanIP v3.2-Simpleware Ltd, Exeter UK). The void ratios calculated for Specimen 1 and Specimen 2 were 3.3 (66% fluid) and 3.8 (76% fluid) respectively. In order to characterise the biphasic properties of the facet pin, a similar protocol to that described in Section 3.8 was applied to estimate the elastic modulus and permeability.

6.2.5 Characterisation of Elastic Modulus of the Facet Subchondral Bone using Specimen-Specific Model

6.2.5.1 Development of Specimen-Specific Model

In this study, two types of specimen-specific models were developed to represent the subchondral bone. In one ('specimen-specific trabecular model'), the actual architecture of the trabecular structure was replicated while in the other model ('specimen-specific solid model') a solid continuum was used to represent the combination of trabecular bone and trabecular space as one material. These enabled estimates of the elastic modulus of the bone tissue (E_{bone}) and the composite elastic modulus ($E_{composite(3D\ solid)}$) to be made respectively.

The three-dimensional geometrical data of the facet pin obtained from the micro-computed tomography scan was utilised to develop these specimen-specific models. The images, which had a resolution of 20 µm, were segmented as described in Section 3.7.3.1 using ScanIP v3.2 (Simpleware Ltd, Exeter, UK) software to generate a specimen-specific trabecular model as shown in Figure 6.3a. However, the mask was only defined for the bone because the cartilage was not detectable in the scan images. For the specimen-specific solid model, the paint operation tool in ScanIP v3.2 (Simpleware Ltd, Exeter, UK) software was used to fill the spaces of the porosity in the bone as shown in Figure 6.4a. The specimen-specific trabecular and solid models of the facet bone were then discretised into finite element meshes using ScanFE v3.1.4 (Simpleware Ltd, Exeter, UK) software to generate a mixed

mesh of eight-node linear hexahedral brick elements (C3D8) and four-node linear tetrahedral elements (C3D4) as shown in Figure 6.3b and Figure 6.4b.

In both models, boundary and interface conditions were applied such that the bottom nodes of the bone were constrained in all directions to prevent any movement during the simulation. The spherical indenter was only permitted to move in a vertical direction and the horizontal direction and rotational movements were constrained. The contact between top surface of the bone and the indenter surface was represented using frictionless small sliding contact. The Poisson's ratio of the bone was assumed to be 0.3 (Shirazi and Shirazi-Adl, 2009).

a.   b.
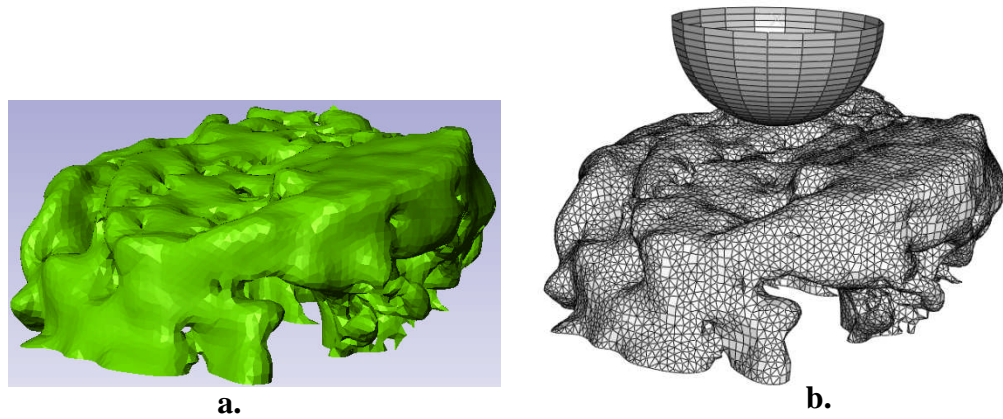
Figure 6.3. Development of the specimen-specific trabecular model a. 3D solid model, b. FE model.

a.   b.
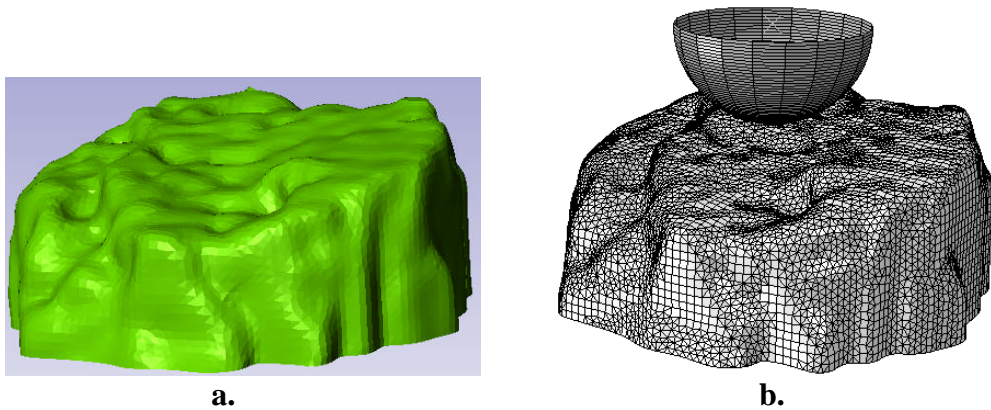
Figure 6.4. Development of the specimen-specific solid model a. 3D solid model, b. FE model.

6.2.5.2 Estimation of the Bone Elastic Modulus

In order to estimate the elastic modulus of the bone tissue (E_{bone}) and the composite elastic modulus ($E_{composite(3D\ solid)}$), the modulus was manually adjusted in the elastic specimen-specific trabecular and solid models respectively until the predicted displacements matched the equilibrium displacements measured from the compression tests of the facet pins. From the estimated tissue elastic modulus of the bone (E_{bone}), the facet bone composite elastic modulus ($E_{composite(3D\ trabecular)}$) was also approximately calculated by incorporating the percentage of the bone volume (V_{bone}) and the fluid modulus as shown below.

$$E_{composite(3D\ trabecular)} \approx (E_{bone} \times \%V_{bone}) + (E_{fluid} \times \%V_{fluid})$$

In this study, the elastic modulus of the fluid (E_{fluid}) was assumed to be negligible because the fluid was expected to freely flow out from the facet pin during the compression test. The composite elastic modulus derived from the specimen-specific trabecular and solid models was then compared to the composite elastic modulus characterised using the biphasic poroelastic axisymmetric model.

6.2.6 Computational Study of the Effect of Trabecular Bone Architecture to the Cartilage Deformation

In the healthy ovine facet joint, the deformation of the subchondral bone was minimal and did not affect the creep compression tests performed on the specimen, as shown in Section 5.2.3. Furthermore, from the computational model sensitivity study, the presence of the subchondral bone did not make any significant change to the cartilage deformation, and there was little change in the outcome until a very low elastic modulus was applied to the bone as demonstrated in Section 5.4.3. However this scenario could not be applied to the human weak bone because, from the experiment results obtained in Section 6.3.1, the subchondral bone deformed even under a low load of 0.24 N during the creep compression test. Previous studies have reported that there are two factors influencing the mechanical properties of the cancellous bone, which are the trabecular architecture and the trabecular material

properties (Goldstein *et al.*, 1993, van Rietbergen *et al.*, 1995). Therefore, these two factors were analysed to observe their influence on the cartilage deformation.

Although virtually no cartilage was detected on both specimens, an artificial cartilage layer with the averaged thickness of 0.6 mm (Yoganandan *et al.*, 2003) was constructed manually in the specimen-specific models using the paint operation tool in ScanIP v3.2 (Simpleware Ltd, Exeter, UK) software. Again, two models were generated representing the subchondral bone as either a solid continuum ('solid model') or including the trabecular architecture ('trabecular model') for comparison of the cartilage deformation, as shown in Figure 6.5. The solid bone was again created manually using the paint operation tool in the ScanIP software to fill the spaces in the trabecular bone in the specimen-specific model.

a. **b.**
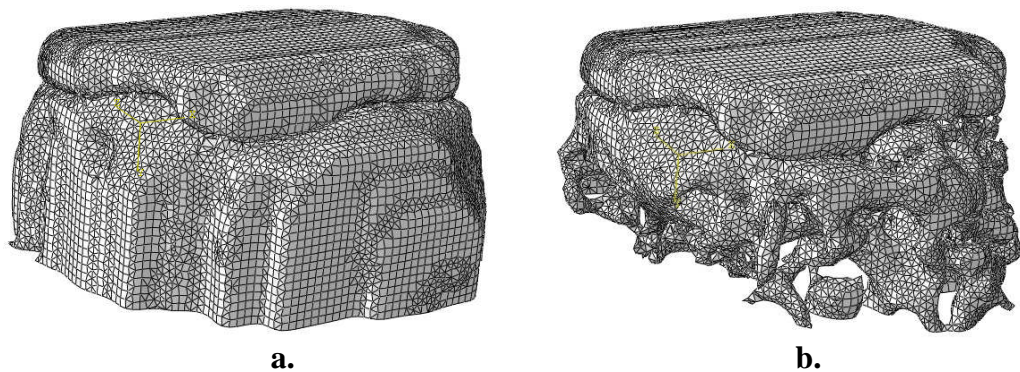
Figure 6.5. FE models a. Solid subchondral bone, b. Trabecular architecture bone.

The cartilage and subchondral bone were modelled as elastic materials in order to reduce the computational time in particular for the cartilage. For the cartilage, the elastic modulus was 0.76 MPa and the Poisson's ratio was 0.08 (Athanasiou *et al.*, 1991). For the subchondral bone, a Poisson's ratio of 0.3 (Shirazi and Shirazi-Adl, 2009) was applied and the composite modulus and bone tissue modulus derived from the compression tests were applied to the solid model and trabecular model respectively. The subchondral bone elastic modulus was also varied between 1000 MPa to 10 MPa in both the solid and trabecular models to evaluate the effect. The selection of the lowest elastic modulus of 10 MPa for the subchondral bone was based on an experimental study which has reported that the compressive modulus of the trabecular bone extracted in anterior-posterior and medial-lateral directions from

human vertebral body aged between 63 to 80 years old was between 7.2 MPa to 48.8 MPa (Ladd *et al.*, 1998).

6.3 Results

6.3.1 Creep Compression Test

The creep compression tests using an indenter were performed on two facet pins (*n=2*) extracted from the human facet joint. The test provided the deformation data of the facet pin which was used to characterise the biphasic properties of the tissue. Figure 6.6 shows an example of the creep compression test result.
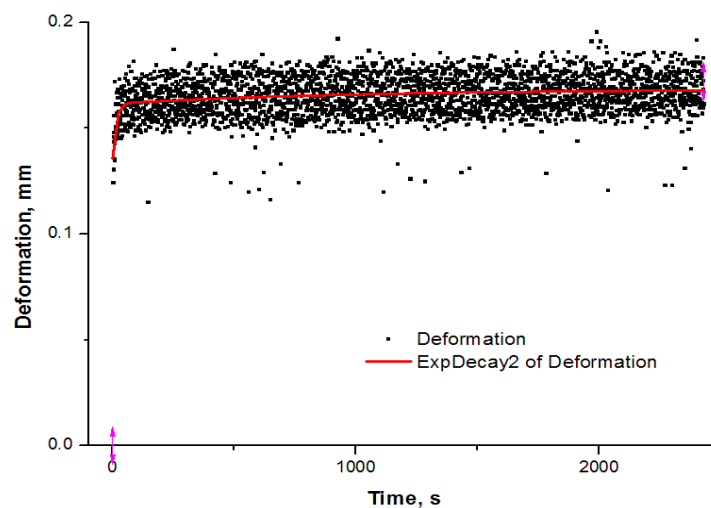
Figure 6.6. Deformation of the facet pin in creep compression test for Specimen 1.

In the previous creep compression test performed on the ovine subchondral bone, no deformation was detected on the bone. However for the human specimens, both of the facet pins were found to deform under the same load of 0.24 N, due to the weak condition of the bone.

6.3.2 Characterisation of Biphasic Properties using Axisymmetric Model

Using the axisymmetric model described in Section 6.2.4, the derived biphasic properties of the two human facet pins ($n=2$) are given in Table 6.1. The elastic modulus and permeability obtained for both of the facet pins were in a similar range.

Table 6.1. The characterised biphasic properties for the human facet pins.
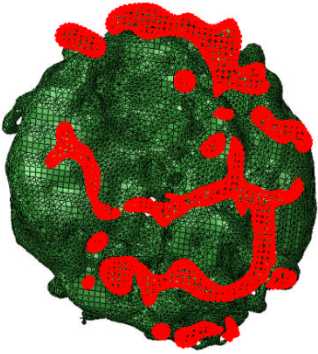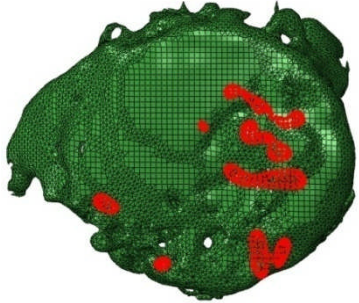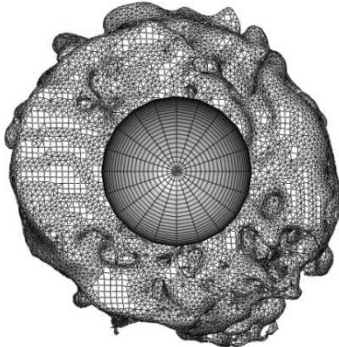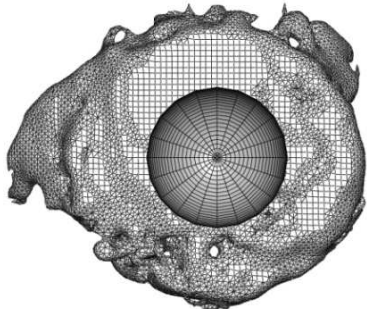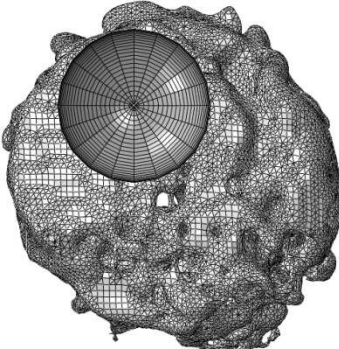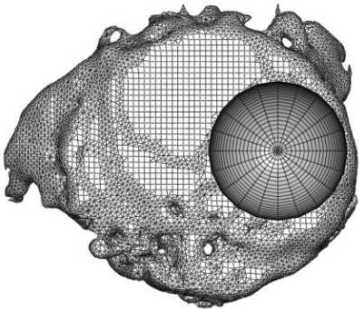
Specimen	Void Ratio	Elastic Modulus $E_{composite(axi)}$, MPa	Permeability,$\times10^{-15}$ m^4/Ns
1	3.3 (66% fluid)	1.90	1.00
2	3.8 (76% fluid)	1.52	1.41

6.3.3 Characterisation of Elastic Modulus of the Facet Subchondral Bone using Specimen-Specific Model

In order to characterise the elastic modulus of the facet subchondral bone, the elastic modulus was manually adjusted to match the experimental displacement using the elastic specimen-specific trabecular and solid models. Table 6.2 shows the estimated elastic modulus of the bone (E_{bone}) obtained from the specimen-specific trabecular models for the two facet bone ($n=2$) specimens. As can be seen from Table 6.2 for the centred indenter, the elastic modulus of the bone (E_{bone}) obtained for Specimen 2 was higher than for Specimen 1. This was likely to be due to the lower number of the nodes constrained at the bottom of the bone due to the uneven trabecular structure on this surface, as well as the thinner trabeculae in this specimen. The models were reanalysed with the indenter offset to the low and high densities of the constrained nodes to clarify that the number of the constrained nodes influenced the estimated elastic modulus. As expected, when the contact point was moved to a region of fewer node constraints, a higher bone tissue elastic modulus was found and vice versa.

In contrast, the constrained nodes did not cause an effect with the solid specific-specimen model since the model was fully constrained across the bottom surface of the bone. The composite elastic modulus values ($E_{composite(3D\ solid)}$) estimated were found to be similar, with values of 1.7 MPa and 1.8 MPa for Specimen 1 and Specimen 2 respectively.

Table 6.2. The elastic modulus of the subchondral bone using specimen-specific model.

	Specimen 1	Specimen 2
Constraint Nodes		
Centre	E_{bone} = 6.9 MPa	E_{bone} = 31.8 MPa
Offset	E_{bone} = 19.3 MPa	E_{bone} = 18.7 MPa

6.3.4 The Effect of Trabecular Architecture to the Cartilage Deformation

Figure 6.7 shows the deformation of the cartilage using various elastic modulus values for the solid and trabecular architecture subchondral bone models.

When the elastic modulus of the bone tissue (E_{bone}) and the composite elastic modulus ($E_{composite(3D\ solid)}$), which were estimated in Section 6.3.3, were applied to the trabecular bone model and solid bone model respectively, there was

approximately 20% difference in the cartilage deformation, as shown in Figure 6.7. This indicates that the trabecular architecture of the facet joint bone plays a role in the cartilage deformation.

When the subchondral bone modulus values were varied between 1000 MPa and 10 MPa, approximately 5% difference in the cartilage deformation was found from the solid specimen-specific model. However for the trabecular architecture bone model, the cartilage deformation started to change at a bone elastic modulus of 100 MPa. These clearly shows that the elastic modulus and the trabecular bone architecture of the subchondral bone influenced the deformation of the cartilage. The difference in the cartilage deformation when the elastic modulus of the bone was applied to the trabecular architecture model between 1000 MPa and 10 MPa was 37%. Figure 6.8 and Figure 6.9 show the comparisons of the cartilage deformation contour plot generated from the solid and trabecular subchondral bone models using different values of elastic modulus of the bone.
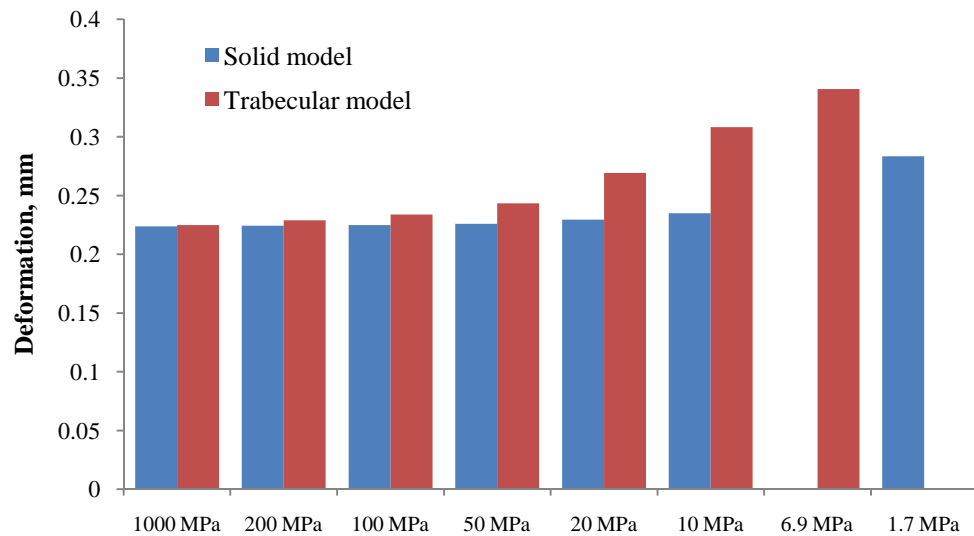
Figure 6.7. Comparison of the cartilage deformation generated from solid and trabecular architecture subchondral bone models at various elastic modulus of the bone.
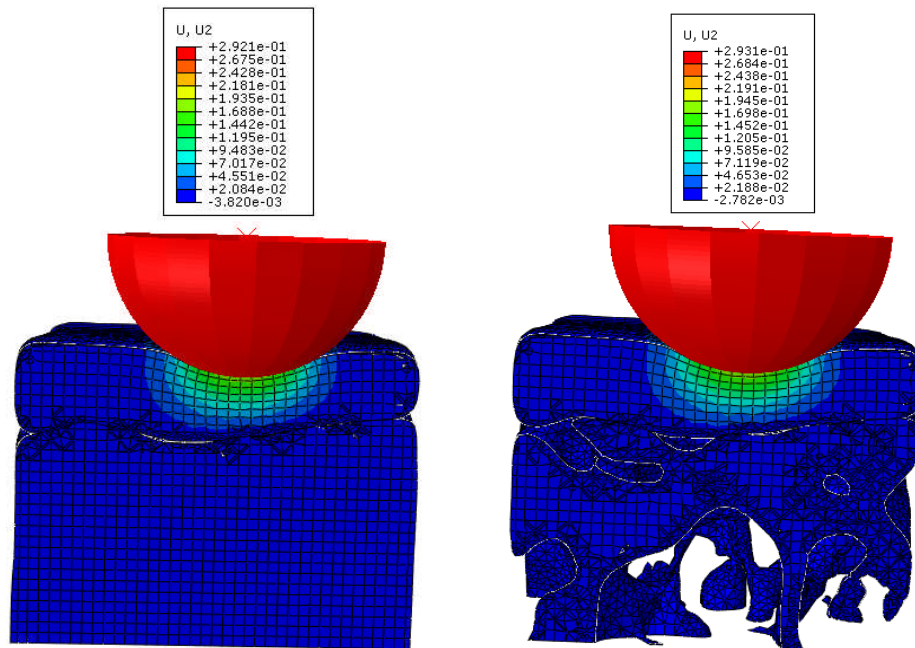
Figure 6.8. Comparison of the cartilage axial deformation contour plot generated from solid and trabecular subchondral bone models using the elastic modulus of subchondral bone value of 1000 MPa subjected to 0.24 N.
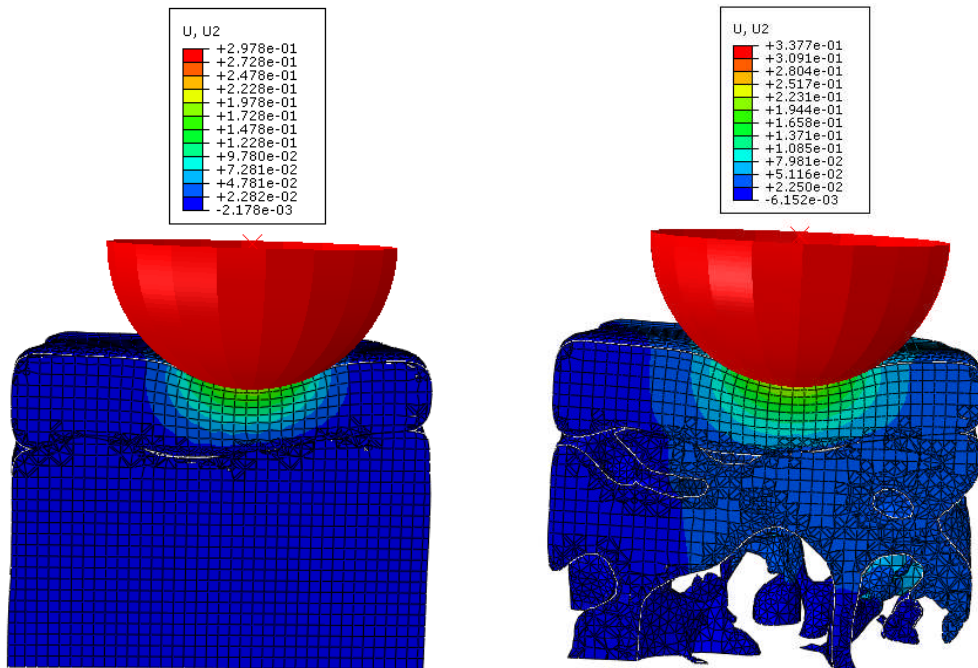
Figure 6.9. Comparison of the cartilage axial deformation contour plot generated from solid and trabecular subchondral bone models using the elastic modulus of subchondral bone value of 20 MPa subjected to 0.24 N.

6.4 Discussion

In this study, the properties of the human facet pin were characterised using the combination of experimental and computational methods. Although the cartilage on the facet pins was totally degenerated, and could not be differentiated from the bone, the study was carried out to characterise the facet subchondral bone properties including the biphasic properties of the facet pin and also the elastic modulus of the bone tissue.

A lot of difficulties were experienced in the extraction of the facet pins, and only two pins were managed to be plugged out from the six facet joints. This was because of the tools used to extract the facet pin from the ovine specimens (Figure 3.1), were insufficient to extract the pin from the weak bone. The corer was fabricated to have rough cutting teeth with a thickness of 0.6 mm, as shown in Figure 6.10, and these may have damaged the architecture of the trabecular bone. In a previous study of bone taken from older cadavers, with an average age of 70 years, a numerically controlled milling machine was used to prepare cubic samples of trabecular bone taken from the vertebral body in order to preserve the architecture of the trabecular bone (Ladd *et al.*, 1998). However, this method would not be suitable for the facet joint because of the small size and curvature shape of the facet articular structures. Therefore, an improved corer with finer cutting teeth using a thinner thickness of stainless steel would be a better option for future studies to avoid damaging the trabecular architecture and enhance the extraction process for the weak bone.
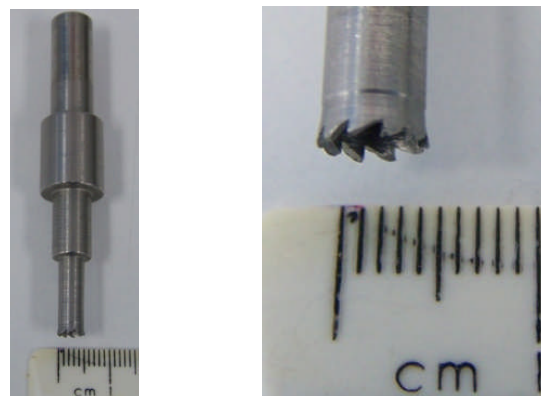
Figure 6.10. The corer used to extract the facet pin.
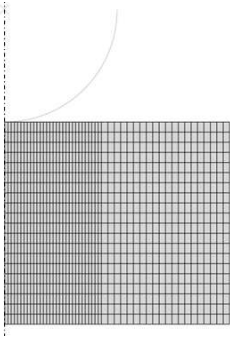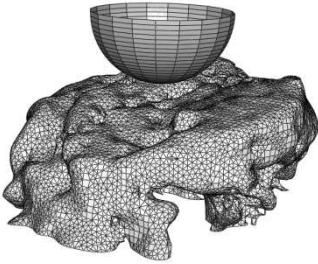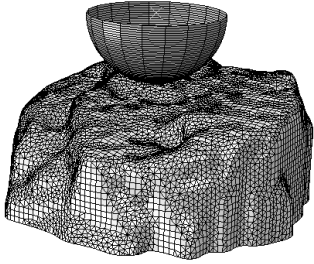
To date, no studies appear to have characterised the elastic modulus of the facet subchondral bone, so there is no previous data to compare with the present results. However, an experimental study has been carried out to determine the composite compressive modulus of the trabecular bone extracted in different directions from the vertebral body of specimens aged between 63 to 80 years old (Ladd *et al.*, 1998). The compression moduli ranged between 11.9 MPa and 48.8 MPa in anterior-posterior direction, while in medial-lateral direction the moduli ranged between 7.2 MPa and 19.1 MPa. Compared to the present estimated composite elastic modulus values of 1.7 MPa and 1.8 MPa, both of the moduli were slightly lower than the experimental values. This could be due to the weak condition of the bone as shown in Figure 6.1.

From the estimated elastic modulus of the bone (E_{bone}) using the elastic specimen-specific model and the volume of the bone (V_{bone}), the composite elastic modulus ($E_{composite(3D\ trabecular)}$) of the facet pin was calculated. Table 6.3 shows these estimated values compared to the composite elastic modulus derived from the biphasic poroelastic axisymmetric model ($E_{composite(axi)}$) and the composite elastic modulus derived from the specimen-specific solid model ($E_{composite(3D\ solid)}$).

Compared with the composite elastic modulus of the bone derived using the solid specimen-specific model, the values derived using the axisymmetric biphasic model were similar, as shown in Table 6.3.

There was some difference between these values and the estimated composite elastic modulus calculated from the specimen-specific trabecular model, even though all of the elastic modulus values were of a similar magnitude. Approximately 24% difference was found for Specimen 1 and a five-fold difference for Specimen 2. This indicates that the trabecular bone model in this case is not an appropriate model to predict the composite modulus or apparent modulus because the model was dependant on the amount of the nodes constrained at the bottom of the bone and the location of the contact point as demonstrated in Table 6.2.

Table 6.3. Comparison of the composite elastic modulus for the facet pin characterised using axisymmetric biphasic model, linear specimen-specific model and linear solid specimen-specific model.

$E_{composite(axi)}$	$E_{composite(3D\ trabecular)}$	$E_{composite(3D\ solid)}$
Method Derived from axisymmetric biphasic poroelastic model to fit compression test data.	**Method** E_{bone} derived from 3D linear trabecular model and then calculated from $E_{composite(3D\ trabecular)} \approx (E_{bone} \times \%V_{bone}) + (E_{fluid} \times \%V_{fluid})$, where $E_{fluid} = 0$.	**Method** Derived from 3D linear solid model to fit compression test data.
Specimen 1 = 1.90 MPa Specimen 2 = 1.52 MPa	Specimen 1 = 2.35 MPa Specimen 2 = 7.63 MPa	Specimen 1 = 1.7 MPa Specimen 2 = 1.8 MPa

Furthermore, bone quality plays an important role in the deformation of the subchondral bone as demonstrated in the present experimental studies on ovine subchondral bone (Section 5.2.3) and weak human subchondral bone (Section 6.3.1). Although the indenter was assumed to be in the centre of the specimen-specific model, the actual contact location in the experiment could not be very accurately located. In addition, actual contact between the lower surface of the bone and the base could not be fully controlled. These uncertainties in the experiment could be attributable for the error in the properties derived from the specimen-specific model.

Further computational study was carried out to examine whether the trabecular architecture affected the cartilage deformation. It was found that the cartilage deformation generated from the trabecular bone models started to increase substantially (Figure 6.7) when the elastic modulus of the bone value of 100 MPa was applied. Moreover, it was demonstrated that the architecture of the trabecular

bone has an important role, as shown by the difference between the trabecular model and the solid bone model, described in Section 6.3.4. Therefore, in order to characterise the properties of the cartilage with weak subchondral bone, the elastic modulus and the trabecular architecture of the subchondral bone must be considered.

In addition, the permeability of the subchondral bone derived using the axisymmetric biphasic poroelastic model were 1.00 and 1.41 $\times 10^{-15}$ m^4/Ns which were two orders of magnitude different compared to the experimental characterisation on mature bone of 3.7 $\times 10^{-13}$ m^4/Ns (Grimm and Williams, 1997, Nauman *et al.*, 1999, Isaksson *et al.*, 2009). Although the computational methodology has the potential to derive the permeability of the bone, a thorough study of this experiment methodology of the compression test using an indenter of the bone must be reviewed.

The limitation of this study was the number of the facet pins tested experimentally. Only two specimens were characterised which was insufficient to determine the variability in the results. However, the application of the specimen-specific model could be a potential method of characterising the cartilage properties. This is because the model could replicate the curvature of the articular cartilage surface and the trabecular bone architecture of the subchondral bone, which this study has shown to influence the predicted deformation of the cartilage. Without these factors, there is likely to be considerable error in the characterisation of the cartilage properties. Furthermore, this methodology could be applied for assessing the cartilage properties for different subchondral bone conditions.

Chapter 7: General Discussion and Conclusions

7.1 Introduction

The work presented in this thesis aimed to characterise the anatomical and biomechanical behaviour of the spinal facet joints and develop computational methods to determine the cartilage biphasic properties. Throughout the development process, investigation of the ovine spine was carried out to evaluate the use of an ovine facet joint model as a representation of the human facet joint. A methodology, which consisted of experimental and computational methods, was developed in order to characterise the biomechanical properties of the articular cartilage for the facet joints. This chapter presents the overall discussion of the work presented in Chapters 4, 5 and 6, the potential applications and future works. This discussion is followed with the overall conclusions of the study.

7.2 Overall Discussion

This study has provided further insight into the complex morphology of the spinal facet joint for better understanding of its behaviour. A comprehensive set of data on the facet articular radius and facet orientation angle of the ovine spine was established using an improved measurement method based on the µCT scan images. The qualitative similarities of the facet joint morphology between the ovine and human spines indicates that the ovine spine could potentially be used to represent the human spine to study the facet joint during spine motion since a similar range of motion was found in an experimental study between these two species (Wilke *et al.*, 1997a).

In the present study, a positive relationship between the facet orientation angle and axial rotation was obtained for both ovine and human vertebral segments,

although Ahmed *et al.* (1990) stated otherwise. Experimental studies have shown that the mechanical function of the facet joint during axial rotation is to limit and prevent excessive movement from damaging the intervertebral disc (Adams and Hutton, 1981, Adams and Hutton, 1983, Stokes, 1988). In addition, the facet orientation angle has been shown to be an important parameter because it has been associated with the low back pain related diseases such as lumbar facet joint osteoarthritis, disc degeneration, disc herniation and degenerative spondylolisthesis (Boden *et al.*, 1996, Fujiwara *et al.*, 2001, Kalichman *et al.*, 2009).

Clinically, low back pain patients are examined using imaging methods such as plain radiography, computed tomography (CT) and magnetic resonance imaging (MRI), after potentially serious conditions have been found in the patient history and from physical examination (Chou *et al.*, 2007). In the imaging diagnosis, the facet joints are evaluated based on the scan images with regard to joint space narrowing, sclerosis, subchondral erosions, cysts and osteophytes (Schwarzer *et al.*, 1995). Therefore, the facet orientation angle could provide an additional potential evaluation measurement in the imaging diagnostic for the low back pain patients. However, further studies are needed in order to implement the measurement of facet angle from medical scan images and assess the effectiveness of incorporating the facet orientation angle parameter into the diagnosis of low back pain patients.

Although facet joint artificial implants have been introduced to treat facet joint related diseases (Wiseman *et al.*, 2005, Goel *et al.*, 2007, Zhu *et al.*, 2007, Regan *et al.*, 2009), these have yet to prove their long term success, and cartilage tissue engineering appears to be a promising approach for facet joint cartilage regeneration. In order to establish the design criteria for tissue engineered materials, the characterisation of the native cartilage biomechanical properties is required so that the desired functional properties of the engineered tissue are known. In this study, the biomechanical properties of the articular cartilage of the ovine facet joint were determined for the first time to obtain the cartilage thickness, equilibrium biphasic elastic modulus and permeability as described in Chapter 5. A methodology which consists of experimental and computational methods, was developed to characterise the properties using an axisymmetric biphasic poroelastic FE model to match the cartilage deformation that was generated from the compression test using an indenter. The derived properties were found to be within the range of the human

cartilage properties characterised from other synovial joints in the human body. In addition, a freeze-thaw cycle of the intact facet joints was found to be a potential storage method for cartilage and facet joint biomechanical research, since the biphasic properties of the cartilage pins extracted from the intact facet joints were comparable to the fresh cartilage specimens. Based on these characterisation results, including the similarities found in the morphology, range of motion, and cartilage properties, the ovine spine appears to be a good model to represent human spine in biomechanical facet joint studies.

However, the axisymmetric model used to characterise the properties was seen to include some error in the estimated cartilage properties since it failed to represent the actual curvature of the cartilage surface. Therefore, a novel specimen-specific model was developed to simulate the compression test of the cartilage pin specimen in order to characterise the biphasic properties of the cartilage. This model incorporated the actual curvature of the cartilage surface and the trabecular bone architecture of the subchondral bone. The difference in the characterised cartilage properties between the specimen-specific model and the axisymmetric model was 35% for the permeability and 13% for the elastic modulus, and moreover the derived properties were found to vary depending on the radius of the cartilage curvature. This is in agreement with a computational study carried out by Holzapfel and Stadler (2006), which reported that the facet curvature was crucial in the contact stress distribution and played an important role in the load-bearing characteristics study. At this stage, it is not known at which level of curvature the specimen-specific modelling becomes necessary, and further investigation is required. However from the axisymmetric model shown in Section 5.4.5, the derived biphasic properties were affected when the cartilage surface radius of 40 mm was applied and became more severe when the radius was decreased.

Although encouraging results were obtained using the specimen-specific model, a few issues were observed during the development and simulation of the model which limited the study in this thesis. The Abaqus 6.9-1 (DS Simulia Corp., Providence, RI, USA) software only provided an eight-node pore pressure element in order to model the cartilage. However, it was not possible to create hexahedral element meshes either in Abaqus 6.9-1 (DS Simulia Corp., Providence, RI, USA) or ScanFE v3.1.4 (Simpleware Ltd, Exeter, UK) software. Therefore, the IA-FEMesh

(University of Iowa, IA, USA) software was used to generate the hexahedral mesh but severe elemental distortions were found at the curved edge of the cartilage which led to the necessity to reshape the model to a smaller cuboid specimen-specific section. In future, the SCIRun (University of Utah, UT, USA) software could be explored as it has shown the potential to generate smooth hexahedral mesh (Shepherd and Johnson, 2009) or other hexahedral mesh generation methods that have been published (Marechal, 2009, Tabacu *et al.*, 2010).

Another important issue was the substantial computational time taken using the specimen-specific model. Due to this issue, no mesh sensitivity study was undertaken since re-meshing the model with different numbers of elements would have been extremely time consuming. Instead, the width and height of the element was chosen to approximately match that used in the axisymmetric model which was proven to produce very similar results to the idealised three-dimensional model as demonstrated in Section 3.7.2. The computational time issue also affected the characterisation of the cartilage biphasic properties using the specimen-specific model, where ideally the properties in the specimen-specific model would have been iteratively changed until the predicted deformation matched the experimental results. Instead, the axisymmetric model was used to reiterate the properties in the simulation to match the results generated from the specimen-specific model experimental data in order to avoid the excessive amount of computational time taken as described in Section 5.4.6. Despite these issues, promising results were obtained using the specimen-specific model and the cartilage characterisation methodology was then implemented in a study of the human facet joint.

In addition to the difficulty in obtaining normal cartilage from the human specimens, other related problems included the large variation in geometry and mechanical properties due to differences in age, bone quality, and disc degenerative changes. The characterisation of the cartilage from human facet joints would provide useful information as the data has yet to be published, however in the present study, the cartilage acquired from the human facet joint was totally degenerated and it was not possible to characterise the properties. Instead, an artificial cartilage layer was created in the specimen-specific model to observe the effect of the trabecular bone architecture on the cartilage deformation in the creep-compression test simulation. It was found that it is important to preserve the architecture of the trabecular bone and

to apply the correct elastic modulus of the subchondral bone because these factors affected the cartilage deformation and could be more crucial for the weak bone. It has been shown in this study that the cartilage deformation generated from the trabecular bone models started to increase substantially (Figure 6.7) when the elastic modulus of the bone value of 100 MPa was applied. However, further investigation is required to relate the elastic modulus of the bone and the level of porosity of the bone.

Although promising results were obtained using the Abaqus 6.9-1 (DS Simulia Corp., Providence, RI, USA) software, it would also be beneficial to explore an alternative software which geared toward the biological applications. The FEBio (University of Utah, UT, USA) software which has been specifically written for biological problems in computational biomechanics has shown the potential of generating similar results compared to Abaqus software (Maas *et al.*, 2009). In addition, the present study only modelled the contact interaction between the cartilage surface and the impermeable indenter surface. The next step is to model the contact between the cartilage surfaces (Pawaskar, 2010). This could lead to the modelling of the whole facet joint and finally for more complex model of the vertebral segment with complete detail of facet joint.

7.3 Conclusions

In the spinal research field, animal models have often been used due to the difficulties in obtaining human spines and moreover, the large variation in the biomechanical properties of the human specimens. The ovine spine appears to be a good model to represent the human spine in facet joint studies based on the following facts: the morphology similarities between these two species, as presented in Chapter 4; the biomechanical properties of the articular cartilage of the ovine facet joint being within the range of human cartilage properties, as described in Chapter 5; and the similar ranges of motion in all directions which were observed in an experimental study published previously (Wilke *et al.*, 1997a).

A successful methodology was achieved to characterise the cartilage biomechanical properties of the facet joint using the experimental and computational

methods. However, the assumption that the cartilage pin specimen has a flat surface in the axisymmetric FE model will limit the accuracy of the derived cartilage properties. A novel specimen-specific FE model was developed to replicate the actual curvature of the cartilage surface and subsequently derive the cartilage biphasic properties. In this study, the difference in the characterised cartilage properties determined using the specimen-specific model compared to the flat axisymmetric model were found to be 35% for the permeability and 13% for the elastic modulus, and these may vary depending on the radius of the cartilage surface.

Furthermore, the specimen-specific model was able to model the trabecular bone architecture of the subchondral bone. Results from a pilot computational study on human facet joint specimens show that the elastic modulus and trabecular architecture of the subchondral bone affected the cartilage deformation in a compression test and therefore will influence the characteristic biphasic properties of the cartilage.

This novel approach of using the specimen-specific model to characterise the cartilage biomechanical properties has provided new prospects for future work in cartilage research since the model incorporated the cartilage surface curvature and the trabecular architecture of the subchondral bone, which were observed to be important aspects in the cartilage properties characterisation. This methodology could potentially be used to characterise the cartilage of the facet joint for other species and the cartilage from other synovial joints. Furthermore, the characterisation of the cartilage biomechanical properties could be performed under various subchondral bone conditions including the osteoporotic bone.

References

Adam, C., Eckstein, F., Milz, S. & Putz, R. (1998) The Distribution of Cartilage Thickness within the Joints of the Lower Limb of Elderly Individuals. *Journal of Anatomy,* 198**,** 203-214.

Adams, M. A., Bogduk, N., Burton, K. & Dolan, P. (2002) *The Biomechanics of Back Pain,* Edinburgh, Churchill Livingstone.

Adams, M. A. & Hutton, W. C. (1980) The Effect of Posture on the Role of the apophysial joints in resisting intervertebral compressive forces. *Journal of Bone Joint and Surgery- British Volume,* 62**,** 353-357.

Adams, M. A. & Hutton, W. C. (1981) The Relevance of Torsion to the Mechanical Derangement of the Lumbar Spine. *Spine,* 6**,** 241-248.

Adams, M. A. & Hutton, W. C. (1983) The Mechanical Function of the Lumbar Apophyseal Joints. *Spine,* 8**,** 327-330.

Ahlgren, B. D., Vasavada, A., Brower, R. S., Lydon, C., Herkowitz, H. N. & Panjabi, M. M. (1994) Anular Incision Technique on the Strength and Multidirectional Flexibility of the Healing Intervertebral Disc. *Spine,* 19**,** 948-954.

Ahmed, A. M., Duncan, N. A. & Burke, D. L. (1990) The Effect of Facet Geometry on the Axial Torque- Rotation Response of Lumbar Motion Segments. *Spine,* 15**,** 391-401.

Akizuki, S., Mow, V. C., Muller, F., Pita, J. C., Howell, D. S. & Manicourt, D. H. (1986) Tensile Properties of Human Knee Joint Cartilage: Influence of Ionic Conditions, Weight Bearing, and Fibrillation on the Tensile Modulus. *Journal of Orthopaedic Research,* 4**,** 379-392.

Allan, D. G., Russell, G. G., Moreau, M. J., Raso, V. J. & Budney, D. (1990) Vertebral End-Plate Failure in Porcine and Bovine Model of Spinal Fracture Instrumentation. *Journal of Orthopaedic Research,* 8**,** 154-156.

An, Y. H. & Martin, K. L. (Eds.) (2003) *Handbook of Histology Methods for Bone and Cartilage,* New Jersey, Humana Press Inc.

Anderson, A. E., Ellis, B. J., Maas, S. A., Peters, C. L. & Weiss, J. A. (2008) Validation of Finite Element Predictions of Cartilage Contact Pressure in the Human Hip Joint. *Journal of Biomechanical Engineering,* 130**,** 051008.

Anderson, D. D., Goldsworthy, J. K., Li, W., Rudert, M. J., Tochigi, Y. & Brown, T. D. (2007) Physical Validation of a Patient-Specific Contact Finite Element Model of the Ankle. *Journal of Biomechanics,* 40**,** 1662-1669.

Andersson, G. B. J., Lucente, T., Davis, A. M., Kappler, R. E., Lipton, J. A. & Leurgans, S. (1999) A Comparison of Osteophatic Spinal Manipulation with Standard Care for Patients with Low Back Pain. *The New England Journal of Medicine,* 341**,** 1426-1431.

Armstrong, C. G. & Gardner, D. L. (1977) Thickness and Distribution of Human Femoral Head Articular Cartilage: Changes with Age. *Annals of the Rheumatic Diseases,* 36**,** 407-412.

Arnoldi, C. C., Brodsky, A. E., Cauchoix, J., Crock, H. V., Dommisse, G. F. & Edgar, M. A. (1976) Lumbar Spinal Stenosis and Nerve Root Entrapment Syndromes. *Clinical Orthopaedics and Related Research,* 115**,** 4-5.

Ateshian, G. A., Soslowsky, L. J. & Mow, V. C. (1991) Quantitation of Articular Surface Topography and Cartilage Thickness in Knee Joints Using Stereophotogrammetry. *Journal of Biomechanics,* 24**,** 761-776.

Athanasiou, K. A., Liu, G. T., Lavery, L. A., Lanctot, D. R. & Schenck, R. C. (1998) Biomechanical Topography of Human Articular Cartilage in the First Metatarsophalangeal Joint. *Clinical Orthopaedics and Related Research***,** 269-281.

Athanasiou, K. A., Rosenwasser, M. P., Buckwalter, J. A., Malinin, T. I. & Mow, V. C. (1991) Interspecies Comparisons of In Situ Intrinsic Mechanical Properties of Distal Femoral Cartilage. *Journal of Orthopaedic Research,* 9**,** 330-340.

Atkinson, P. J., Newberry, W. N., Atkinson, T. S. & Haut, R. C. (1998) A Method to Increase the Sensitive Range of Pressure Sensitive Film. *Journal of Biomechanics,* 31**,** 855-859.

Black, J., Shadle, C. A., Parsons, J. S. & Brighton, C. T. (1979) Articular Cartilage Preservation and Storage: Application of Tissue Culture Techniques to the Storage of Viable Articular Cartilage. *Arthritis and Rheumatism,* 22**,** 1102-1108.

Boden, S. D., Riew, K. D., Yamaguchi, K., Branch, T. P., Schellinger, D. & Wiesel, S. W. (1996) Orientation of the Lumbar Facet Joints: Association with Degenerative Disc Disease. *Journal of Bone and Joint Surgery-American Volume,* 78**,** 403-411.

Bogduk, N. (2005) *Clinical Anatomy of the Lumbar Spine and Sacrum,* Elsevier Churchill Livingstone.

Breau, C., Shirazi-Adl, A. & De Guise, J. (1991) Reconstruction of a Human Ligamentous Lumbar Spine Using CT Images- A Three-Dimensional Finite Element Mesh Generation. *Annals of Biomedical Engineering,* 19**,** 291-302.

Brekelmans, W. A. M., Poort, H. W. & Slooff, T. J. (1972) A New Method to Analyse the Mechanical Behaviour of Skeletal Parts. *Acta Orthopaedica Scandinavica,* 43**,** 301-317.

Brighton, C. T., Shadle, C. A., Jimenez, S. A., Irwin, J. T., Lane, J. M. & Lipton, M. (1979) Articular Cartilage Preservation and Storage: Application of Tissue Culture Techniques to the Storage of Viable Articular Cartilage. *Arthritis and Rheumatism,* 22**,** 1093-1101.

Brown, T. D., Anderson, D. D., Nepola, J. V., Singerman, R. J., Pedersen, D. R. & Brand, R. A. (1988) Contact Stress Aberrations Following Imprecise Reduction of Simple Tibial Plateau Fractures. *Journal of Orthopaedic Research,* 6**,** 851-862.

Burstein, D., Bashir, A. & Gray, M. L. (2000) MRI Techniques in Early Stages of Cartilage Disease. *Investigative Radiology,* 35**,** 622-638.

Busscher, I., Van Der Veen, A. J., Van Dieen, J. H., Kingma, I., Verkerke, G. J. & Veldhuizen, A. G. (2010) In Vitro Biomechanical Characteristics of the Spine: A Comparison Between Human and Procine Spinal Segments. *Spine,* 35**,** E35-E42.

Buttermann, G. R., Schendel, M. J., Kahmann, R. D., Lewis, J. L. & Bradford, D. S. (1992) In Vivo Facet Joint Loading of the Canine Lumbar Spine. *Spine,* 17**,** 81-92.

Carrera, G. F., Haughton, V. M., Syvertsen, A. & Williams, A. L. (1980) Computed Tomography of the Facet Joints. *Radiology,* 134**,** 145-148.

Cassidy, J. J., Hiltner, A. & Baer, E. (1989) Hierarchical Structure of the Intervertebral Disc. *Connective Tissue Research,* 23**,** 75-88.

Cavanaugh, J. M., Ozaktay, A. C., Yamashita, H. T. & King, A. I. (1996) Lumbar Facet Pain: Biomechanics, Neuroanatomy and Neurophysiology. *Journal of Biomechanics,* 29**,** 1117-1129.

Chan, T. F. & Vese, L. A. (2001) Active Contours Without Edges. *IEEE Transactions on Image Processing,* 10**,** 266-277.

Choi, A. P. & Zheng, Y. P. (2005) Estimation of Young's Modulus and Poisson's Ratio of Soft Tissue from Indentation Using Two Different-Sized Indentors: Finite Element Analysis of the Finite Deformation Effect. *Medical & Biological Engineering & Computing,* 43**,** 258-264.

Chou, R., Qaseem, A., Snow, V., Casey, D., Cross Jr., J. T., Shekelle, P. & Owens, D. K. (2007) Diagnosis and Treatment of Low Back Pain: A Joint Clinical

Practice Guideline from the American College of Physicians and the American Pain Society. *Annals of Internal Medicine,* 147**,** 478-491.

Clark, A. L., Herzog, W. & Leonard, T. R. (2002) Contact Area and Pressure Distribution in the Feline Patellofemoral Joint UnderPphysiologically Meaningful Loading Conditions. *Journal of Biomechanics,* 35**,** 53-60.

Cohen, S. P. & Raja, S. N. (2007) Pathogenesis, Diagnosis, and Treatment of Lumbar Zygapophysial (Facet) Joint Pain. *Anesthesiology,* 106**,** 591-614.

Cotterill, P. C., Kostuik, J. P., D'angelo, G., Fernie, G. R. & Maki, B. E. (1986) An Anatomical Comparison of the Human and Bovine Thoracolumbar Spine. *Journal of Orthopaedic Research,* 4**,** 298-303.

Cyteval, C., Thomas, E., Picot, M. C., Derieffy, P., Blotman, F. & Taourel, P. (2002) Normal Vertebral Body Dimensions: A New Measurement Method Using MRI. *Osteoporosis International,* 13**,** 468-473.

Dath, R., Ebinesan, A. D., Porter, K. M. & Miles, A. W. (2007) Anatomical Measurements of Porcine Lumbar Vertebrae. *Clinical Biomechanics,* 22**,** 607-613.

Deyo, R. A. & Weinstein, J. N. (2001) Low Back Pain. *The New England Journal of Medicine,* 344**,** 363-370.

Dietrich, M., Kedzior, K. & Zagrajek, T. (1991) A Biomechanical Model of the Human Spinal System. *Proceedings Inst Mech Eng [H]: Journal of Engineering in Medicine,* 205**,** 19-26.

Disilvestro, M. R. & Suh, J. K. (2002) Biphasic Poroviscoelastic Characteristics of Proteoglycan-Depleted Articular Cartilage: Simulation of Degeneration. *Annals of Biomedical Engineering,* 30**,** 792-800.

Dreyer, S. J. & Dreyfuss, P. H. (1996) Low Back Pain and the Zygapophysial (Facet) Joints. *Archives of Physical Medicine Rehabilitation,* 77**,** 290-300.

Dunlop, R. B., Adams, M. A. & Hutton, W. C. (1984) Disc Space Narrowing and the Lumbar Facet Joints. *Journal of Bone and Joint Surgery- British Volume,* 66**,** 706-710.

Eckstein, F., Burstein, D. & Link, T. M. (2006) Quantitative MRI of Cartilage and Bone: Degenerative Changes in Osteoarthritis. *NMR in Biomedicine,* 19**,** 822-854.

Eckstein, F., Schnier, M., Haubner, M., Priebch, J., Glaser, C., Englmeier, K. H. & Reiser, M. (1998) Accuracy of Cartilage Volume and Thickness

Measurements with Magnetic Resonance Imaging. *Clinical Orthopaedics and Related Research,* 352**,** 137-148.

Eckstein, F., Sittek, H., Milz, S., Schulte, E., Kiefer, B., Reiser, M. & Putz, R. (1995) The Potential of Magnetic Resonance Imaging (MRI) for Quantifying Articular Cartilage Thickness - A Methodological Study. *Clinical Biomechanics,* 10**,** 434-440.

Edwards, W. T., Zheng, Y., Ferrara, L. A. & Yuan, H. A. (2001) Structural Features and Thickness of the Vertebral Cortex in the Thoracolumbar Spine. *Spine,* 26**,** 218-225.

Eggli, S., Schlapfer, F., Angst, M., Witschger, P. & Aebi, M. (1992) Biomechanical Testing of Three Newly Developed Transpedicular Multisegmental Fixation Systems. *European Spine Journal,* 1**,** 109-116.

El-Bohy, A. A., Yang, K. H. & King, A. I. (1989) Experimental Verification of Facet Load Transmission by Direct Measurement of Facet Lamina Contact Pressure. *Journal of Biomechanics,* 22**,** 931-941.

El-Khoury, G. Y., Alliman, K. J., Lundberg, H. J., Rudert, M. J., Brown, T. D. & Saltzman, C. L. (2004) Cartilage Thickness in Cadaveric Ankles: Measurement with Double-Contrast Multi–Detector Row CT Arthrography versus MR Imaging. *Radiology,* 233**,** 768-773.

Elder, B. D., Vigneswaran, K., Athanasiou, K. A. & Kim, D. H. (2009) Biomechanical, Biochemical and Histological Characterization of Canine Lumbar Facet Joint Cartilage. *Journal of Neurosurgery: Spine,* 10**,** 623-628.

Elliott, D. M., Narmoneva, D. A. & Setton, L. A. (2002) Direct measurement of the Poisson's ratio of human patella cartilage in tension. *Journal of Biomechanical Engineering,* 124**,** 223-228.

Elmore, S. M., Sokoloff, L., Norris, G. & Carmeci, P. (1963) Nature of "Imperfect" Elasticity of Articular Cartilage. *Journal of Applied Physiology,* 18**,** 393-396.

Eyre, D. R. (1991) The Collagens of Articular Cartilage. *Seminars in Arthritis and Rheumatism,* 21**,** 2-11.

Fagan, M. J., S, J. & Mohsen, A. M. (2002a) Finite Element Analysis in Spine Research. *Proceedings Inst Mech Eng [H]: Journal of Engineering in Medicine,* 216**,** 281-298.

Fagan, M. J., S, J., Siddall, D. J. & Mohsen, A. M. (2002b) Patient-Specific Spine Models. Part 1: Finite Element Analysis of the Lumbar Intervertebral Disc - A Material Sensitivy Study. *Proceedings Inst Mech Eng [H]: Journal of Engineering in Medicine,* 206**,** 299-314.

Farfan, H. F., Huberdeau, R. M. & Dubow, H. I. (1972) Lumbar Intervertebral Disc Degeneration: The Influence of Geometrical Features on the Pattern of disc Degeneration- A Post Mortem Study. *Journal of Bone and Joint Surgery-American Volume,* 54**,** 492-510.

Farndale, R. W., Buttle, D. J. & Barrett, A. J. (1986) Improved Quantitation and Discrimination of Sulphated Glycosaminoglycans by Use of Dimethylmethylene Blue. *Biochimica et Biophysica Acta,* 883**,** 173-177.

Fetter, N. L., Leddy, H. A., Guilak, F. & Nunley, J. A. (2006) Composition and Transport Properties of Human Ankle and Knee Cartilage. *Journal of Orthopaedic Research,* 24**,** 211-219.

Fitzpatrick, C. K., Baldwin, M. A., Ali, A. A., Laz, P. J. & Rullkoetter, P. J. (2011) Comparison of Patellar Bone Strain in the Natural and Implanted Knee during Simulated Deep Flexion *Journal of Orthopaedic Research,* 29**,** 232-239.

Frank, E. H. & Grodzinsky, A. J. (1987) Cartilage Electromechanics: A Continuum Model of Cartilage Electrokinetics and Correlation with Experiments. *Journal of Biomechanics,* 20**,** 629-639.

Franz, T., Hasler, E. M., Hagg, R., Weiler, C., Jakob, R. P. & Mainil-Varlet, P. (2001) In Situ Compressive Stiffness, Biochemical Composition, and Structural Integrity of Articular Cartilage of the Human Knee Joint. *Osteoarthritis and Cartilage,* 9**,** 582-592.

Friedrich, K. M., Nemec, S., Peloschek, P., Pinker, K., Weber, M. & Trattnig, S. (2007) The Prevalence of Lumbar Facet Joint Edema in Patients with Low Back Pain. *Skeletal Radiology,* 36**,** 755-760.

Frymoyer, J. W., Pope, M. H., Clements, J. H., Wilder, D. G., Macpherson, B. & Ashikaga, T. (1983) Risk Factors in Low-Back Pain: An Epidemiological Survey. *Journal of Bone and Joint Surgery- American Volume,* 65**,** 213-218.

Fujiwara, A., Tamai, K., An, H. S., Lim, T. H., Yoshida, H., Kurihashi, A. & Saotome, K. (2001) Orientation and Osteoarthritis of the Lumbar Facet Joint. *Clinical Orthopaedics and Related Research,* 385**,** 88-94.

Fujiwara, A., Tamai, K., Yamato, M., An, H. S., Yoshida, H., Saotome, K. & Kurihashi, A. (1999) The Relationship Between Facet Joint Osteoarthritis and Disc Degeneration of the Lumbar Spine: An MRI Study. *European Spine Journal,* 8**,** 396-401.

Geisser, M. E., Wiggert, E. A., Haig, A. J. & Colwell, M. O. (2005) A Randomized, Controlled Trial of Manual Therapy and Specific Adjuvant Exercise for Chronic Low Back Pain. *Clinical Journal of Pain,* 21**,** 463-470.

Ghormley, R. K. (1933) Low Back Pain - With Special Reference to the Articular Facets, with Presentation of an Operative Procedure. *Journal of American Medical Association,* 101**,** 1773-1777.

Goel, V. K., Goyal, S., Clark, C., Nishiyama, K. & Nye, T. (1985) Kinematics of the Whole Lumbar Spine: Effect of Discectomy. *Spine,* 10**,** 543-554.

Goel, V. K., Mehta, A., Jangra, J., Ahmed, F., Kiapour, A., Hoy, R. W. & Fauth, A. R. (2007) Anatomic Facet Replacement System (AFRS) Restoration of Lumbar Segment Mechanics to Intact: A Finite Element Study and In Vitro Cadaver Investigation. *SAS Journal,* 1**,** 46-54.

Goldsmith, A. A. J., Hayes, A. & Clift, S. E. (1995) Modelling the Response of Biomaterials and Soft, Hydrated Biological Tissues Using Soils Consolidation Theory. *ABAQUS User's Conference.* Paris, France.

Goldstein, S. A., Goulet, R. & Mccubbrey, D. (1993) Measurement and Significance of Three-Dimensional Architecture to the Mechanical Integrity of Trabecular Bone. *Calcified Tissue International,* 53**,** S127-S133.

Goldthwait, J. E. (1911) The Lumbo-Sacral - Articulation - An Explanation of Many Cases of Lumbago, Sciatica and Paraplegia. *Boston Medical and Surgical Journal,* 164**,** 365-372.

Gonzalez, R. C., Woods, R. E. & Eddins, S. L. (2004) *Digital Image Processing Using MATLAB,* New Jersey, Pearson Education, Inc.

Grimm, M. J. & Williams, J. L. (1997) Measurements of Permeability in Human Calcaneal Trabecular Bone. *Journal of Biomechanics,* 30**,** 743-745.

Guerin, H. A. L. & Elliot, D. M. (Eds.) (2006) *Structure and Properties of Soft Tissues in the Spine*, Elsevier Academic Press.

Gurwitz, G. S., Dawson, J. M., Mcnamara, M. J., Federspiel, C. F. & Spengler, D. M. (1993) Biomechanical Analysis of Three Surgical approaches for Lumbar Burst Fractures Using Short-Segment Instrumentation. *Spine,* 18**,** 977-982.

Hagg, O. & Wallner, A. (1990) Facet Joint Asymmetry and Protrusion of the Intervertebral Disc. *Spine,* 15**,** 356-359.

Hakim, N. S. & King, A. I. (1979) A Three Dimensional Finite Element Dynamic Response Analysis of a Vertebra with Experimental Verification. *Journal of Biomechanics,* 12**,** 277-292.

Harris, M. L., Morberg, P., Bruce, W. J. M. & Walsh, W. R. (1999) An Improved Method for Measuring Tibiofemoral Contact Areas in Total Knee

Arthroplasty: A Comparison of K-scan Sensor and Fuji Film. *Journal of Biomechanics,* 32**,** 951-958.

Hart, L. G., Deyo, R. A. & Cherkin, D. C. (1995) Physician Office Visits for Low Back Pain: Frequency, Clinical Evaluation and Treatment Patterns from a U.S. National Survey. *Spine,* 20**,** 11-19.

Hayes, W. C. & Bodine, A. J. (1978) Flow-Depandant Viscoelastic Properties of Articular Cartilage Matrix. *Journal of Biomechanics,* 11**,** 407-419.

Hayes, W. C. & Mockros, L. F. (1971) Viscoelastic Properties of Human Articular Cartilage. *Journal of Applied Physiology,* 31**,** 562-568.

Hedman, T. P. (1992) A New Transducer for Facet Force Measurement in the Lumbar Spine: Benchmark and In Vitro Test Results. *Journal of Biomechanics,* 25**,** 69-80.

Helbig, T. & Lee, C. K. (1988) The Lumbar Facet Syndrome. *Spine,* 13**,** 61-64.

Holmes, M. H. (1985) A Theoretical Analysis for Determining the Nonlinear Hydraulic Permeability of a Soft Tissue from a Permeation Experiment. *Bulletin of Mathematical Biology,* 47**,** 669-683.

Holmes, M. H. (1986) Finite Deformation of Soft Tissue Analysis of a Mixture Model in Uniaxial Compression. *Journal of Biomechanical Engineering,* 108**,** 372-381.

Holmes, M. H., Lai, W. M. & Mow, V. C. (1985) Singular Perturbation Analysis of the Nonlinear, Flow-Dependent Compressive Stress Relaxation Behavior of Articular Cartilage. *Journal of Biomechanical Engineering,* 107**,** 206-218.

Holmes, M. H. & Mow, V. C. (1990) The Nonlinear Characteristics of Soft Gels and Hydrated Connective Tissues in Ultrafiltration. *Journal of Biomechanics,* 23**,** 1145-1156.

Holzapfel, G. A. & Stadler, M. (2006) Role of Facet Curvature for Accurate Vertebral Facet Load Analysis. *European Spine Journal,* 15**,** 849-856.

Hori, R. & Mockros, L. F. (1976) Indentation Tests of Human Articular Cartilage. *Journal of Biomechanics,* 9**,** 259-268.

Hu, J. C. Y. & Athanasiou, K. A. (Eds.) (2003) *Handbook of Histology Methods for Bone and Cartilage,* Totowa, New Jersey, Humana Press Inc.

Huberti, H. H. & Hayes, W. C. (1988) Contact Pressures in Chondromalacia Patellae and the Effects of Capsular Reconstructive Procedures. *Journal of Orthopaedic Research,* 6**,** 499-508.

Isaksson, H., Van Donkelaar, C. C. & Ito, K. (2009) Sensitivity of Tissue Differentiation and Bone Healing Predictions to Tissue Properties. *Journal of Biomechanics,* 42**,** 555-564.

Jin, H. & Lewis, J. L. (2004) Determination of Poisson's Ratio of Articular Cartilage by Indentation using Different-Sized Indenters. *Journal f Biomechanical Engineering,* 126**,** 138-145.

Jin, Z. M., Pickard, J. E., Forster, H., Ingham, E. & Fisher, J. (2000) Frictional Behaviour of Bovine Articular Cartilage. *Biorheology,* 37**,** 57-63.

Jones, A. C. & Wilcox, R. K. (2008) Finite Element Analysis of the Spine: Towards a Framework of Verification, Validation and Sensitivity Analysis. *Medical Engineering and Physics,* 30**,** 1287-1304.

Kahmann, R. D., Buttermann, G. R., Lewis, J. L. & Bradford, D. S. (1990) Facet Loads in the Canine Lumbar Spine Before and After Disc Alteration. *Spine,* 15**,** 971-978.

Kalichman, L. & Hunter, D. J. (2007) Lumbar Facet Joint Osteoarthritis: A Review. *Seminars in Arthritis and Rheumatism,* 37**,** 69-80.

Kalichman, L., Suri, P., Guermazi, A., Li, L. & Hunter, D. J. (2009) Facet Orientation and Tropism: Associations with Facet Joint Osteoarthritis and Degeneratives. *Spine,* 34**,** E579-E585.

Katta, J. (2007) Self-Assembling Peptide Networks for Treatment of Cartilage Degenerative Diseases. *School of Mechanical Engineering.* Leeds, U.K., University of Leeds.

Katz, J. N. (2006) Lumbar Disc Disorders and Low-Back Pain: Socioeconomic Factors and Consequences. *Journal of Bone and Joint Surgery- American Volume,* 88**,** 21-24.

Kempson, G. E. (1991) Age-Related Changes in the Tensile Properties of Human Articular Cartilage - A Comparative-Study between the Femoral Head of the Hip Joint and the Talus of the Ankle Joint. *Biochimica Et Biophysica Acta,* 1075**,** 223-230.

Kempson, G. E., Freeman, M. A. & Swanson, S. A. (1968) Tensile Properties of Articular Cartilage. *Nature (London),* 220**,** 1127-1128.

Kempson, G. E., Freeman, M. A. & Swanson, S. A. (1971) The Determination of a Creep Modulus for Articular Cartilage from Indentation Tests on the Human Femoral Head. *Jornal of Biomechanics,* 4**,** 239-250.

Kempson, G. E., Muir, H., Pollard, C. & Tuke, M. (1973) The Tensile Properties of the Cartilage of Human Femoral Condyles Related to the Content of Collagen and Glycosaminoglycans. *Biochimica et Biophysica Acta (BBA) - General Subjects,* 297**,** 456-472.

Knecht, S., Vanwanseele, B. & Stussi, E. (2006) A Review on the Mechanical Quality of Articular Cartilage – Implications for the Diagnosis of Osteoarthritis. *Clinical Biomechanics,* 21**,** 999-1012.

Korhonen, R. K., Laasanen, M. S., Toyras, J., Reippo, J., Hirvonen, J., Helminen, H. J. & Jurvelin, J. S. (2002) Comparison of the Equilibrium Response of Articular Cartilage in Unconfined Compression, Confined Compression and Indentation. *Journal of Biomechanics,* 35**,** 903-909.

Kumaresan, S., Yoganandan, N. & Pintar, F. A. (1998) Finite Element Modeling Approaches of Human Cervical Spine Facet Joint Capsule. *Journal of Biomechanics,* 31**,** 371-376.

Kurtz, S. M. & Edidin, A. A. (Eds.) (2006) *Spine Technology Handbook*, Elsevier Academic Press.

Kwan, M. K., Hacker, S. A., Woo, S. L. Y. & Wayne, J. S. (1992) The Effect of Storage on the Biomechanical Behavior of Articular Cartilage: A Large Strain Study. *Journal of Biomechanical Engineering,* 114**,** 149-153.

Kwan, M. K., Lai, W. M. & Mow, V. C. (1984) Fundamentals of Fluid Transport Through Cartilage in Compression. *Annals of Biomedical Engineering,* 1984**,** 6.

Kwan, M. K., Lai, W. M. & Mow, V. C. (1990) A Finite Deformation Theory for Cartilage and Other Soft Hydrated Connective Tissues: Equilibrium Results. *Journal of Biomechanics,* 23**,** 145-155.

Ladd, A. J. C., Kinney, J. H., Haupt, D. L. & Goldstein, S. A. (1998) Finite Element Modeling of Trabecular Bone: Comparison with Mechanical Testing and Determination of Tissue Modulus. *Journal of Orthopaedic Research,* 16**,** 622-628.

Lai, W. M., Hou, J. S. & Mow, V. C. (1991) A Triphasic Theory for the Swelling and Deformation Behaviors of Articular Cartilage. *Journal of Biomechanical Engineering,* 113**,** 245-258.

Lai, W. M. & Mow, V. C. (1980) Drag-Induced Compression of Articular Cartilage During a Permeation Experiment. *Biorheology,* 17**,** 111-123.

Lai, W. M., Mow, V. C. & Roth, V. (1981) Effects of Non-Linear strain-Dependent Permeability and Rate of Compression on the Stress Behaviior of Articular Cartilage. *Journal Biomechanical Engineering,* 103**,** 61-66.

Lane, L. B. & Bullough, P. G. (1980) Age-Related Changes in the Thickness of the Calcified Zone and the Number of Tidemarks in Adult Human Articular Cartilage. *Journal of Bone and Joint Surgery-British Volume,* 62**,** 372-375.

Lanyon, L. E. (1972) In Vivo Bone Strain Recorded from Thoracic Vertebrae of Sheep. *Journal of Biomechanics,* 5**,** 277-281.

Laslett, M., Mcdonald, B., Aprill, C. N., Tropp, H. & Oberg, B. (2006) Clinical Predictors of Screening Lumbar Zygapophyseal Joint Blocks: Development of Clinical Prediction Rules. *The Spine Journal,* 6**,** 370-379.

Leclaire, R., Fortin, L., Lambert, R., Bergeron, Y. M. & Rossignol, M. (2001) Radiofrequency Facet Joint Denervation in the Treatment of Low Back Pain: A Placebo-Controlled Clinical Trial to Assess Efficacy. *Spine,* 26**,** 1411-1417.

Lee, M., Kelly, D. W. & Steven, G. P. (1995) A Model of Spine, Ribcage and Pelvic Responses to a Specific Lumbar Manipulative Force in Relaxed Subjects. *Journal of Biomechanics,* 28**,** 1403-1408.

Lei, F. & Szeri, A. Z. (2007) Inverse Analysis of Constitutive Models: Biological Soft Tissues. *Journal of Biomechanics,* 40**,** 936-940.

Lewinnek, G. E. & Warfield, C. A. (1986) Facet Joint Degeneration as a Cause of Low Back Pain. *Clinical Orthopaedics,* 213**,** 216-222.

Li, X., An, Y. H., Wu, Y. D., Song, Y. C., Chao, Y. J. & Chien, C. H. (2007) Microindentation Test for Assessing the Mechanical Properties of Cartilaginous Tissues. *Journal of Biomedical Material Research Part B: Applied Biomaterials,* 80B**,** 25-31.

Lilius, G., Laasonen, E. M., Myllynen, P., Harilainen, A. & Gronlund, G. (1989) Lumbar Facet Joint Syndrome: A Randomised Clinical Trial. *Journal of Bone and Joint Surgery- British Volume,* 71**,** 681-684.

Lin, H. S., Liu, Y. K. & Adam, K. H. (1978) Mechanical Response of the Lumbar Intervertebral Joint Under Physiological (Complex) Loading. *Journal of Bone and Joint Surgery- American Volume,* 60**,** 41-55.

Linton, S. J., Hellsing, A. L. & Hallden, K. (1998) A Population-Based Study of Spinal Pain Among 35-45 Year-Old Individuals: Prevalence, Sick Leave, and Health Care Use. *Spine,* 23**,** 1457-1463.

Lorenz, M., Patwardhan, A. & Vanderby Jr., R. (1983) Load-Bearing Characteristics of Lumbar Facets in Normal and Surgically Altered Spinal Segments. *Spine,* 8**,** 122-130.

Luo, Z. P., Buttermann, G. R. & Lewis, J. L. (1996) Determination of Spinal Facet Joint Loads from Extra-Articular Strains: A Theoretical Validation. *Jornal of Biomechanics,* 29**,** 785-790.

Lusse, S., Claassen, H., Gehrke, T., Hassenpflug, J., Schunke, M., Heller, M. & Gluer, C. C. (2000) Evaluation of Water Content by Spatially Resolved Transverse Relaxation Times of Human Articular Cartilage. *Magnetic Resonance Imaging,* 18**,** 423-430.

Lyyra, T., Jurvelin, J., Pitkänen, P., Väätäinen, U. & Kiviranta, I. (1995) Indentation Instrument for the Measurement of Cartilage Stiffness Under Arthroscopic Control *Medical Engineering & Physics,* 17**,** 395-399.

Maas, S. A., Ellis, B. J., Rawlins, D. S. & Weiss, J. A. (2009) A Comparison of FEBio, ABAQUS, and NIKE3D: Results for a Suite of Verification Problems. Salt Lake City, UT, USA, The University of Utah.

Mak, A. F., Lai, W. M. & Mow, V. C. (1987) Biphasic Indentation of Articular Cartilage-i Theoretical Analysis. *Journal of Biomechanics,* 20**,** 703-714.

Manchikanti, L., Boswell, M. V., Singh, V., Pampati, V., Damron, K. S. & Beyer, C. D. (2004) Prevalence of Facet Joint Pain in Chronic Spinal Pain of Cervical, Thoracic and Lumbar Regions. *BMC Musculoskeletal Disorders,* 5.

Manchikanti, L. & Pampati, V. (2002) Research Designs in Interventional Pain Management: Is Randomization Superior, Desirable or Essential? *Pain Physician,* 5**,** 275-284.

Manchikanti, L., Pampati, V., Fellows, B. & Bakhit, C. E. (1999) Prevalence of Lumbar Facet Joint Pain in Chronic Low Back Pain. *Pain Physician,* 2**,** 59-64.

Marchand, F. & Ahmed, A. M. (1990) Investigation of the Laminate Structure of Lumbar Disc Anulus Fibrosus. *Spine,* 15**,** 402-410.

Marechal, L. (2009) Advances in Octree-Based All-Hexahedral Mesh Generation: Handling Sharp Features. *18th International Meshing Roundtable.* Salt Lake City, UT, USA.

Marks, R. C., Houston, T. & Thulbourne, T. (1992) Facet Joint Injection and Facet Nerve Block: A Randomised Comparison in 86 Patients with Chronic Low Back Pain. *Pain,* 49**,** 325-328.

Masharawi, Y., Rothschild, B., Dar, G., Peleg, S., Robinson, D., Been, E. & Hershkovitz, I. (2004) Facet Orientation in the Thoracolumbar Spine: Three-dimensional Anatomic and Biomechanical Analysis. *Spine,* 29**,** 1755-1763.

Masharawi, Y., Rothschild, B., Salame, K., Dar, G., Peleg, S. & Hershkovitz, I. (2005) Facet Tropism and Interfacet Shape in the Thoracolumbar Vertebrae. *Spine,* 30**,** 281-292.

Maul, I., Laubli, T., Oliveri, M. & Krueger, H. (2005) Long-term Effects of Supervised Physical Training in Secondary Prevention of Low Back Pain. *European Spine Journal,* 14**,** 599-611.

Maurel, N., Lavaste, F. & Skalli, W. (1997) A Three-Dimensional Parameterized Finite Element Model of the Lower Cervical Spine: Study of the Influence of the Posterior Articular Facets. *Journal of Biomechanics,* 30**,** 921-931.

Mccutchen, C. W. (1962) The Frictional Properties of Animal Joints. *Wear,* 5**,** 1-17.

Mclain, R. F., Yerby, S. A. & Moseley, T. A. (2002) Comparative Morphometry of L4 Vertebrae: Comparison of Large Animal Models for the Human Lumbar Spine. *Spine,* 27**,** E200-E206.

Mens, J. M. A. (2005) The Use of Medication in Low Back Pain. *Best Practice & Research Clinical Rheumatology,* 19**,** 609-621.

Mente, P. L. & Lewis, J. L. (1994) Elastic Modulus of Calcified Cartilage is an Order of Magnitude Less that of Subchondral Bone. *Journal of Orthopaedic Research,* 12**,** 637-647.

Mesfar, W. & Shirazi-Adl, A. (2005) Biomechanics of the Knee Joint in Flexion Under Various Quadriceps Forces. *The Knee,* 12**,** 424-434.

Miller, J. A., Schultz, A. B., Warwick, D. N. & Spencer, D. L. (1986) Mechanical Properties of Lumbar Spine Motion Segments Under Large Loads. *Journal of Biomechanics,* 19**,** 79-84.

Millington, S. A., Li, B., Tang, J. S., Trattnig, S., Crandall, J. R., Hurwitz, S. R. & Acton, S. T. (2007) Quantitative and Topographical Evaluation of Ankle Articular Cartilage Using High Resolution MRI. *Journal of Orthopaedic Research,* 25**,** 143-151.

Mimura, M. (1990) Rotational Instability of the Lumbar Spine: A Three-Dimensional Motion Study Using Bi-plane X-ray Analysis System. *Journal of the Japanese Orthopaedic Association,* 64**,** 546-559.

Mitton, D., Rumelhart, C., Hans, D. & Meunier, P. J. (1997) The Effects of Density and Test Conditions on Measured Compression and Shear Strength of

Cancellous Bone from te Lumbar Vertebrae of Ewes. *Medical Engineering and Physics,* 19**,** 464-474.

Miyazaki, M., Morishita, Y., Takita, C., Yoshiiwa, T., Wang, J. C. & Tsumura, H. (2010) Analysis of the Relationship Between Facet Joint Angle Orientation and Lumbar Spine Canal Diameter with Respect to the Kinematics of the Lumbar Spinal Unit. *Journal of Spinal Disorders & Techniques,* 23**,** 242-248.

Modest, V. E., Murphy, M. C. & Mann, R. W. (1989) Optical Verification of a Technique for In Situ Ultrasonic Measurement of Articular Cartilage Thickness. *Jornal of Biomechanics,* 22**,** 171-176.

Mooney, R. J. & Robertson, J. (1976) The Facet Syndrome. *Clinical Orthopaedics and Related Research,* 115**,** 149-157.

Moore, R. J. (2006) The Vertebral Endplate: Disc Degeneration, Disc Regeneration. *European Spine Journal,* 15**,** S333-S337.

Mosekilde, L. (1993) Vertebral Structure and Strength In Vivo and In Vitro. *Calcified Tissue International,* 53**,** S121-S126.

Mow, V. C., A, R. & Poole, A. R. (1992) Cartilage and Diarthrodial Joints as Paradigms for Hierarchical Materials and Structures. *Biomaterials,* 13**,** 67-97.

Mow, V. C., Gibbs, M. C., Lai, W. M. & Athanasiou, K. A. (1989) Biphasic Indentation of Articular Cartilage-ii. A Numerical Algorithm and an Experimental Study. *Journal of Biomechanics,* 22**,** 853-861.

Mow, V. C., Good, P. M. & Gardner, T. R. (2000) A New Method to Determine the Tensile Properties of Articular Cartilage Using the Indentation Test. *46th Annual Meeting, Orthopaedic Research Society.* Orlando, Florida.

Mow, V. C., Holmes, M. H. & Lai, W. M. (1984) Fluid Transport and Mechanical Properties of Articular Cartilage: A Review. *Journal of Biomechanics,* 17**,** 377-394.

Mow, V. C. & Huiskes, R. (2005) *Basic Orthopaedic Biomechanics and Mechano-Biology*, Lippincott Williams & Wilkins: Philadelphia.

Mow, V. C., Kuei, S. C., Lai, W. M. & Armstrong, C. G. (1980) Biphasic Creep and Stress Relaxation of Articular Cartilage in Compression: Theory and Experiments. *Journal of Biomechanical Engineering,* 102**,** 73-83.

Natarajan, R. N., Chen, B. H., An, H. S. & Andersson, G. B. J. (2000) Anterior Cervical Fusion: A Finite Element model Study on Motion Segment Stability Including the Effect of Osteoporosis. *Spine,* 25**,** 955-961.

Nauman, E. A., Fong, K. E. & Keaveny, T. M. (1999) Dependence of Intertrabecular Permeability on Flow Direction and Anatomic Site. *Annals of Biomedical Engineering,* 27**,** 517-524.

Netter, F. H. (2006) *Atlas of Human Anatomy,* Philadelphia, Pennsylvania., Saunders Elsevier.

Oxland, T. R., Grant, J. P., Dvorak, M. F. & Fisher, C. G. (2003) Effects of Endplate Removal on the Structural Properties of the Lower Lumbar Vertebral Bodies. *Spine,* 28**,** 771-777.

Panjabi, M. M., Oxland, T., Takata, K., Goel, V., Duranceau, J. & Krag, M. (1993) Articular Facets of the Human Spine: Quantitative Three-Dimensional Anatomy. *Spine,* 18**,** 1298-1310.

Panjabi, M. M., Oxland, T., Yamamoto, I. & Crisco, J. J. (1994) Mechanical Behavior of the Human Lumbar and Lumbosacral Spine as Shown by Three-Dimensional Load-Displacement Curves. *Journal of Bone and Joint Surgery-American Volume,* 76**,** 413-424.

Park, S., Krishnan, R., Nicoll, S. B. & Ateshian, G. A. (2003) Cartilage Interstitial Fluid Load Support in Unconfined Compression. *Journal of Biomechanics,* 36**,** 1785-1796.

Parsons, J. R. & Black, J. (1977) The Viscoelastic Shear Behavior of Normal Rabbit Articular Cartilage. *Journal of Biomechanics,* 10**,** 21-29.

Paulsen, F. & Tillmann, B. (1999) Composition of the Extracellular Matrix in Human Cricoarytenoid Joint Articular Cartilage. *Archives Histology and Cytology,* 62**,** 149-163.

Pawaskar, S. S. (2006) Contact Mechanics Modelling of Articular Cartilage and Applications. *School of Mechanical Engineering.* Leeds, U.K., University of Leeds.

Pawaskar, S. S. (2010) Joint Contact Modelling of Articular Cartilage in Synovial Joints. *School of Mechanical Engineering.* Leeds, U.K., University of Leeds.

Pawaskar, S. S., Fisher, J. & Jin, Z. M. (2010) Robust and General Method for Determining Surface Fluid Flow Boundary Contidions in Articular Cartilage Contact Mechanics Modeling. *Journal of Biomechanical Engineering,* 132.

Pawaskar, S. S., Ingham, E., Fisher, J. & Jin, Z. (2011) Fluid Load Support and Contact Mechanics of Hemiarthroplasty in the Natural Hip Joint. *Medical Engineering & Physics,* 33**,** 96-105.

Pearcy, M. J. & Tibrewal, S. B. (1984) Axial Rotation and Lateral Bending in the Normal Lumbar Spine Measured by Three-Dimensional Radiography. *Spine,* 9**,** 582-587.

Pickard, J., Ingham, E., Egan, J. & Fisher, J. (1998) Investigation into the Effect of Proteoglycan molecules on the Tribological Properties of Cartilage Joint Tissues. *Proceedings Inst Mech Eng [H]: Journal of Engineering in Medicine,* 212**,** 177-182.

Pintar, F. A., Yoganandan, N., Myers, T., Elhagediab, A. & Sances Jr, A. (1992) Biomechanical Properties of Human Lumbar Spine Ligaments. *Journal of Biomechanics,* 25**,** 1351-1356.

Plamondon, A., Gagnon, M. & Maurais, G. (1988) Application of a Stareo-Radiographic Method for the Study of Intervertebral Motion. *Spine,* 13**,** 1027-1032.

Ramruttun, A. K., Wong, H. K., Goh, J. C. H. & Ruiz, J. N. (2008) An Improved Methodology for Measuring Facet Contact Forces in the Lumbar Spine. *13th International Conference on Biomedical Engineering.* Singapore, Springer.

Regan, J. J., Hartjen, C. A., Dryer, R. F. & Dirisio, D. J. (2009) ACADIA Facet Arthroplasty US IDE Pilot Study: Twelve Month Follow-Up Results for 20 Patients at Four Centers. *Spine Arthroplasty Society.* London, England.

Reinwald, S. & Burr, D. (2008) Review of Nonprimate, Large Anima Models for Osteoporosis Research. *Journal of Bone and Mineral Research,* 23**,** 1353-1368.

Roemhildt, M. L., Coughlin, K. M., Peura, G. D., Fleming, B. C. & Beynnon, B. D. (2006) Material Properties of Articular Cartilage in the Rabbit Tibial Plateau. *Journal of Biomechanics,* 39**,** 2331-2337.

Rohlmann, A., Zander, T., Schmidt, H., Wilke, H. J. & Bergmann, G. (2006) Analysis of the Influence of Disc Degeneration on the Mechanical Behaviour of a Lumbar Motion Segment using the Finite Element Method. *Journal of Biomechanics,* 39**,** 2484-2490.

Rosen, M. (1994) Report of a Clinical Standards Advisory Group Committee on Back Pain. London: HMSO.

Rushfeldt, P. D., Mann, R. W. & Harris, W. H. (1981) Improved Techniques for Measuring In Vitro the Geometry and Pressure Distribution in the Human

Acetabulum- Ultrasonic Measurement of Acetabular Surfaces, Sphericity and Cartilage Thickness. *Journal of Biomechanics,* 14**,** 253-260.

Sarzi-Puttini, P., Atzeni, F., Fumagalli, M., Capsoni, F. & Carrabba, M. (2004) Osteoarthritis of the Spine. *Seminars in Arthritis and Rheumatism,* 34**,** 38-43.

Schenck, R. C., Athanasiou, K. A., Constantinides, G. & Gomez, E. (1994) A Biomechanical Analysis of Articular-Cartilage of the Human Elbow and a Potential Relationship to Osteochondritis-Dissecans. *Clinical Orthopaedics and Related Research,* 299**,** 305-312.

Schendel, M. J., Wood, K. B., Buttermann, G. R., Lewis, J. L. & Ogilvie, J. W. (1993) Experimental Measurement of Ligament Force, Facet Force and Segment Motion in the Human Lumbar Spine. *Journal of Biomechanics,* 26**,** 427-438.

Schmidt, C. O., Raspe, H., Pfingsten, M., Hasenbring, M., Basler, H. D., Eich, W. & Kohlmann, T. (2007a) Back Pain in the German Adult Population: Prevalence, Severity, and Sociodemographic Correlates in a Multiregional Survey. *Spine,* 32**,** 2005-2011.

Schmidt, H., Heuer, F., Claes, L. & Wilke, H. J. (2008) The Relation Between the Instantaneous Center of Rotation and Facet Joint Forces- A Finite Element Analysis. *Clinical Biomechanics,* 23**,** 270-278.

Schmidt, H., Heuer, F., Drumm, J., Klezl, Z., Claes, L. & Wilke, H. J. (2007b) Application of a Calibration Method Provides More Realistic Results for a Finite Element Model of a Lumbar Spinal Segment. *Clinical Biomechanics,* 22**,** 377-384.

Schultz, A. B., Warwick, D. N., Berkson, M. H. & Nachemson, A. L. (1979) Mechanical Properties of Human Lumbar Spine Motion Sgments. Part 1: Responses in Flexion, Extension, Lateral Bending and Torsion. *Journal Biomechanical Engineering,* 101**,** 46-52.

Schwartz, D. E., Choi, Y., Sandell, L. J. & Hanson, W. R. (1985) Quantitative Analysis of Collagen, Protein and DNA in Fixed, Paraffin-Embedded and Sectioned Tissue. *Histochemical Journal,* 17**,** 655-663.

Schwarzer, A. C., Wang, S. C., O'driscoll, D., Harrington, T., Bogduk, N. & Laurent, R. (1995) The Ability of Computed Tomography to Identify a Painful Zygapophysial Joint in Patients with Chronic Low Back Pain. *Spine,* 20**,** 907-912.

Sharma, M., Langrana, N. A. & Rodriguez, J. (1995) Role of Ligaments and Facets in Lumbar Spinal Stability. *Spine,* 20**,** 887-900.

Sharma, M., Langrana, N. A. & Rodriguez, J. (1998) Modeling of Facet Articulation as a Nonlinear Moving Contact Problem: Sensitivity Study on Lumbar Facet Response. *Journal of Biomechanical Engineering,* 120**,** 118-125.

Sheng, S. R., Wang, X. Y., Xu, H. Z., Zhu, G. Q. & Zhou, Y. F. (2010) Anatomy of Large Animal Spines and Its Comparison to the Human Spine: A Systematic Review. *European Spine Journal,* 19**,** 46-56.

Shepherd, J. F. & Johnson, C. R. (2009) Hexahedral Mesh Generation for Biomedical Models in SCIRun. *Engineering with Computers,* 25**,** 97-114.

Shirazi-Adl, A. (1994) Nonlinear Stress Analysis of the Whole Lumbar Spine in Torsion-Mechanics of Facet Articulation. *Journal of Biomechanics,* 27**,** 289-299.

Shirazi-Adl, A., Ahmed, A. M. & Shrivastava, S. C. (1986a) A Finite Element Study of a Lumbar Motion Segment Subjected to Pure Sagittal Plane Moments. *Journal of Biomechanics,* 19**,** 331-350.

Shirazi, R. & Shirazi-Adl, A. (2009) Computational Biomechanics of Articular Cartilage of Human Knee Joint: Effect of Osteochondral Defects. *Journal of Biomechanics,* 42**,** 2458-2465.

Silva, M. J., Wang, C., Keaveny, T. M. & Hayes, W. C. (1994) Direct and Computed Tomography Thickness Measurements of the Human, Lumbar Vertebral Shell and Endplate. *Bone,* 15**,** 409-414.

Slotz, M. A. & Ateshian, G. A. (1998) Experimental Verification and Theoretical Prediction of Cartilage Interstitial Fluid Pressurezation at an Impermeable Contact Interface in Confined Compression. *Journal of Biomechanics,* 31**,** 927-934.

Smit, T. H. (2002) The Use of a Quadruped as an In Vivo Model for the Study of the Spine- Biomechanical Considerations. *European Spine Journal,* 11**,** 137-144.

Stokes, I. A. F. (1988) Mechanical Function of Facet Joints in the Lumbar Spine. *Clinical Biomechanics,* 3**,** 101-105.

Strine, T. W. & Hootman, J. M. (2007) US National Prevalence and Correlates of Low Back and Neck Pain Among Adults. *Arthritis & Rheumatism (Arthritis Care & Research),* 57**,** 656-665.

Swann, A. C. & Seedhom, B. B. (1989) Improved Techniques for Measuring the Indentation and Thickness of Articular Cartilage. *Proceedings Inst Mech Eng [H]: Journal of Engineering in Medicine,* 203**,** 143-150.

Tabacu, S., Hadar, A., Stanescu, N. D., Ilie, S. & Tudor, D. I. (2010) Hexahedral Finite Elements Mesh Generation Method with Applications to Plastics Parts. *Materiale Plastice, 47,* 94-102.

Tencer, A. F., Ahmed, A. M. & Burke, D. L. (1982) Some Static Mechanical Properties of the Lumbar Interbvertebral Joint, Intact and Injured. *Journal Biomechanical Engineering, 104,* 193-201.

Teo, E. C., Lee, K. K., Qiu, T. X., Ng, H. W. & Yang, K. (2004) The Biomechanics of Lumbar Graded Facetectomy Under Anterior-Shear Load. *IEEE Transactions on Biomedical Engineering, 51,* 443-449.

Teo, E. C. & Ng, H. W. (2001a) First Cervical Vertebra (Atlas) Fracture Mechanism Studies Using Finite Element Method. *Journal of Biomechanics, 34,* 13-21.

Teo, E. C. & Ng, H. W. (2001b) Evaluation of the Role of Ligaments, Facets and Disc Nucleus in Lower Cervical Spine Under Compression and Sagittal Moments Using Finite Element Method. *Medical Engineering and Physics, 23,* 155-164.

Tobias, D., Ziv, I. & Maroudas, A. (1992) Human Facet Cartilage: Swelling and Some Physicochemical Characteristics as a Function of Age - Swelling of Human Facet Joint Cartilage. *Spine, 17,* 694-700.

Treppo, S., Koepp, H., Quan, E. C., Cole, A. A., Kuettner, K. E. & Grodzinsky, A. J. (2000) Comparison of Biomechanical and Biochemical Properties of Cartilage from Human Knee and Ankle Pairs. *Journal of Orthopaedic Research, 18,* 739-748.

Tulsi, R. S. & Hermanis, G. M. (1993) A Study of the Angle of Inclination and Facet Curvature of Superior Lumbar Zygapophyseal Facets. *Spine, 18,* 1311-1317.

Ueno, K. & Liu, Y. K. (1987) A Three-Dimensional Nonlinear Finite Element Model of Lumbar Intervertebral Joint in Torision. *Journal of Biomechanical Engineering, 109,* 200-209.

Van Der Rest, M. & Mayne, R. (1988) Type IX Collagen Proteoglycan from Cartilage is Covalently Cross-linked to Type II Collagen. *The Journal Biological Chemistry, 263,* 1615-1618.

Van Kleef, M., Barendse, G. A. M., Kessels, A., Voets, H. M., Weber, W. E. J. & De Lange, S. (1999) Randomized Trial of Radiofrequency Lumbar Facet Denervation fro Chronic Low Back Pain. *Spine, 24,* 1937-1942.

Van Rietbergen, B., Weinans, H., Huiskes, R. & Odgaard, A. (1995) A New Method to Determine Trabecular Bone Elastic Properties and Loading Using
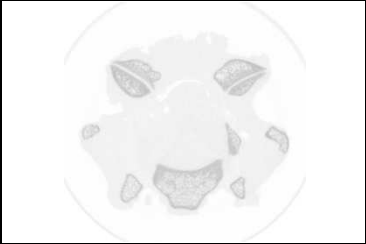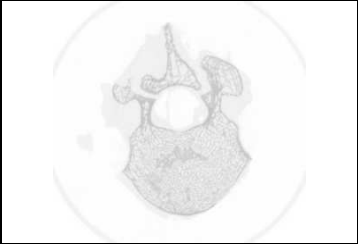
Micromechanical Finite Element Models. *Journal of Biomechanics,* 28**,** 69-81.

Van Schaik, J. P. J. & Van Pinxteren, B. (1999) Curvature of the Lower Lumbar Facet Joints: Variations at Different Levels and Relationship with Orientation. *Journal of Spinal Disorders,* 12**,** 341-347.

Van Schaik, J. P. J., Van Pinxteren, B., Verbiest, H., Crowe, A. & Zuiderveld, K. (1997) The Facet Orientation Circle: A New Parameter for Facet Joint Angulation in the Lower Lumbar Spine. *Spine,* 22**,** 531-536.

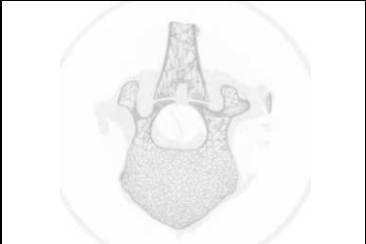Vanharanta, H., Floyd, T., Ohnmeiss, D. D., Hochschuler, S. H. & Guyer, R. D. (1993) The Relationship of Facet Tropism to Degenerative Disc Disease. *Spine,* 18**,** 1000-1005.

Vanwanseele, B., Eckstein, F., Hadwighorst, H., Knecht, H., Spaepen, A. & Stussi, E. (2004) In Vivo Precision of Quantitative Shoulder Cartilage Measurements, and Changes After Spinal Cord Injury. *Magnetic Resonance in Medicine,* 51**,** 1026-1030.

Wagner, U. A., Sangeorzan, B. J., Harrington, R. M. & Tencer, A. F. (1992) Contact Characteristics of the Subtalar Joint: Load Distribution Between the Anterior and Posterior Facets. *Journal of Orthopaedic Research,* 10**,** 535-543.

Warner, J. J. P., Bowen, M. K., Deng, X. H., Hannafin, J. A., Arnoczky, S. P. & Warren, R. F. (1998) Articular Contact Patterns of the Normal Glenohumeral Joint. *Journal of Shoulder and Elbow Surgery,* 7**,** 381-388.

Warner, M. D., Taylor, W. R. & Clift, S. E. (2001) Finite Element Biphasic Indentation of Cartilage: A Comparison of Experimental Indenter and Physiological contact geometries. *Proceedings of the Institution of Mechanical Engineers Part [H]: Journal of Engineering in Medicine,* 215**,** 487-496.

Weightman, B., Chappell, D. J. & Jenkins, E. A. (1978) A Second Study of Tensile Fatigue Properties of Human Articular Cartilage. *Annals of the Rheumatic Diseases,* 37**,** 58-63.

Weishaupt, D., Zanetti, M., Boos, N. & Hodler, J. (1999) MR Imaging and CT in Osteoarthritis of the Lumbar Facet Joints. *Skeletal Radiology,* 28**,** 215-219.

White, A. E. T., Bentley, G., Stephens, M. D., Bader, D. L., Giddins, G. E. B. & Lee, D. A. (1999) The Effects of Storage Temperature on the Composition, Metabolism and Biomechanical Properties of Human Articular Cartilage. *The Knee,* 6**,** 197-205.

Wilcox, R. K. (2006) The Biomechanical Effect of Vertebroplasty on the Adjacent Vertebral Body: A Finite Element Study. *Proceedings of the Institution of Mechanical Engineers Part [H]: Journal of Engineering in Medicine,* 220**,** 565-572.

Wilcox, R. K. (2007) The Influence of Material Property and Morphological Parameters on Specimen-Specific Finite Element Models of Porcine Vertebral Bodies. *Journal of Biomechanics,* 40**,** 669-673.

Wilke, H. J., Kettler, A. & Claes, L. E. (1997a) Are Sheep Spines a Valid Biomechanical Model for Human Spine? *Spine,* 22**,** 2365-2374.

Wilke, H. J., Kettler, A., Wenger, K. H. & Claes, L. E. (1997b) Anatomy of the Sheep Spine and Its Comparison to the Human Spine. *The Anatomical Record,* 247**,** 542-555.

Wilke, H. J., Krischak, S. & Claes, L. (1996) Biomechanical Comparison of Calf and Human Spines. *Journal of Orthopaedic Research,* 14**,** 500-503.

Wilke, H. J., Neef, P., Caimi, M., Hoogland, T. & Claes, L. E. (1999) New In Vivo Measurements of Pressures in the Intervertebral Disc in Daily Life. *Spine,* 24**,** 755-762.

Willet, T. L., Whiteside, R., Wild, P. M., Wyss, U. P. & Anastassiades, T. (2005) Artefacts in the Mechanical Characterization of Procine Articular Cartilage due to Freezing. *Proceedings of the Institution of Mechanical Engineers Part [H]: Journal of Engineering in Medicine,* 219**,** 23-29.

Wilson, D. C., Niosi, C. A., Zhu, Q. A., Oxland, T. R. & Wilson, D. R. (2006) Accuracy and Repeatability of a New Method for Measuring Facet Loads in the Lumbar Spine. *Journal of Biomechanics,* 39**,** 348-353.

Wilson, D. R., Apreleva, M. V., Eichler, M. J. & Harrold, F. R. (2003) Accuracy and Repeatability of a Pressure Measurement System in the Patellofemoral Joint. *Journal of Biomechanics,* 36**,** 1909-1915.

Wiseman, C. M., Lindsey, D. P., Fredrick, A. D. & Yerby, S. A. (2005) The Effect of an Interspinous Process Implant on Facet Loading During Extension. *Spine,* 20**,** 903-907.

Wu, J. Z., Herzog, W. & Epstein, M. (1998) Effects of Inserting a Presensor Film into Articular Joints on the Actual Contact Mechanics. *Journal of Biomechanical Engineering,* 120**,** 655-659.

Yamamoto, I., Panjabi, M. M., Crisco, T. & Oxland, T. (1989) Three Dimensional Movements of the Whole Lumbar Spine and Lumbosacral Joint. *Spine,* 14**,** 1256-1260.

Yang, K. H. & King, A. I. (1984) Mechanism of Facet Load Transmission as a Hypothesis for Low-Back Pain. *Spine,* 9**,** 557-565.

Yoganandan, N., Knowles, S. A., Maiman, D. J. & Pintar, F. A. (2003) Anatomic Study of the Morphology of Human Cervical Facet Joint. *Spine,* 28**,** 2317-2323.

Yoganandan, N., Kumaresan, S. C., Voo, L., Pintar, F. A. & Larson, S. J. (1996) Finite Element Modeling of the C4-C6 Cervical Spine Unit. *Medical Engineering and Physics,* 18**,** 569-574.

Young, S., Aprill, C. & Laslett, M. (2003) Correlation of Clinical Examination Characteristics with Three Sources of Chronic Low Back Pain. *The Spine Journal,* 3**,** 460-465.

Zhu, Q., Larson, C. R., Sjovold, S. G., Rosler, D. M., Keynan, O., Wilson, D. R., Cripton, P. A. & Oxland, T. R. (2007) Biomechanical Evaluation of the Total Facet Arthroplasty System: 3-Dimensional Kinematics. *Spine,* 32**,** 55-62.

Ziv, I., Maroudas, C., Robin, G. & Maroudas, A. (1993) Human Facet Cartilage: Swelling and Some Physicochemical Characteristics as a Function of Age - Age Changes in Some Biophysical Parameters of Human Facet Joint Cartilage. *Spine,* 18**,** 136-146.

Appendix I: µCT Scan Image of Facet Joint for Spine 2

Table A-1. µCT scan images of the ovine facet joint for Spine 2.

Vertebral Segment	µCT Scan Image	Vertebral Segment	µCT Scan Image
C2C3		T8T9	
C4C5		T10T11	
C6C7		T12T13	
T2T3		L1L2	
T4T5		L3L4	
T6T7		L5L6	

Appendix II: Publication and Conference Presentations

Journal Publication to be Submitted

Spine: "Investigation of the sheep spine as a biomechanical model for human spines in facet joint study", Abd Latif, M.J.; Jin, Z.; and Wilcox, R.K. (2011).

Journal of Biomechanics: "Biomechanical characterisation of ovine spinal facet joint cartilage", Abd Latif, M.J.; Jin, Z.; and Wilcox, R.K. (2011).

Conference Oral Presentation

4th International Conference of Computational Bioengineering (2009), Bertinoro, Italy;

17th Congress of the European Society of Biomechanics 2010, Edinburgh, UK;

6th World Congress on Biomechanics 2010, Singapore.

Conference Poster Presentation

British Orthopaedic Research Society (2009), Newcastle, UK.

Appendix III: Abstract for 4th International Conference of Computational Bioengineering (2009).

Morphological Study of Ovine Spinal Facet Joints

Mohd Juzaila Abd Latif, Zhongmin Jin and Ruth K. Wilcox

Introduction

The ovine spine is often used as a model for the human spine, although the anatomical comparisons of the spinal facet joints have yet to be established. The facet joints are important in governing the kinematics of the spine and a recent computational study has shown that the level of curvature of the facet surfaces has a significant effect on the segment load-displacement characteristics and the facet stress distribution (Holzapfel, 2006).

Although studies have been made to characterise the facet curvature (van Schaik, 1999; McLain, 2002), newer imaging methodologies will now allow more accurate characterisation. The purpose of this study was to develop a new method to characterise the facet curvature from micro-computed tomography (μCT) images and investigate the morphology of ovine spinal facet joints.

Methods

Two female Texel ovine spines (age, 4 to 5 years) were dissected into two-vertebra segments and imaged using μCT. The scan plane was parallel to the upper endplate of the segmented vertebra. The facet orientation angles were evaluated using the transverse scan images as shown in Figure 1.
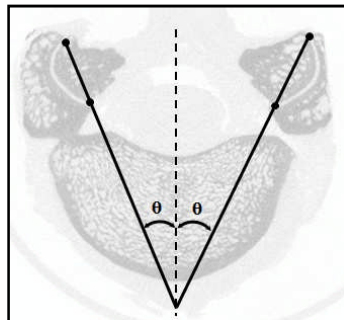

Figure 1: Facet orientation angle measurement.

Based on the active contour segmentation method [Chan, 2001], the facet joint images were segmented and the edge was detected using the Canny method in a MatLab (MathWorks Inc.) program. Boundaries were then created at the superior and inferior curvatures of the facet articular surface and the points along the boundaries were extracted. The points were used to create circles using a least-squares method to determine the superior and inferior facets radii as in Figure 2.
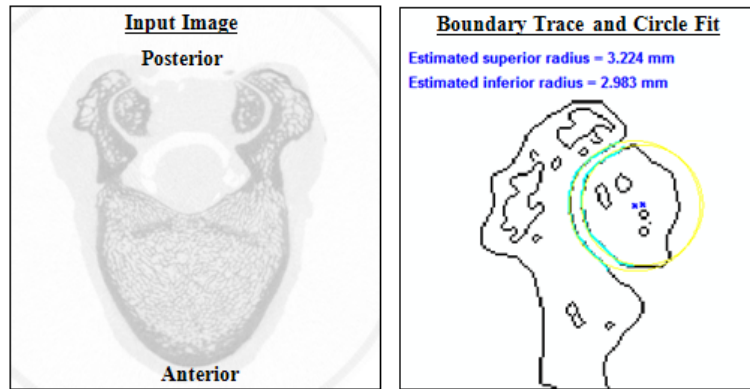
Figure 2: Transverse facet radius measurement.

Results

The measurements of the facet radii and angles from the lumbar region are illustrated in Figure 3. The facet joints of the thoracic vertebral segments from T2 to T11 were found to be virtually flat.
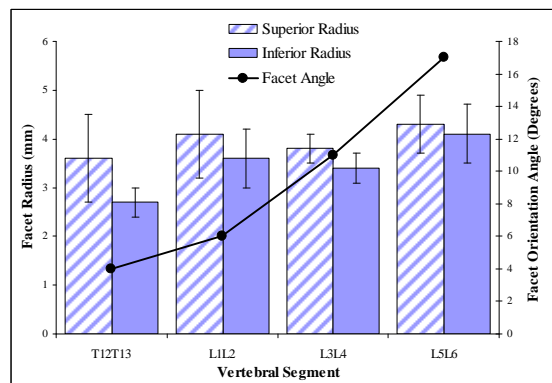

Figure 3: Results of facet radius and angle.

Discussion

This anatomical study described a new method to characterise the facet joint curvature using μCT. The results provide a comprehensive morphologic database of the Texel ovine facet joints curvature. Although there were differences in the facet radius compared with the human, the lumbar region possesses similar curvature and might be used as a model for the human spine.

References

Chan *et al.*, IEEE Trans Image Procss., 10:266-277, 2001.
Holzapfel *et al.*, Eur Spine J, 15:849-856, 2006.
McLain *et al.*, Spine, 27:E200-E206, 2002.
Van Schaik *et al.*, J Spinal Disorders, 12:341-347, 1999.

Appendix IV: Abstract for 6th World Congress on Biomechanics 2010.

Biomechanical Characterisation of Ovine Facet Joint Cartilage

Mohd Juzaila Abd Latif, Zhongmin Jin and Ruth K. Wilcox

Introduction

Articular cartilage has been extensively characterised in previous studies for many synovial joints, however there has been limited investigation of the spinal facet joint. Only recently the facet cartilage biomechanical properties have been characterised for the first time using canine lumbar vertebrae [1]. However in studies of biomechanics, ovine spines are more often used due to the anatomy and range of motion being similar to the human spine[2,3].

This study therefore aimed to characterise the ovine facet joint cartilage to obtain the biphasic properties of elastic modulus and permeability. In addition, a novel specimen-specific model which included the structure of the subchondral bone was developed for further investigation.

Methods

Cylindrical cartilage pins (n=10) were harvested from Texel ovine cervical facet joints (C2-C7) between 4-5 years old. The specimens were kept between 2-5ºC overnight and tested within 24 hours. In order to evaluate the cartilage thickness, the specimens were imaged using micro-computed tomography (μCT). In addition, indentation tests were undertaken using a needle indenter for comparison purposes.

The biphasic experimental data were obtained from creep indentation tests using a 2 mm diameter spherical indenter subjected to 0.24 N load for 30 minutes. Both 2D and 3D specimen-specific poroelastic biphasic finite element models of the specimens were generated. The 2D models assumed axisymmetry whilst the 3D model were based on the μCT scan images following segmentation (ScanIP, Simpleware Ltd., UK). All of the models were solved using Abaqus (Simulia Corp., RI, USA). The elastic modulus and permeability of cartilage were derived by curve-fitting the computational prediction of the displacement from the FE model to the corresponding experiment indentation data[4].

Results

Good agreement was found (2% difference) between the μCT and indentation measurement of the cartilage thickness with the average thickness of 0.52±0.1 mm. However, it was found that an appropriate weight (>4N) must be applied for the indentation test. The properties derived from the FE models were 0.76±0.3 MPa for the biphasic elastic modulus and 1.61±1.1 x 10-15 m4/Ns for the permeability.

Discussion

This study provides the cartilage biphasic properties for the ovine facet joints. The use of the finite element models enabled the cartilage properties to be obtained whilst taking into account the individual specimen geometry. The properties obtained were found to be in a similar range to human cartilage from other synovial

joints. The 3D finite element models will now be used to investigate the effect of subchondral bone stiffness during the cartilage indentation. This analysis could be extended to the osteoarthritis studies as increasing evidence suggests that subchondral bone and cartilage health seem to be closely related in the progression of osteoarthritis[5].

References

[1] Elder B. D. *et al.*, J. Neurosurg.: Spine. 10:623-628, 2009.

[2] Wilke H. J. *et al.*, The Anatomical Record. 247:542-555, 1997.

[3] Wilke H. J. *et al.*, Spine. 22:2365-2374, 1997.

[4] Pawaskar S. S. *et al.*, J. Biomech Eng., 2010.

[5] Karsdal M. A. *et al.*, Osteoarthritis and Cartilage. 16:638-646, 2008.